Robust and Efficient Mathematical Techniques for Modeling and Simulation of Smart Material Systems

Dissertation

Presented in Partial Fulfillment of the Requirements for the Degree
Doctor of Philosophy in the Graduate School of The Ohio State
University

By

Hafez Tari, M.S.

Graduate Program in Mechanical Engineering

The Ohio State University

2014

Dissertation Committee:

Professor Marcelo J. Dapino, Advisor

Professor Gary L. Kinzel

Professor Daniel A. Mendelsohn

Professor Brian Harper

© Copyright by
Hafez Tari
2014

Abstract

This dissertation presents robust and efficient mathematical techniques for modeling and simulation of smart material systems. First, passive materials are discussed which undergo large deformations. Taking the Euler–Bernoulli cantilever beams as an example, parametric large deflection components for the case of a combined tip point loading are developed. Verified by comparison with numerical solutions, the obtained parametric deflection solutions are valid for the entire beam length, and independently and efficiently adaptable for very large loading conditions. To demonstrate the robustness of the solutions, the piecewise parametric solutions are coded as a stand-alone executable, *BeamSol*, which is envisioned to help engineering analyses and syntheses of beam applications. Then, smart materials, in particular, magnetostrictive materials are discussed. A reformulation of the Discrete Energy-Averaged model is given for the calculation of the 3D hysteretic magnetization and magnetostriction of iron-gallium (Galfenol) alloys, and an analytical solution procedure based on eigenvalue decomposition is developed. This procedure avoids the singularities present in the existing approximate solution by offering multiple local minimum energy directions for each easy crystallographic direction. This improved robustness is crucial for use in black-box finite-element codes. Also, analytical simplifications of the 3D model to 2D and 1D applications are presented. To find model parameters, the average of the hysteretic data is utilized. This obviates any need for anhysteretic curves, which would require additional measurements. An efficient optimization routine is developed that retains the dimensionality of the prior art, but improves the accuracy and computational efficiency. Analytical derivations of the Jacobian and Hessian matrices corresponding to this direct model are also presented. Then, a computationally efficient and robust nonlinear modeling framework is presented for fast design and optimization of nonlinear smart materials. The framework consists of a novel 3D inversion scheme for nonlinear modeling of smart material transducers, and a reduced 2D model for smart composite plate structures. Building on the Newton technique, the inversion scheme can be applied to any nonlinear smart material system with a differentiable direct model. The nonlinear 2D magnetostrictive plate model and the 3D inversion scheme are integrated with a finite-element software to analyze an aluminum plate embedded with a Galfenol strip. The resulting nonlinear finite-element framework is utilized to obtain major and minor magnetostriction curves corresponding to the tip of the Galfenol patch exposed to unbiased and biased magnetic fields. A significant advantage in computational time and numerical convergence is demonstrated via comparison with an existing approach for magnetostrictive material modeling. Finally, a globally convergent and fully coupled magnetomechanical model is developed for 3D magnetostrictive systems. The inverse model finds the unknown magnetic field and stress vectors for any specified magnetic flux density and strain vectors. This inversion procedure is iterative, and is proposed for arbitrary magnetostrictive materials. Built on *continuation*, the approach is globally convergent, which makes it ideal for use in finite-element frameworks. Galfenol is chosen as the magnetostrictive material, and the computational efficiency of the proposed approach is shown to compare favorably against existing models.

To my extraordinary parents and grandparents!

Acknowledgments

This dissertation and the work presented would not have been fulfilled without the help and support of many individuals. Foremost, my thank goes to my advisor, Prof. Marcelo J. Dapino, for providing me the opportunity to work on this project. I am grateful for the technical and professional advice given throughout the project. There has never been an occasion, when I've knocked on his office door and he hasn't given me time. I hope to reach an academic position in the very near future that justifies his invaluable support. Prior to joining his lab, I was advised by Prof. Gary L. Kinzel and Prof. Daniel A. Mendelsohn, who have believed in me and encouraged me to be pushed further. They have selflessly supported me, and provided me the opportunity to further branch out in my academic studies at the Ohio State. Prof. Kinzel has given me fatherly advice in both my academic and personal life. I have a greatest respect for this extraordinary person, and I will continue to see him as my mentor. I would also like to thank Prof. Brian Harper for serving on my dissertation committee. It is impossible for me to describe how much admiration and respect I have for all of these extraordinary individuals.

I would like to thank Prof. Ahmet Selamet and Prof. Krishnaswamy Srinivasan, respectively, the current and former chairs of the Department of Mechanical and Aerospace Engineering for their understanding and financial support during my studies at the Ohio State. Also, I would like to thank Ms. Janeen Sands and Mr. Nick Breckenridge of the Graduate Office for their support.

Also, I would like to thank my friends and collaborators at the Smart Materials and Structures Lab. I have had collaborations with Dr. Sushma Santapuri and Mr. Justin Scheidler. I have had enjoyable time discussing and interacting with these people and other great individuals in the lab including Mr. Adam Hehr, Mr. Joshua Pritchard, Dr. John Larson, Mr. Zhangxian Deng, Mr. Sheng Dong, Mr. Mark Riggs, and Mr. Paul Wolcott.

I would like to thank my extraordinary friends, Mr. Bob Lowe and Mr. Mohammad Ali Rezaei (and his family), who have patiently supported me and given me brotherly advice when I have needed. They will remain two best friends of mine for the rest of my life.

I owe my deepest thanks to every member of my family, my father, to whom I owe my life; my Mom, brother, and two sisters, whom I love; my grandparents, uncle, and his family, for whom I have a greatest respect. They have always stood by me even at distance and guided me through my career, and have pulled me through against impossible odds at times. I thank all of them for always believing in me and encouraging me to push myself further. Words are unable to express the gratitude I owe them.

So much thanks to God for surrounding me with all of the aforementioned extraordinary people.

Vita

May, 2011	M.S. Mechanical Engineering, University of Maryland, Baltimore County, Maryland, USA
May, 2008	M.S. Mechanical Engineering, University of Mazandaran, Mazandaran, Iran
May, 2005	B.S. Mechanical Engineering, University of Mazandaran, Mazandaran, Iran

Publications

Hafez Tari, "On the Parametric Large Deflection Study of Euler–Bernoulli Cantilever Beams subjected to Combined Tip Point Loading." *International J. of Non–Linear Mechanics*, 49: 90–99, 2013.

Hafez Tari, H.-J. Su and J.D. Hauenstein, "Classification and Complete Solution of the Kinetostatics of a Compliant Stewart–Gough Platform." *Mechanism and Machine Theory*, 49: 177–186, 2012.

Hafez Tari and H.-J. Su, "A Complex Solution Framework for the Kinetostatic Synthesis of Compliant Four-Bar Mechanisms." *Mechanism and Machine Theory*, 46(8): 1137–1152, 2011.

H.-J. Su and Hafez Tari, "On Line Screw Systems and Their Application to Flexure Synthesis." *ASME, J. of Mechanisms and Robotics*, 3(1): 011009, 2011.

Hafez Tari and H.-J. Su, "Complete Solution to the Eight-Point Path Generation of Slider-Crank Four-Bar Linkages." *ASME, J. of Mechanical Design*, 132(8): 081003, 2010.

Hafez Tari, H.-J. Su and T.Y. Li, "A Constrained Homotopy Technique for excluding unwanted Solutions from Polynomial Equations arising in Kinematics Problems." *Mechanism and Machine Theory*, 45(6): 898–910, 2010.

H.-J. Su and Hafez Tari, "Realizing Orthogonal Motions with Wire Flexures Connected in Parallel." *ASME, J. of Mechanical Design*, 132(12): 121002, 2010.

M.H. Hojjati and Hafez Tari, "On the Solution of Transient Heat Conduction of Multi-Layer Slab and Filtering Temperature Measurements." *Multidiscipline Modeling in Materials and Structures*, 6(1): 166–178, 2010.

M.H. Hojjati and Hafez Tari, "Variational Iteration Solutions for Nonlinear Differential Equations of Different Damping Models in Oscillations and Vibrations." *Far East J. of Dynamical Systems*, 10(1), 131–143, 2008.

D.D. Ganji, A. Sadighi, Hafez Tari, M. Gorji and N. Haghparast, "Large Deflection of a Cantilever Beam under Point Load using the Homotopy Perturbation Method." *Topological Methods in Nonlinear Analysis*, 31(2): 271–277, 2008.

Hafez Tari, "Modified Variational Iteration Method." *Physics Letters A*, 369(4): 290–293, 2007.

Hafez Tari, D.D. Ganji and H. Babazadeh, "The Application of He's Variational Iteration Method to Nonlinear Equations Arising in Heat Transfer." *Physics Letters A*, 363(3): 213–217, 2007.

Hafez Tari and D.D. Ganji, "Approximate Explicit Solutions of Nonlinear BBMB Equations by He's Methods and Comparison with the Exact Solution." *Physics Letters A*, 367(1–2): 95–101, 2007.

Hafez Tari, D.D. Ganji and M. Rostamian, "Approximate Solutions of K(2,2), KdV and Modified KdV Equations by Variational Iteration Method, Homotopy Perturbation Method and Homotopy Analysis Method." *Int. J. of Nonlinear Sciences and Numerical Simulations*, 8(2): 203–210, 2007.

D.D. Ganji, Hafez Tari and M.B. Jooybari, "Variational Iteration Method and Homotopy Perturbation Method for Nonlinear Evolution Equations." *Computers and Mathematics with Applications*, 54(7–8): 1018–1027, 2007.

D.D. Ganji, Hafez Tari, R. Kalantari and M. Shahiri, "Approximate Explicit Solutions of Homotopy Perturbation and Perturbation Methods for Forced Nonlinear

Oscillation of Quasi-Harmonic Systems." *Far East J. of Dynamical Systems*, 9(2): 165–174, 2007.

Fields of Study

Major Field: Mechanical Engineering

Studies in:

- Smart Materials and Structures
- Solid Mechanics
- Compliant Mechanisms
- Numerical Algebraic Geometry
- Applied Mathematics

Table of Contents

Page

Abstract . . . ii
Dedication . . . iv
Acknowledgments . . . v
Vita . . . vii
List of Figures . . . xiii
List of Tables . . . xvii
List of Symbols . . . xviii

Chapters

1 Introduction and Background . . . 1
- 1.1 Passive materials . . . 2
  - 1.1.1 Contributions . . . 4
- 1.2 Smart materials . . . 6
  - 1.2.1 Contributions . . . 8
- 1.3 Organization of the Dissertation . . . 10

2 Effective Start Point for the Automatic Taylor Expansion Technique 12
- 2.1 Introduction . . . 13
- 2.2 Statement of the Problem . . . 15
- 2.3 Basic Concepts of the Automatic Taylor Expansion Technique (ATET) 15
  - 2.3.1 Review of ATET . . . 16
  - 2.3.2 Choice of the Start Point z_0 . . . 17
  - 2.3.3 Choice of the Approximation Order M . . . 19
  - 2.3.4 Example . . . 20
  - 2.3.5 Multiple Solution Branches . . . 22
  - 2.3.6 ATET for a System of Nonlinear ODEs . . . 23
- 2.4 Nonlinear BVPs from Engineering and Science . . . 24
  - 2.4.1 Application 1: Micropolar Fluids . . . 24
  - 2.4.2 Application 2: Heat Transfer . . . 28
  - 2.4.3 Application 3: Theoretical Biology . . . 33

2.5 Summary and Conclusions 35

3 Parametric Large Deflection Solutions for Euler–Bernoulli Cantilever Beams 37
3.1 A Brief Review on Euler–Bernoulli Beams 38
3.2 Parametric Large Deflection Solutions 40
    3.2.1 Choice of the Start Point s_0 42
    3.2.2 Choice of the Approximation Orders $\mathcal{M}_1$-$\mathcal{M}_3$ 44
3.3 Beam's Characteristic Equation 45
    3.3.1 A Circular Deflection 46
3.4 Parametric Study of the Beam's Deflection 48
    3.4.1 Pure End-Force 49
    3.4.2 Dominant End-Moment 54
    3.4.3 Dominant End-Force 55
    3.4.4 Mixed Loading with Inflection Point 57
3.5 Summary and Conclusions 62

4 Cartesian and Piecewise Parametric Large Deflection Solutions . 63
4.1 Cartesian Large Deflection Solutions 64
4.2 Piecewise Parametric Large Deflection Solutions 66
    4.2.1 Choice of the Number of Subdivisions n 70
    4.2.2 Choice of the Segments' Endpoints s_i and s_{i+1} 71
    4.2.3 Choice of the Start Points s_{0i} 71
    4.2.4 Independence of the Approximation Orders 71
    4.2.5 Solution of the Boundary Constraints $\mathcal{B}(\mathcal{C}_{4n})$ 72
4.3 *BeamSol*: A Large Deflection *Beam Sol*ver 72
4.4 Summary and Conclusions 74

5 Calculation of the 3D Hysteretic Magnetization and Magnetostriction of Iron-Gallium Alloys 75
5.1 Review of calculation of the 3D magnetostriction and magnetic flux density for Galfenol 77
    5.1.1 Calculation of $\overset{k}{\mathbf{m}}$ (approximate solution) 79
    5.1.2 Magnetomechanical hysteresis 79
5.2 Reformulation of the DEA Model with Exact Solution Procedure . . 80
    5.2.1 Calculation of $\overset{k}{\mathbf{m}}$ (exact solution) 82
5.3 Simplification of the Model for Lower Dimensional Applications . . . 87
    5.3.1 2D Applications 88
    5.3.2 1D Applications 89
5.4 Parameter Optimization 90
    5.4.1 Extracting the averaged responses from hysteretic measurements 91

5.4.2 Objective Error Function 91
5.4.3 Some Notes on the Optimization 93

5.5 Validation of the Model: Results and Discussion 94
5.5.1 Validation of the Nonhysteretic Model 94
5.5.2 Computational Efficiency 98
5.5.3 Validation of the Hysteretic Model 99

5.6 Summary and Conclusions 102

6 Derivative terms for the direct model for Galfenol 104

6.1 Derivative terms for the direct model, given in Chapter 5 105
6.1.1 Jacobian terms 107
6.1.2 Hessian terms 109

6.2 Summary and Conclusions 113

7 Efficient and Robust Nonlinear Model for Smart Materials with Application to Composite Magnetostrictive Plates 114

7.1 3D System Model for Embedded Smart Composites 116
7.1.1 Inversion Procedure for One-way Coupled Constitutive Model 117

7.2 Reduced 2D System Model for Embedded Smart Composites 119

7.3 Case study: Galfenol-aluminium structure for actuator applications . 122
7.3.1 Solution Methodology 123
7.3.2 Simulation Results 124

7.4 Summary and Conclusions 128

8 Fast and Globally Convergent Nonlinear System Model for 3D Magnetostrictive Systems 130

8.1 Magnetostrictive System Model featuring Continuation 131

8.2 Inverse model performance 134
8.2.1 Performance for 1D inputs 135
8.2.2 Performance for random 3D inputs 136
8.2.3 Choice of the iterative step size α 137
8.2.4 Choice of start solution 138

8.3 Summary and Conclusions 138

9 Conclusions and Future Work 140

9.1 Summary and Conclusions 140

9.2 Research Contributions 143

9.3 Future Work 143

Bibliography 145

List of Figures

Figure **Page**

2.1 Maximum absolute values of the term (S) and the term-ratio (L) of the 20-order ATET solution for eq. (2.7) for $x_0 \in \{0, 2.5, 5\}$, $a = 0$, $b = 5$, and (a) $A = -10$ and $B = 10$; (b) $A = 0$ and $B = 10$; and (c) $A = 10$ and $B = 10$. 21

2.2 Comparison of the exact solution (2.8) and the eighth order ATET solution (2.9) for $x_0 = 2.5$ and $B = 10$. 22

2.3 Comparison of the numerical and ATET solutions (2.14) with $M_1 = 4$ and $M_2 = 3$ for $F(x)$ and $G(x)$ written about (a) $x_0 = 0$, (b) $x_0 = 0.5$, and (c) $x_0 = 1$ for eqs. (2.12). 26

2.4 Comparison of the numerical and ATET solutions with $M_1 = M_2 = 4$ for $F(x)$ and $G(x)$ written about (a) $x_0 = 0$, (b) $x_0 = 0.5$, and (c) $x_0 = 1$ for eqs. (2.12). 27

2.5 Comparison of the numerical and ATET solutions ($M_1 = 4$, $M_2 = 10$, and $x_0 = 0.5$) for $F(x)$ and $G(x)$ with respect to (a) Re, (b) N_1, (c) N_2, and (d) N_3 for eqs. (2.12). 28

2.6 The profile of the fin tip point temperature $\theta(0)$ obtained from eq. (2.18) for the heat transfer application. 31

2.7 Comparison of the numerical solution and sixth order ATET solution (2.17) for the heat transfer application for (a) $k = 1.5$, (b) $k = 2.5$, (c) $k = 4$, and (d) $k = 6$. 32

2.8 The temperature profile obtained from the ATET solution (2.17) for arbitrary k for the heat transfer application for (a) $\epsilon^2 = 0.2$, (b) $\epsilon^2 = 0.4$, (c) $\epsilon^2 = 1.2$, and (d) $\epsilon^2 = 1.8$. 33

2.9 Solution profile based on (a) the second order, and (b) fourth order ATET solutions for application 3. 35

3.1 A schematic view of a tip point loaded cantilever beam. 38

3.2 Comparison of the numerical solution and the fifth order ATET solutions (3.17)-(3.19) with (a) $s_0 = 0$, (b) $s_0 = 0.5$, and (c) $s_0 = 1$ for the deflection components of the entire nondimensional beam length for several loading parameters. 43
3.3 Exact large deflection profile of a cantilever beam of unit length subject to nondimensional pure end-moments. 48
3.4 A deflected cantilever beam of unit length and circularity 5 subject to a pure end-moment. 49
3.5 Comparison of the numerical and the sixth order ATET solutions ($\mathcal{M}_1 = 8$ for $\alpha = 2$) for the angular deflections of the entire nondimensional beam length for pure end-forces. 50
3.6 Comparison of the numerical and the sixth order ATET solutions ($\mathcal{M}_1 = \mathcal{M}_2 = \mathcal{M}_3 = 8$ for $\alpha = 2$) for the horizontal and vertical deflections of the entire nondimensional beam length for pure end-forces. 51
3.7 Force angle effects on the beam's deflections (a) $\alpha = \frac{1}{3}$ and $\mathcal{M}_1 = \mathcal{M}_2 = \mathcal{M}_3 = 3$, (b) $\alpha = 1$ and $\mathcal{M}_1 = \mathcal{M}_2 = \mathcal{M}_3 = 4$, and (c) $\alpha = 3$, $\mathcal{M}_1 = \mathcal{M}_2 = \mathcal{M}_3 = 8$ for $\phi < \frac{2\pi}{3}$ otherwise $\mathcal{M}_1 = 12$ and $\mathcal{M}_2 = \mathcal{M}_3 = 14$. 52
3.8 Comparison of the numerical and the tenth order ATET solutions with $s_0 = 1$ for the trajectory of the beam's end-angle for pure end-forces. 53
3.9 Tenth order ATET solutions with $s_0 = 1$ for the angular deflections of the entire nondimensional beam length for large pure end-forces of angles $\frac{\pi}{3}$, $\frac{2\pi}{3}$, and π. 54
3.10 Comparison of the numerical and the tenth order ATET solutions for the angular deflections of the entire nondimensional beam length for dominant end-moments. 55
3.11 Comparison of the numerical and the tenth order ATET solutions for the horizontal and the vertical deflections of the entire nondimensional beam length for dominant end-moments. 56
3.12 Comparison of the numerical and the tenth order ATET solutions ($\mathcal{M}_1 = 15$ for $\alpha = \frac{40}{9}$, and $\mathcal{M}_1 = 16$ for $\alpha = 5$) for the angular deflections of the entire nondimensional beam length for pure and dominant end-forces. 56
3.13 Comparison of the numerical and the tenth order ATET solutions ($\mathcal{M}_2 = \mathcal{M}_3 = 12$ for $\alpha = \frac{35}{9}$; $\mathcal{M}_1 = 15$ and $\mathcal{M}_2 = \mathcal{M}_3 = 18$ for $\alpha = \frac{40}{9}$; and $\mathcal{M}_1 = 16$ and $\mathcal{M}_2 = \mathcal{M}_3 = 24$ for $\alpha = 5$) for the horizontal and vertical deflections of the entire nondimensional beam length for pure and dominant end-forces. 57
3.14 Comparison of the numerical and the eighth order ATET solutions for the beam's (a) angular and (b) axial deflections for $\alpha = 4$, $\phi = \frac{\pi}{3}$, and several values of β causing inflection points. 58

3.15 Comparison of the numerical and the 20th order ATET solutions for the beam's angular (a) deflection, (b) slope and (c) curvature for $\alpha = 1.5$, $\beta = \pm 2\pi$, and $\phi = \frac{2\pi}{3}$. 59

4.1 A snapshot of *BeamSol 1.0* corresponding to the ten cases of input data given in Table 4.1. The annotations in red are added manually for illustration purposes. 73

5.1 (a) The determinant sub-locus of the matrix $\overline{\mathbf{K}}$ corresponding to planar stress for $K = 3 \times 10^4$, $3\lambda_{100} = 520 \times 10^{-6}$, and $3\lambda_{111} = -20 \times 10^{-6}$, (b) slice plot for $T_1 = 0$ or $T_2 = 0$, and (c) slice plot for $T_4 = 0$. 83

5.2 Volume of valid magnetization directions (shaded region) for $\overset{-2}{\mathbf{m}}$ in the vicinity of $\overset{-2}{\mathbf{c}} = [0; -1; 0]$ (black arrow), shown in relation to the 5 other easy magnetization directions (red arrows) for a material with cubic anisotropy and $\overset{k}{K} > 0$. 87

5.3 The cartesian surface plot of Gibbs free energy (5.1), scaled down by K, relative to the second easy direction $\overset{-1}{\mathbf{c}}$ with $K = 30$ (kJ/m^3), $K_{100} = 0$ (kJ/m^3), $3\lambda_{100} = 520$ (ppm) and $3\lambda_{111} = -20$ (ppm) for $\mathbf{H} = [1; 0; 0]$ (kA/m) and $\mathbf{T} = -[100; 0; 40; 40; 40; 0]$ (MPa); real solutions of eq. (5.27) shown by blue arrows (orientation most minimizing energy by a double-headed arrow); approximate solution (5.9) shown by a red arrow. 88

5.4 Comparison of averaged hysteretic measurements and nonhysteretic model for $\langle 100 \rangle$ $Fe_{81.5}Ga_{18.5}$ grown with FSZM at (a),(b) constant compressive stress values of 0.32, 8.00, 13.40, 23.10, and 32.30 MPa, and (c),(d) constant field values of 1.85, 3.24, 5.65, and 8.88 kA/m. Strain is the superposition of the mechanical strain (T/E) and the magnetostriction (λ). 95

5.5 Magnetostriction calculated with (a) eq. (5.7) and (b) eq. (5.17), and compared with the averaged hysteretic data at constant field values of 1.85, 3.24, 5.65, and 8.88 kA/m. For each case, material parameters are optimized for the full family of actuation and sensing measurements using identical objective error functions. 97

5.6 Expected execution time (averaged over 2 computers) of the exact and approximate constitutive models (coded as compiled MATLAB functions). 99

5.7 Comparison of hysteretic measurements and hysteretic model for $\langle 100 \rangle$ $Fe_{81.5}Ga_{18.5}$ grown with FSZM at (a),(b) constant compressive stress values of 0.32, 8.00, 13.40, 23.10, and 32.30 MPa, and (c),(d) constant field values of 1.85, 3.24, 5.65, and 8.88 kA/m. Strain is the superposition of the mechanical strain (T/E) and the magnetostriction (λ). . 100

7.1 Schematic of a Galfenol-aluminium composite structure. The x-y plane of the coordinate system is coincident with the bottom plane of the Galfenol strip, and the x-z plane is a plane of symmetry ($y_0 = 0$). 122
7.2 (a) A schematic plot of 1D input magnetic field: $H(t) = H_b - H_a \sin(2\pi\omega t)$, and (b) schematic of deflected plate configurations (dimensions in inches) at different fractions of time period (T) corresponding to the frequency ω. 124
7.3 Dynamic actuation results, obtained using the proposed model, with 1D unbiased input magnetic field ($H(t) = -15\sin(2\pi\omega t)$ kA/m) for two periods at frequencies: (a),(b) 0.1 Hz; (c),(d) 100 Hz; and (e),(f) 350 Hz. The displacement-field curves are for the last period. 125
7.4 Dynamic actuation results with biased input magnetic field $H(t) = 3.50 - 3.25\sin(2\pi\omega t)$ kA/m at different frequencies: (a) 50 Hz, (b) 200 Hz, (c) 350 Hz, and (d) 500 Hz. 126
7.5 Plots of (a) unbiased harmonic magnetic field input, and (b) the response at 100 Hz. 128
7.6 (a) Plot of non-smooth 1D magnetic field input, and (b) the response at 50 Hz. 129

8.1 Direct and inverse model simulations for $\langle 100 \rangle$ $\mathrm{Fe}_{81.5}\mathrm{Ga}_{18.5}$ grown with FSZM for 1D (a),(b),(c) actuation; and (d),(e),(f) sensing. Any run taking more than 500 iterations is assumed to be divergent. 136

List of Tables

Table **Page**

4.1 Input data used for Figure 4.1. For all cases: $l = 1$ (m), $I = 10^{-4}$ (m^4), and $E = 10$ (MPa). 74

5.1 Optimized parameters for the nonhysteretic model. 96
5.2 Comparison of the normalized error of the exact and approximate nonhysteretic models. Model parameters for the latter are: $M_s = 1,225.00$ (kA/m), $E = 75.31$ (GPa), $\lambda_{100} = 166.31$ (ppm), $K = 34.84$ (kJ/m^3), $K_{100} = 498.00$ (J/m^3), and $\Omega = 1,014.70$ (J). 96
5.3 Optimized parameters for the hysteretic model. 101

7.1 Parameters for the Galfenol direct model, given in Chapter 5. 123
7.2 Simulation runtimes for the existing and proposed models. 127

8.1 Performance of the existing and proposed inverse models for a large 3D generic dataset. 137

List of Symbols

Symbols from Greek alphabet.

Symbol	Description
α	Newton step size.
$\boldsymbol{\lambda}$	Magnetostriction tensor.
λ_{100}	Magnetostriction constant.
λ_{111}	Magnetostriction constant.
μ_0	Vacuum permeability.
ξ	Volume fraction.
ρ	Density.
σ	Stress.
Ω	Smoothing factor.

List of mathematical symbols.

Symbol	**Description**
$\cdot$	Vector dot product operator.
$\times$	Vector cross product operator.
$\lvert\mathbf{A}\rvert$	Determinant of matrix $\mathbf{A}$.
$\lvert x\rvert$	Absolute value of the scalar x.
$[x_1; x_2]$	Column vector $\mathbf{x}$ with elements x_1 and x_2.
A_{ij}	The $(i,j)^{th}$ element of matrix $\mathbf{A}$.
$\mathbf{B}$	Magnetic induction.
$\mathbf{c}$	Matrix of the easy axes.
$\mathbf{C}$	Stiffness matrix.
$\mathbf{G}$	Gibbs free energy.
$\mathbf{H}$	Magnetic field vector.
$\mathbf{I}$	The 3×3 Identity matrix.
J	Jacobian vector/matrix.
H	Hessian matrix.
k	Number of the easy axis.
K	Anisotropy energy constant.
K_0	Anisotropy energy constant.
$\mathbf{m}$	Magnetization unit direction.
M_s	Saturation magnetization.
r	Total number of the easy axes.
$\mathbb{R}$	The set of the real numbers.
$\mathbf{s}$	Compliance matrix.
$\mathbf{S}$	Strain tensor.
$tr(\mathbf{A})$	Trace of matrix $\mathbf{A}$.
^{T}	Vector/matrix transpose operator.
$\mathbf{T}$	Stress tensor.
x_i	The ith element of vector $\mathbf{x}$.

Chapter 1

Introduction and Background

This dissertation presents robust and efficient mathematical techniques for modeling and simulation of smart material systems. Smart or active materials exhibit controllable changes in shape and properties in response to external stimuli. Such changes are accompanied with coupling of different physical effects and conversion of energy from one type to another. For instance, piezoelectric and electrostrictive materials convert electrical energy to mechanical energy and vice versa; magnetostrictive materials and magnetorheological fluids exhibit coupling of magnetic and mechanical effects; shape-memory alloys and polymers respond mechanically to thermal activation; and pH sensitive polymers swell in response to changes in external pH.

Passive materials (such as iron, steel, or aluminum) do not exhibit controllable changes in shape and properties in response to external stimuli. In addition, their response is not necessarily two-way coupled. For example, application of heat may cause aluminum to deflect, but deflection of aluminum does not create substantial heat. This one-way response is not as complex to model as that of smart materials, but some materials (for example, epoxy), when exhibiting large deflection, reveal a complex behavior, which is hard to model mathematically.

For the sake of completeness, techniques for both passive and active materials are developed. In the first few chapters, the simpler materials, i.e., the passive materials, are discussed; then, the focus is given to the more complicated materials, i.e., the smart materials, in the remaining chapters. In the following, overviews of passive and smart materials, together with the major existing modeling tools are given, in particular, for the magnetostrictive smart materials. Each section is followed by relevant dissertation contributions.

1.1 Passive materials

Passive materials have long been used, for example, for the construction of mechanisms to transmit motion. If exhibiting considerable rigidity, the corresponding materials have been utilized for designing rigid mechanisms, whose components do not deform considerably under the load exertion. The four-bar mechanism is one well-known example. See Ref. [1] and the references therein, for more details. On the other hand, if exhibiting flexibility, the corresponding materials have found applications, within the last decades, for the design of a new type of mechanisms called "compliant mechanisms". Unlike rigid mechanisms, compliant mechanisms attain their mobility from the flexibility of their members which, in essence, is the cause of transmitting or transforming motion, load, or energy. Part-count reduction, reduced assembly time, ease of manufacturing, increased reliability and precision, wear, weight and maintenance reduction are the major advantages of compliant mechanisms over their rigid counterparts. These advantages may be classified as production cost reduction and increased mechanical performance. However, compliant mechanisms pose several challenges that may not be found in their rigid counterparts. Several factors, such as the location, direction and magnitude of applied forces or even the material that is used for the synthesis, may affect the motion of a compliant mechanism. The mathematical modeling of these effects is an open and a very challenging problem. See Ref. [2] for more details.

Beams are slender structural members that have been the building block of many compliant mechanisms. Beams have also found applications in mechanical engineering in the design of shafts, gas turbines, rotor blades, engine components, wind turbine rotors, precision engineering flexures and so on, in aerospace engineering in the design of propellers, helicopter rotor blades, high aspect ratio aircraft wings and so on, in civil engineering for the synthesis of buildings, highways, bridge constructions, etc. The identification of a beam's governing load-deformation relations, especially when deflections are large, has emerged as a challenging problem primarily due to the inherently severe nonlinearities caused by the geometry and the material of the beam and even the type and position of the applied loading. See Ref. [3] for the nonlinear composite beam theory.

Work has been done on linear beam theory to obtain explicit solutions for the small deformation of cantilever beams subjected to tip point loading. However, these solutions are not valid once the beam's axis slope is significant. Large deflection solutions are now necessary to address the new beam applications. The first demonstration of the exact implicit elliptic integral solutions of an Euler–Bernoulli cantilever beam of uniform cross section for the case of a vertical tip point force appears to be Ref. [4]. These solutions were generalized in Ref. [5] for the case of general combined tip point loading.

However, elliptic integral solutions have imposed challenges on the solutions evaluations and implementations. These have motivated researchers to employ or in some cases devise alternative approaches, such as numerical integration methods, shooting methods, finite-element methods. See Ref. [2] for a review. Moreover, with employing nonlinear shooting and Adomian's decomposition methods, numerical and approximate large deflection solutions for concentrated intermediate and end point loading were obtained in Ref. [6]. Recently, a numerical integral approach was developed in

Ref. [7] which may be applicable for complex load and variable beam properties. The uniqueness of large deflections of a uniform cantilever beam under a concentrated rotational tip load was also studied in Ref. [8]. In addition, cantilever beams with nonlinear elastic materials have been studied. Ref. [9] investigated the large deflection of cantilever beams made of a Ludwick type material subjected to combined concentrated vertical tip point and uniformly distributed forces. The same problem was recently studied in Ref. [10] with a bending moment formulation.

Due to the absence of explicit analytical large deflection solutions, research has been shifted toward approximating the beam's flexibility with Pseudo-Rigid-Body models (PRB models), which consist of rigid segments joined with torsional springs that compensate the compliance. These models basically employ the kinematic loop-closure equations, thus, have been proved to simplify the analysis and the design of beam based devices. In this regard, Ref. [11] proposed a pseudo-rigid-body model consisting of two rigid links and an intermediate torsional spring whose geometric specifications were identified with a one-dimensional optimization search procedure, which minimized the tip point deflection errors exploiting the numerical elliptic integral data. The outcome was a PRB 1R model, which mimics the trajectory of the beam's end point for a certain domain of pure end–force parameters. An improved variable parametric pseudo-rigid-body model was then proposed in Ref. [12] which increased the validity range of the PRB 1R model. By adding one link and one joint to the previous PRB 1R models, Ref. [13] proposed a PRB 2R model, which is valid for general combined loading, especially cases causing inflection points.

1.1.1 Contributions

Motivated by the importance of closed form solutions for parametric studies of engineering and scientific boundary value problems, Automatic Taylor Expansion technique (ATET) is discussed in Chapter 2. Documented in Ref. [14], ATET is shown to be effective when written about the domain center of the boundary value problem. For a system of ordinary differential equations, it is shown that one may control the accuracy of each solution independently of that of the other solutions, hence, efficiently describing the nonlinearity of the entire system. Utilizing ATET, applications from micropolar fluids, heat transfer, and theoretical biology are studied. To facilitate parametric studies, approximate parametric closed form solution for each application is given. In particular, for the biology and heat transfer applications, the proposed solutions are valid, even though the differential solver of Mathematica fails to return numerical solutions. For the case of micropolar fluids, the accuracy of each stream function solution can be controlled independently of that of the remaining solution.

Discussed in Chapter 3 and documented in Ref. [15], parametric large deflection components of Euler–Bernoulli cantilever beams subjected to combined tip point loading are developed. The characteristic equation of the beam's deflection is introduced, and with employing ATET, deflection solutions to the Euler–Bernoulli boundary value problem are presented in terms of the loading parameters. The obtained ATET deflection solutions, verified by comparison with the numerical solutions, are valid for the entire beam length, and independently and efficiently adaptable for very large loading conditions and easily implementable for engineering analyses and syntheses. Exploiting these solutions as theoretical tools, the beam's angular and axial deflections behavior for several tip point loading conditions are studied. Besides the widely known axial inflection points, beam's angular inflection points are also recognized for the mixed loading condition, and it is shown that the parametric solutions are intelligent in recognizing the right deflection branch for both inflection types.

In addition, cartesian and piecewise parametric large deflection solutions are derived in Chapter 4 and documented in Ref. [16]. Employing the latter solutions, BeamSol, a stand-alone large deflection beam solver, is coded in Visual C++.

1.2 Smart materials

In contrast to passive materials, the coupling of physical effects in smart materials enables tuning of material properties, thus, making smart materials attractive for design of sensors [17], actuators [18], energy harvesters [19], and vibration controlling devices [20]. See Ref. [21, 22] for more on smart materials.

Smart materials typically exhibit nonlinear and hysteretic behavior, even though certain smart materials can be characterized using linear models within a specified operational regime. For instance, piezoelectric materials like PZT, PVDF, and $BaTiO_3$, when poled, exhibit approximately linear behavior for low to moderate inputs [23]. These linear constitutive models are often sufficient for efficient transducer designs. In contrast, magnetostrictives, electrostrictives, and shape memory alloys or polymers exhibit higher order of nonlinearity and hysteresis, and cannot be fully characterized with linear equations.

Magnetostrictive materials are a class of smart materials that exhibit nonlinear magnetomechanical coupling. These materials undergo dimensional changes when exposed to a magnetic field, and exhibit magnetization changes when they experience external stress fields. Two common magnetostrictive materials are terbium-dysprosium-iron and iron-gallium alloys, known as Terfenol-D and Galfenol, respectively. The former has relatively large magnetostriction ($\approx$ 1600 ppm) at a moderate magnetic field ($\approx$ 200 kA/m), making it well suited for actuator designs; see for example Chakrabarti and Dapino [24]. Referring to Ref. [26], Galfenol exhibits moderate magnetostriction ($\approx$ 350 ppm) at low magnetic fields ($\approx$ 8 kA/m); possesses high tensile strength ($\approx$ 500 MPa), and a high Curie temperature (675 °C); and demonstrates limited variation in magnetomechanical properties for temperatures between -20 and

80 °C. When composed of less than 20% gallium, Galfenol retains the machinability and ductility of iron, thus, it can be easily produced in sheets or wires; welded, threaded or extruded into unprecedented complex geometries to gain significant load-bearing capabilities. In contrast, Terfenol-D is brittle, and always requires stress biasing to avoid tension. See Atulasimha and Flatau [27] for a review of iron-gallium alloys.

The intrinsic nonlinearity and hysteresis manifested by magnetostrictives, electrostrictives, and shape memory alloys or polymers add complexity to devise models. To date, several methods exist to efficiently model the behavior of the aforementioned materials. At one extreme, a *phenomenological approach* fits a curve or surface to measurement data, which provides efficiency but ignores the underlying physics. At the other extreme, *microscopic models* consider all known energies and are very accurate. For example, a well-known paradigm to determine the magnetization evolution in a ferromagnetic material is to solve Landau-Lifshitz equation [28]. To this end, a Gauss-Seidel projection method was proposed by Wang et al. [29]; a boundary-corrected algorithm for general geometry was developed by García-Cervera et al. [30]; built on fast multipole method, Van de Wiele et al. [31] presented a numerical finite-difference scheme that employs far and near field interactions to describe the interactions between finite-difference cells; the recent high-order finite-element model devised by Kritsikis et al. [32] can handle nonlocal magnetostatic interactions in logarithmic time with nonuniform fast Fourier transform.

Finally, a third kind of approach, namely, the *macroscopic modeling*, uses an intermediate approach by relating the macroscopic response of the material to simplified descriptions of the microscopic behavior. Macroscopic models, therefore, strike a balance between efficiency, accuracy, and predictive capability. For magnetostrictive materials, in particular, the classical macroscopic models are the Preisach model [33], Globus model [34], Jiles-Atherton model [35], and Stoner-Wohlfarth model [36]. Ref. [37] compares these models in detail. For Terfenol-D, Carman and Mitrovic [38] formulated a model by expanding the Gibbs free energy in a truncated Taylor series, and found the coefficients experimentally. Later, Zheng and Sun [39] considered higher order terms in the expansion to improve the applicability of the model for larger magnetic field inputs. Recently, a fully coupled 3D energy-averaged model was presented by Chakrabarti and Dapino [24]. Armstrong [40] proposed an incremental hysteretic magnetoelastic constitutive theory of pseudo-cubic ferro-magnetostrictive alloys that can be applied to both Terfenol-D and Galfenol. The bulk magnetization and magnetostriction are the expected values of a large collection of magnetic moments. The probability density function is a Boltzmann distribution, where minimum energy orientations are more probable. The Armstrong model is computationally inefficient, as it searches for global energy minima. Atulasimha et al. [41] improved efficiency by considering only 98 fixed orientations. Evans and Dapino [42] greatly enhanced the previous model by solving for the local minima along only six easy directions of Galfenol. The computational cost of this model was further reduced by Chakrabarti [43].

1.2.1 Contributions

Discussed in Chapter 5 and documented in Ref. [44], a reformulation of the Discrete Energy-Averaged model for calculation of the 3D hysteretic magnetization and magnetostriction of iron-gallium (Galfenol) alloys is presented. An analytical solution procedure based on eigenvalue decomposition is developed. This procedure avoids the singularities present in the existing approximate solution by offering multiple local minimum energy directions for each easy crystallographic direction. This improved robustness is crucial for use in black-box finite-element codes. Analytical simplifications of the 3D model to 2D and 1D applications are also presented. In particular, the 1D model requires calculation for only one easy direction, while all six easy directions must be considered for general applications. Compared to the approximate solution procedure, it is shown that the resulting robustness comes at no expense for 1D applications, but requires almost twice the computational cost for 3D applications. To find model parameters, the average of the hysteretic data is employed. This obviates any need for anhysteretic curves, which require additional measurements. An efficient optimization routine is developed that retains the dimensionality of the prior art. The routine decouples the parameters into exclusive sets, some of which are found directly through a fast preprocessing step to improve accuracy and computational efficiency.

In addition, as discussed in Chapter 7 and documented in Ref. [45], a computationally efficient and robust nonlinear modeling framework is presented for smart material systems. The framework consists of a novel 3D inversion scheme for nonlinear modeling of smart material systems, and a reduced dimensional model (2D) for smart composite plate structures. Building on the Newton technique, the inversion scheme can be applied to any nonlinear smart material system with a differentiable direct model. The 2D nonlinear magnetostrictive plate model and the 3D inversion scheme are integrated with a finite-element software to analyze an aluminum plate embedded with a Galfenol strip. The resulting nonlinear finite-element framework is utilized to obtain complete and minor magnetostriction curves corresponding to the tip of the Galfenol patch with applying unbiased and biased magnetic fields, respectively. A significant advantage in computational time and numerical convergence is demonstrated via comparison with an existing approach for magnetostrictive material modeling. The framework is ideal for the fast design and optimization of nonlinear smart material based transducers.

Furthermore, Chapter 8 presents a globally convergent and fully coupled magnetomechanical model for 3D magnetostrictive systems. As documented in Ref. [46], the inverse model finds the unknown magnetic field and stress vectors for any specified magnetic flux density and strain vectors. This inversion procedure is iterative, and is proposed for arbitrary magnetostrictive materials. The inversion requirement is a continuous and second order differentiable direct model for any magnetostrictive material. The approach is globally convergent, which makes it ideal for use in finite-element frameworks. The premise of the proposed iterative system model is to constitute a recursive correction formula based on second order approximations of a novel scalar error function which allows to achieve a faster convergence rate. A continuation approach is then used to achieve global convergence for arbitrary input parameters. To illustrate, Galfenol is chosen as the magnetostrictive material. Finally, the computational efficiency of the proposed approach is shown to compare favorably against existing models.

1.3 Organization of the Dissertation

The next chapter presents automatic Taylor expansion technique, and illustrates it with applications from micropolar fluids, heat transfer, and theoretical biology. Utilizing this technique, Chapter 3 presents parametric large deflection solutions for Euler–Bernoulli cantilever beams subjected to combined tip point loading. Chapter 4 presents cartesian and piecewise parametric large deflection solutions, which are implemented as the stand-alone executable *BeamSol*. Chapter 5 presents a reformulation of the discrete energy-averaged model, and an exact solution procedure for the calculation of the 3D hysteretic magnetization and magnetostriction of iron-gallium (Galfenol) alloys. Jacobian and Hessian terms corresponding to this model are presented in Chapter 6. Built on these derivative terms, computationally efficient and robust nonlinear system modeling frameworks for one-way coupled and fully coupled smart material systems are presented, respectively, in Chapters 7 and 8. Finally, Chapter 9 gives conclusions, and addresses suggestions for future work.

Chapter 2

Effective Start Point for the Automatic Taylor Expansion Technique

This chapter discusses the Automatic Taylor Expansion technique (ATET) for the approximate analytical solution of nonlinear ordinary boundary value problems appearing in, particularly, engineering and scientific applications. Documented in Ref. [14], it is shown that highly convergent ATET solutions can be obtained if the solution is expanded about the domain center of the boundary value problem. Employing ATET in a symbolic fashion, approximate analytical solutions are obtained for BVPs arising in micropolar fluids, heat transfer, and theoretical biology. In particular, for the biology and heat transfer applications, which lead to singular boundary value problems, the proposed solutions are valid, while the differential solver of Mathematica fails to return numerical solutions. Additionally, it is shown that the accuracy of each stream function solution for the micropolar fluids application can be controlled independently of that of the remaining solution.

The rest of this chapter is organized as follows. After a brief introduction, Section 2.2 gives the problem statement. Section 2.3 discusses ATET, and introduces a generally optimal start point choice. Section 2.4 discusses three significant applications arising in engineering and science, and gives parametric ATET solutions validated by numerical results. Finally, summary and conclusions are given.

2.1 Introduction

The phenomena occurring in the nature may not be fully perceived unless their mathematical modelings are carried out, solved, and the results scrutinized. However, most of the phenomena are mathematically nonlinear, the fact that hinders us from a tangible understanding of their behavior. Although numerical methods outside the singularities are almost always effective choices, sampling highly nonlinear surfaces not only is inefficient, the obtained digital data are often unreadable and insufficient to recognize a pattern by the human-being.

To this end, through the past decades, several approximate analytical methods have been devised, by numerous researchers, to circumvent the difficulties encountered in the solution of the nonlinear differential equations. These methods, in essence, deliver approximate analytical solutions, which are crucial to parametric studies of a desired problem arising possibly in diverse fields of science and engineering. Among these methods, perturbation method [47] appears to be pioneer, arguably limited, in solving nonlinear differential equations. Lyapunov's artificial small parameter method [48] and its variant developed later as the δ-expansion technique [49] are based on embedding a small parameter, through which power series expansion solutions are computed. These methods have one requirement in common which is the existence of small/large parameters in the target differential equations.

In essence, recent work has been shifted toward alleviating this shortcoming. Adomian's decomposition method (ADM) [50] irrespective of the existence of the small/large parameters is capable of solving highly nonlinear differential equations. Built on this technique, Ref. [51] constructs an augmented system based on an inhomogeneity function to solve inhomogeneous differential equations without any so-called noise terms. A modification of ADM for solving singular boundary value problems is also given in Ref. [52]. In addition, homotopy analysis method (HAM) [53] exploits the topological concept of a linear convex homotopy, and offers an auxiliary parameter $\hbar$ to further control the convergence rate of the obtained approximate analytical solutions. The essence of the auxiliary parameter $\hbar$ is elaborated in Ref. [54], and further improvements on the convergence of HAM are addressed in Ref. [55]. On the other hand, the homotopy perturbation method (HPM) [56] specialized HAM by setting $\hbar = -1$, which has been shown, in the literature, to be an effective choice for many nonlinear problems. Ref. [57] gives a comparison of HAM and HPM solutions for the temperature distribution of a straight rectangular fin with a power-law temperature dependent surface heat flux, which is also studied in this chapter. Furthermore, based on the Lagrange multipliers and variational theory, variational iteration method (VIM) [58] was introduced, which has been shown to be effective, in general, for the solution of initial value problems (IVPs). However, Tari [59] proposed a modified variational iteration method, which generalized VIM for the solution of boundary value problems (BVPs) as well.

Finally, Taylor's method has been a well-known technique for the solution of nonlinear differential equations. Ref. [60] has shown that this method once flavored with automatic differentiation, called Automatic Taylor Expansion technique (ATET), is well capable of numerically approximating the unknown solutions of nonlinear ordinary IVPs. However, IVPs are of infinite computational domains, thus, require interval analysis. This often leads to very high order polynomial approximations with iterative adjustment of the step size taken along the entire solution domain which would often lead to computational inefficiencies. The numerical ATET has also been coded to developing black-box numerical softwares as in Refs. [61–63].

In contrast to IVPs, BVPs attain relatively smaller computational domains, which can obviate interval analysis. However, ATET loses its explicitness for BVPs, as it delivers implicit solutions, which depend on unknown constants. Nonetheless, the unknowns can be identified in a second step via imposing the boundary conditions. However, this may lead to multiple solutions, or even to no solutions for singular BVPs. In this chapter, we show that expanding the solutions about an appropriate point can alleviate this shortcoming. In particular, if the domain center of the BVP is a nonsingular point, expanding about this point would lead to highly convergent solutions.

2.2 Statement of the Problem

Let $\mathcal{F}(z, \mathcal{Z}_m(z)) = 0$ be the m-order ordinary differential equation where $u^{(i)}(z) = \frac{d^i u(z)}{dz^i}$ and $\mathcal{Z}_i(z) = (u(z), u^{(1)}(z), \ldots, u^{(i)}(z))$ for $i = 0, \ldots, m$. Let further $\mathbf{G} = \cup_{i=1}^{m} g_i(z_i, \mathcal{Z}_{m-1}(z_i))$ be the set of m initial or boundary conditions constraining $\mathcal{F}$ at the given points z_i. In addition, assume that $\mathcal{F}$ may be written as

$$\mathcal{F}(z, \mathcal{Z}_m(z)) = -f(z) + \sum_{i=0}^{m} \mathcal{A}_i\left(z, \mathcal{Z}_{i-1}(z)\right) u^{(i)}(z) = 0. \tag{2.1}$$

When the coefficients $\mathcal{A}_i\left(z, \mathcal{Z}_{i-1}(z)\right)$ are generally defined, the differential equation $\mathcal{F}(z, \mathcal{Z}_m(z))$ becomes nonlinear, and a closed form solution for $u(z)$ is, in general, not attainable via traditional techniques. Our goal is to find a symbolic but approximate solution $u(z)$, which is accurate enough for engineering parametric studies.

2.3 Basic Concepts of the Automatic Taylor Expansion Technique (ATET)

First, a brief review of ATET is given in the following. Then, the start point choice, multiple solution branches, and a generalization to a system of equations are discussed subsequently.

2.3.1 Review of ATET

Recall that the goal is to obtain a parametric approximate solution to eq. (2.1), whose exact closed form solution may not exist. ATET employs the Taylor series expansion, and approximates the solution $u(z)$ in terms of the unknown higher order derivatives as

$$u(z) = \lim_{M\to\infty} \sum_{j=0}^{M} \frac{u^{(j)}(z_0)}{j!}(z - z_0)^j, \tag{2.2}$$

where z_0 is an appropriate point defined optimally considering the m initial, or boundary conditions $\mathbf{G}$. As a result, the solution of the differential equation (2.1) and the m constraints $\mathbf{G}$ is reduced to obtaining $M + 1$ unknown coefficients of the series solution $u(z)$ given by eq. (2.2). For simplicity, we denote $\mathcal{C} = \cup_{k=0}^{M} c_k$ as the set of such unknowns, where $c_k = \frac{1}{k!}u^{(k)}(z_0)$.

A set of $M + 1$ equations is needed to determine the unknown set $\mathcal{C}$. Clearly, there are m initial and boundary conditions ($\mathbf{G}$), which can be evaluated at z_0 and written in terms of the unknowns $\mathcal{C}$. Additionally, not the entire $M + 1$ elements of $\mathcal{C}$ are actually unknown. It appears that $M - m + 1$ of the unknown constants $\mathcal{C}$ may be eliminated by considering the fact that all of the higher order derivatives $u^{(j)}(z_0)$, for $j = m, \ldots, M$, may be written in terms of the lower derivatives $u^{(j)}(z_0)$, for $j = 0, \ldots, m - 1$. This is possible by simply differentiating eq. (2.1) successively for $j = 0, \ldots, M - m$ with respect to the unknown z, evaluating the results at z_0, and reformatting it as

$$u^{(m+j)}(z_0) = \frac{1}{\mathcal{A}_m(z_0, \mathcal{Z}_{m-1}(z_0))} \left[f^{(j)}(z_0) - \sum_{k=0}^{j-1} \binom{j}{k} \mathcal{A}_m^{(j-k)}(z_0, \mathcal{Z}_{m-1}(z_0)) u^{(m+k)}(z_0) \right.$$
$$\left. - \sum_{i=0}^{m-1} \sum_{k=0}^{j} \binom{j}{k} \mathcal{A}_i^{(j-k)}(z_0, \mathcal{Z}_{i-1}(z_0)) u^{(i+k)}(z_0) \right]. \tag{2.3}$$

As a result, as j increments successively from 0 to $M - m$ all of the derivatives $u^{(m+j)}(z_0)$ are at hand in terms of the first m unknowns c_r with $0 \leq r < m$. This, in turn, allows for rewriting the solution $u(z)$ in eq. (2.2) as

$$u(z) = \sum_{j=0}^{m-1} c_j (z - z_0)^j + \lim_{M \to \infty} \sum_{j=0}^{M-m} \frac{u^{(m+j)}(z_0)}{(m+j)!} (z - z_0)^{m+j}, \tag{2.4}$$

where the second summation is explicitly at hand due to the recursive eq. (2.3). Note that the solution $u(z)$ contains, now, only m unknown constants $\mathcal{C} = \cup_{r=0}^{m-1} c_r$, which would be identified upon utilizing the m available initial or boundary conditions G.

2.3.2 Choice of the Start Point z_0

Choice of z_0 has a dichotomous effect, namely, on the simplicity and convergence of the ATET solutions. As for the former, if z_0 is taken, for instance, a point which appears in the initial or boundary conditions $\mathbf{G}$, the ATET solutions very often become relatively simpler as some of the unknown higher order derivatives in the unknown set $\mathcal{C}$ become known. To be precise, consider initial value problems, for which all of the higher order derivatives are already given by the initial conditions. For such cases, if z_0 is taken as the initial point, the ATET solutions are completely explicit without further computations. This may be considered as to why the numerical codes [61–63] were specialized only for the initial value problems.

In addition, choice of z_0 also plays an important role in the accuracy and convergence of the solutions. Note that the focus of the chapter is on boundary value problems, and a finite domain of the independent variable is under consideration, say, $z_0 \in [z_L, z_R]$, where z_L and z_R are distinct finite real numbers. While either z_L or z_R may be the first candidate for z_0, they often lead to poorly convergent solutions. Nonetheless, problems that arise from engineering applications are known to have physical and real solutions, and are assumed to be differentiable on the entire finite computational domain, as a result of which a more effective alternative start point exists for such problems.

Let $R_M(z)$ denote the residual error introduced by the truncation of the approximate ATET solutions. The identification of the optimal start point z_0 may turn into a minimization problem, whose objective function is the accumulation of the residual errors associated with each point on the computational domain. However, the maximum error would, in general, occur at the two extreme points, i.e., z_L and/or z_R, as for a chosen start point either boundary point requires the most extrapolation. Therefore, an optimal start point must minimize both residuals $R_M(z_L)$ and $R_M(z_R)$. One way of doing this is to minimize:

$$\begin{aligned} R_{LR} &= |R_M(z_L)| + |R_M(z_R)| \\ &= \left| \sum_{i=M+1}^{\infty} \frac{u^{(i)}(z_0)}{i!}(z_L - z_0)^i \right| + \left| \sum_{i=M+1}^{\infty} \frac{u^{(i)}(z_0)}{i!}(z_R - z_0)^i \right| \\ &= \sum_{i=M+1}^{\infty} \frac{\left|u^{(i)}(z_0)\right|}{i!} \left[(z_0 - z_L)^i + (z_R - z_0)^i\right] . \end{aligned} \tag{2.5}$$

Given the assumption that the higher order derivatives are analytic and bounded on the entire computational domain, it is not hard to see that R_{LR} may be minimized, in general, if $z_0 = (z_L + z_R)/2$. This is expected, since $(z_L + z_R)/2$ is the center of the problem domain, and compared to the other domain points attains the least distance from both boundary points z_L and z_R. Thus, such a choice requires the least extrapolation, and therefore results, in general, in the least overall error on the entire computational domain. Nonetheless, making a decision on the choice of the start point is application based, and often requires a trade-off between the simplicity and accuracy.

One of the common tests to checking the convergence of the series with known closed form terms is the well-known *ratio test*; for instance, see Ref. [64]. For a chosen start point z_0, a modification of the ratio test can be utilized to check the convergence of the corresponding solution. Let $z_{max} = max(|z - z_0|)$ for z on the entire computational domain, and

$$L_i = \frac{S_i}{S_j} = \frac{j!}{i!} \left| \frac{u^{(i)}(z_0)}{u^{(j)}(z_0)} \right| z_{max}^{i-j},$$

which is the ratio of the maximum absolute values of the ith and j^{th} terms of the series solution (2.4), where $j < i$ is the largest index, for which $S_j \neq 0$. After sifting out the zero terms and evaluating the term-ratio values, a good test on the appropriateness of z_0 would be to check whether the term-ratio curve attains a descending slope. This is illustrated with an example in Subsection 2.3.4.

2.3.3 Choice of the Approximation Order M

As per Stirling's formula, $M! = \sqrt{2\pi M}(M/e)^M(1 + \mathcal{O}(1/M))$, the increase of the approximation order M decreases the residual $R_M(z_0)$ for a convergent approximate solution. For such a case, if M in eq. (2.4) tends to infinity, the approximate analytical solution $u(z)$ converges to an exact solution. However, a large approximation order is computationally impractical.

Let $S_i = \frac{1}{i!}|u^{(i)}(z_0)|z_{max}^i$ denote the maximum absolute value of the ith term of the series solution $u(z)$ in eq. (2.4). Let further $M_c = \{j \mid S_i \approx 0, i \in [j+1, \infty)\}$. If the series solution is convergent, we will have

$$|u(z)| \leq \sum_{j=0}^{m-1} |c_j| z_{max}^j + \sum_{j=m}^{M_c} S_j, \tag{2.6}$$

which can be utilized as a criterion for determining the approximation order. An example is given below.

2.3.4 Example

Consider the linear ordinary boundary value problem

$$y''(x) = y(x), \quad y'(a) = A, \quad y'(b) = B, \tag{2.7}$$

where a, b, A, and B are real numbers, and the exact solution is

$$y^{Exact}(x) = \frac{1}{\sinh(a-b)}(A\cosh(b-x) - B\cosh(a-x)). \tag{2.8}$$

Employing eqs. (2.3) and (2.4), one may write the ATET solution for $y(x)$ about the arbitrary point x_0 as

$$\begin{aligned} y(x) = c_0 &\left[1 + \frac{1}{2!}(x-x_0)^2 + \frac{1}{4!}(x-x_0)^4 + \frac{1}{6!}(x-x_0)^6 + \frac{1}{8!}(x-x_0)^8 + \mathcal{O}(x^{10})\right] \\ &+ c_1 \left[x - x_0 + \frac{1}{3!}(x-x_0)^3 + \frac{1}{5!}(x-x_0)^5 + \frac{1}{7!}(x-x_0)^7 + \mathcal{O}(x^9)\right], \end{aligned} \tag{2.9}$$

where $c_0 = y(x_0)$ and $c_1 = y'(x_0)$ are easily identified upon the solution of the linear system constructed by imposing the boundary conditions of eq. (2.7). Note that the solution (2.9) is exactly an eight order Taylor series approximation of the exact solution (2.8), and converges to the exact solution if more terms are retained.

Nonetheless, we assume that no exact solution is at hand, and proceed with the truncated series solution to illustrate the ideas proposed in the foregoing subsections.

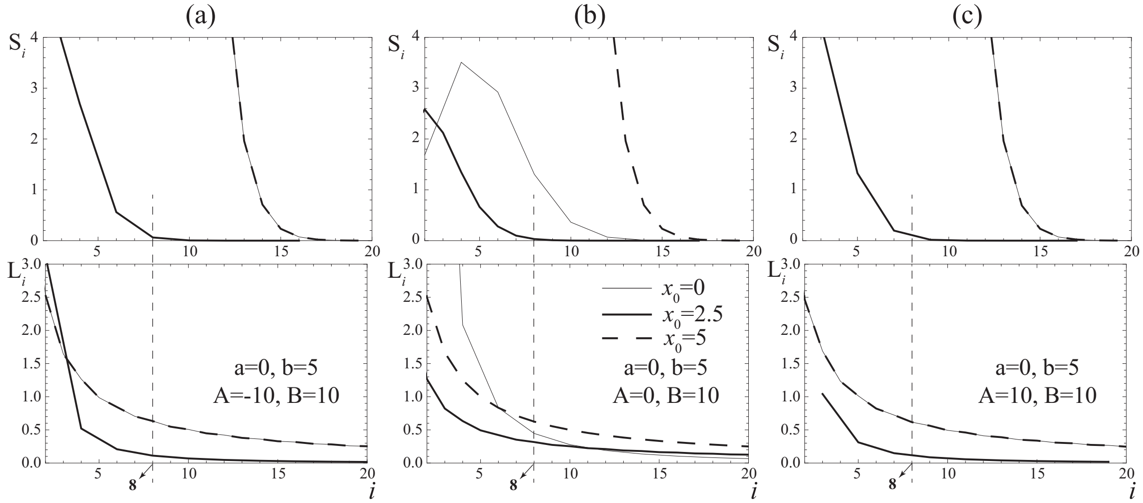

Figure 2.1: Maximum absolute values of the term (S) and the term-ratio (L) of the 20-order ATET solution for eq. (2.7) for $x_0 \in \{0, 2.5, 5\}$, $a = 0$, $b = 5$, and (a) $A = -10$ and $B = 10$; (b) $A = 0$ and $B = 10$; and (c) $A = 10$ and $B = 10$.

Figure 2.1 illustrates the maximum absolute values of the term and the term-ratio of the 20-order ATET solution $y(x)$ for the domain $x \in [0, 5]$ and the start points $x_0 \in \{0, 2.5, 5\}$. Note that all of the terms, which were identically zero, have been expunged out. All subfigures, except for some early terms, show monotonically decreasing term-ratios for the chosen start points. This signifies that all of the chosen start points lead to convergent solutions.

However, how to pick the most efficient one from the chosen start points may be decided by further noting the revealed convergence rates. For example, the solution terms associated with the start point $x_0 = 5$ are the same in all three subfigures and vanish for $i \geq 17$. Likewise, the solution terms corresponding to the start point $x_0 = 0$ behave the same in Subfigures 2.1(a) and (c), but decrease slightly as in Subfig-

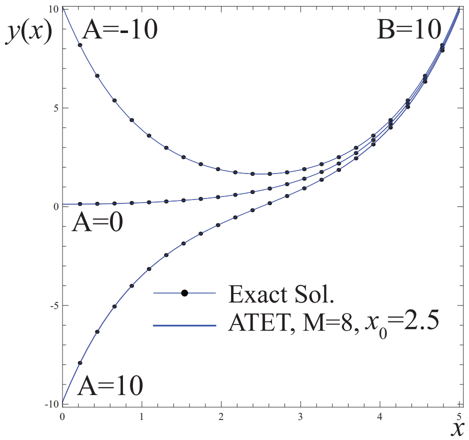

Figure 2.2: Comparison of the exact solution (2.8) and the eighth order ATET solution (2.9) for $x_0 = 2.5$ and $B = 10$.

ure 2.1(b) and vanish for $i \geq 14$. Finally, the solution terms associated with $x_0 = 2.5$, common to all subfigures, are negligible for $i \geq 9$. As a result, the most efficient choice from the chosen start points is $x_0 = 2.5$, and an eight order approximation is needed. Figure 2.2 compares such a solution with the exact solution (2.8).

2.3.5 Multiple Solution Branches

Nonlinear BVPs may have multiple solution branches, but not all such branches may be physical for a given set of input parameters. In fact, the actual solution may exist either entirely on a single branch, or collectively on two or more solution branches. The latter case rather complicates even the traditional techniques, even when exact closed form solution branches are known explicitly. However, ATET is intelligent in recognizing the right solution branch, as the branch selection is automatically taken into account when solving for the unknown constants, which make up the ATET solutions. This feature allows that a single parametric ATET solution becomes applicable to arbitrary input parameter sets which is enormously desirable for engineering parametric studies.

2.3.6 ATET for a System of Nonlinear ODEs

Let $\mathbf{i}, \mathbf{m}_i \in \mathbb{N}^k$, and $\mathbf{u}(z) = \{u_1(z), \ldots, u_k(z)\}$ be the set of k unknown univariate functions, which construct a system of k nonlinear ordinary, possibly coupled, differential equations

$$\mathfrak{F} = \cup_{i=1}^{k} \mathcal{F}_i(z, \mathcal{U}_{\mathbf{m}_i}(z)),$$

where $\mathcal{U}_{\mathbf{m}_i}(z) = (\mathbf{u}(z), D^{\mathbf{1}}\mathbf{u}(z), \ldots, D^{\mathbf{m}_i}\mathbf{u}(z))$, the ith differential equation $\mathcal{F}_i(z, \mathcal{U}_{\mathbf{m}_i}(z))$ is of order $\mathbf{m}_i$ with respect to $\mathbf{u}(z)$, and finally

$$D^{\mathbf{i}}\mathbf{u}(z) = D^{i_1}u_1(z) \cdots D^{i_k}u_k(z) = \frac{d^{i_1}u_1(z) \times \cdots \times d^{i_k}u_k(z)}{dz^{i_1+\ldots+i_k}}. \qquad (2.10)$$

Utilizing eq. (2.2), one may write the solution components of $\mathbf{u}(z)$ as

$$u_i(z) = \lim_{M_i \to \infty} \sum_{j=0}^{M_i} \frac{u_i^{(j)}(z_0)}{j!}(z - z_0)^j, \qquad i = 1, \ldots, k, \qquad (2.11)$$

where M_i is the approximation order of $u_i(z)$, and the derivatives $u_i^{(j)}(z_0)$ are unknown, but count to $\sum_{i=1}^{k}(1 + M_i)$ and can be identified by carrying out the same procedure done before for the single ordinary differential equation (2.1).

It is noteworthy that the approximation order of the solution $u_i(z)$, which is M_i, is independent of that of the other solutions. This allows to desirably and independently control the accuracy of each solution, thus, efficiently capturing the nonlinearity structure of the differential equations of the system $\mathfrak{F}$. This is illustrated below with the micropolar fluids application.

2.4 Nonlinear BVPs from Engineering and Science

In what follows, three significant applications from engineering and science are studied. For each application, a brief history is given first, and then compact parametric ATET solutions with relevant discussions are given.

2.4.1 Application 1: Micropolar Fluids

Fluids with randomly oriented particles suspended in a viscous medium whose microstructure often reveal non-symmetrical stress tensor are commonly referred to as micropolar fluids. Initiated in Ref. [65], the theory of micropolar fluids studies the local effects arising from microstructure and intrinsic micro-motion of the fluid constituents. The problem of the injective micropolar flow in a porous channel has gained a significant interest in the literature. Derived in Ref. [66], the equations governing the steady flow of an incompressible micropolar fluid past a curved surface are

$$\left\{\begin{array}{rcl} (N_1+1)F^{IV}(x) - N_1G''(x) - Re(F'''(x)F(x) - F''(x)F'(x)) & = & 0 \\ N_2G''(x) + N_1(F''(x) - 2G(x)) - N_3Re(G'(x)F(x) - F'(x)G(x)) & = & 0 \end{array}\right., \tag{2.12}$$

where the primes stand for differentiation; Re represents Reynolds number, corresponding to suction when positive, and injection when negative; $F(x)$ and $G(x)$ are stream functions; and N_1-N_3 are dimensionless micropolar parameters. Moreover, the six boundary conditions

$$F(0) = F''(0) = G(0) = F(1) - 1 = F'(1) = G(1) = 0, \tag{2.13}$$

define a symmetric flow in the channel.

Stream Function Solutions Behavior

Despite the extreme complexity of the BVP (2.12), application of ATET is quite straightforward. The goal, here, is to show the effect of the start point choice and independence of the approximation orders on ATET stream function solutions. For illustration purposes, we take very low approximation orders to show the effectiveness of the start point proposed in subsection 2.3.2, but will adopt higher orders when we proceed to a parametric study afterwards.

Employing eq. (2.11), we take $M_1 = 4$ and $M_2 = 3$, and write the fourth and third order approximate parametric ATET solutions for, respectively, $F(x)$ and $G(x)$ about an arbitrary point x_0 as

$$\begin{aligned} F(x) &= c_0 + c_1(x-x_0) + \tfrac{c_2}{2!}(x-x_0)^2 + \tfrac{c_3}{3!}(x-x_0)^3 + \tfrac{(\chi_0+\chi_2 N_1)}{(1+N_1)4!}(x-x_0)^4, \\ G(x) &= \tilde{c}_0 + \tilde{c}_1(x-x_0) + \tfrac{\chi_2}{2!}(x-x_0)^2 + \tfrac{(\chi_1+c_0\chi_2 N_3 Re)}{N_2 3!}(x-x_0)^3, \end{aligned} \tag{2.14}$$

where

$$\chi_0 = Re(c_0c_3 - c_1c_2), \quad \chi_1 = N_1(2\tilde{c}_1 - c_3) - \tilde{c}_0c_2ReN_3,$$

$$\chi_2 = \frac{((2\tilde{c}_0 - c_2)N_1 + ReN_3(c_0\tilde{c}_1 - \tilde{c}_0c_1))}{N_2},$$

and finally c_0, c_1, c_2, c_3, $\tilde{c}_0$ and $\tilde{c}_1$ are the only unknown constants, which can be identified upon imposing the boundary conditions (2.13).

Figure 2.3 illustrates the obtained low order parametric stream function solutions for three x_0 values, namely, 0, 0.5, and 1, and compares them with those of numerical solutions obtained from the numerical differential solver of Mathematica. Note that taking x_0 as either 0 or 1 drastically simplifies the solution procedure, as three of the unknown constants, i.e., either $\{c_0, c_2, \tilde{c}_0\}$ or $\{c_0, c_1, \tilde{c}_0\}$, become known parameters due to the boundary conditions (2.13). While this is computationally favorable,

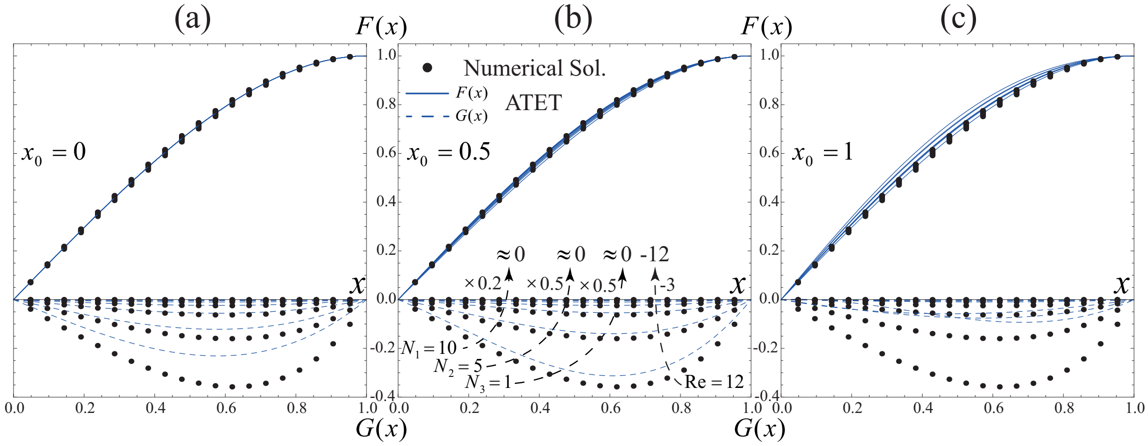

Figure 2.3: Comparison of the numerical and ATET solutions (2.14) with $M_1 = 4$ and $M_2 = 3$ for $F(x)$ and $G(x)$ written about (a) $x_0 = 0$, (b) $x_0 = 0.5$, and (c) $x_0 = 1$ for eqs. (2.12).

Figure 2.3 justifies the superior accuracy of the ATET solutions when written about the midpoint $x_0 = 0.5$.

Note that the stream function $F(x)$ does not undergo significant changes as the input parameters change. Therefore, as discussed earlier, considering lower approximation orders for $F(x)$, while higher orders for $G(x)$, appears to be computationally safe and efficient. To this end, Figure 2.4 shows fourth order ATET approximate solutions for both stream functions. Some of the solutions corresponding to $x_0 = 1$ diverged, and the solutions corresponding to $x_0 = 0$ remained unchanged since the obtained $G(x)$ turned out to be an odd function which would change only for odd values of M_2. On the other hand, as expected, the solutions associated with $x_0 = 0.5$ considerably improved even that the approximation order is increased only by one for only the second stream function. This last start point is chosen for the following parametric study of the stream functions with higher order approximation orders.

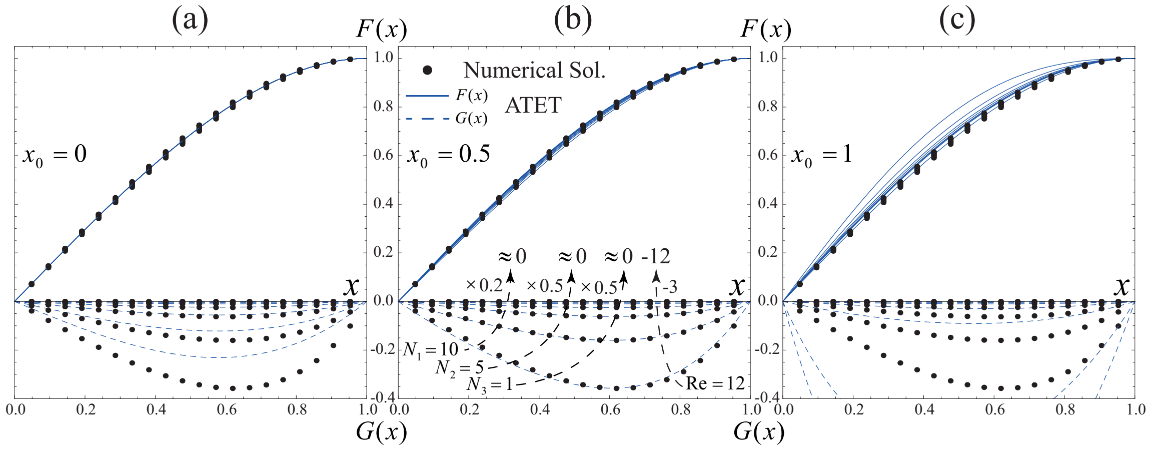

Figure 2.4: Comparison of the numerical and ATET solutions with $M_1 = M_2 = 4$ for $F(x)$ and $G(x)$ written about (a) $x_0 = 0$, (b) $x_0 = 0.5$, and (c) $x_0 = 1$ for eqs. (2.12).

Parametric Study of the ATET Stream Function Solutions

The behavior of the stream functions $F(x)$ and $G(x)$ depends on the four parameters Re, N_1, N_2, and N_3. For the sake of simplicity, four one-dimensional cases are considered. That is, for each case, three parameters are held constant, and the profile of the stream functions for the change of the remaining parameter is plotted as in Figure 2.5.

Subfigures 2.5(a)-(d) depict that the change in the input parameters have relatively less effect on $F(x)$ than on $G(x)$ which is why a higher order approximation is considered only for the latter stream function. Nonetheless, note that, compared to Ref. [66], this partial increase in the approximation order accommodates an enormous parameter range, e.g., $Re \in [-150, 50]$, $N_1 \in [0, 40]$. In addition, the increase of the parameters Re, N_1, and N_3 does make $G(x)$ diminish, but the reduction amount is minimum for the Reynolds number. In contrast, the change of N_2 has an opposite effect. Shown in Subfigure 2.5(c), the increase of N_2 increases $G(x)$, but reduces its absolute value. This is expected, since due to the second equation of eq. (2.12), N_2 is inversely proportional to the second derivative of $G(x)$.

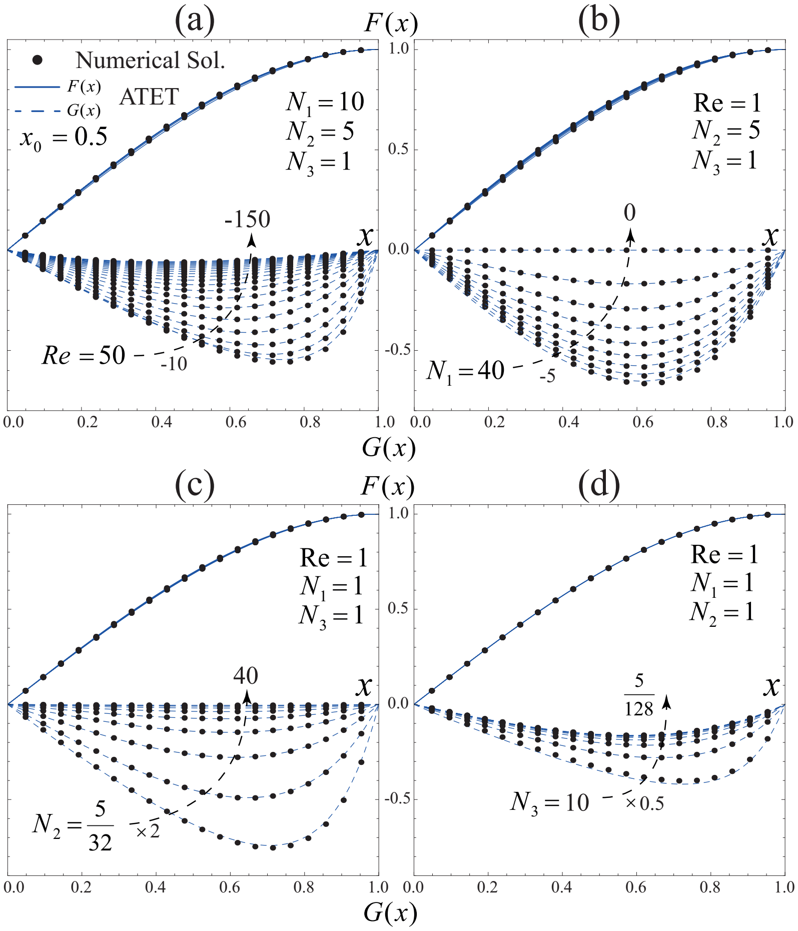

Figure 2.5: Comparison of the numerical and ATET solutions ($M_1 = 4$, $M_2 = 10$, and $x_0 = 0.5$) for $F(x)$ and $G(x)$ with respect to (a) Re, (b) N_1, (c) N_2, and (d) N_3 for eqs. (2.12).

2.4.2 Application 2: Heat Transfer

The thermal characteristics of a single uniformly thick rectangular fin with a power law type heat transfer coefficient and with/without heat transfer at the tip of the fin was studied in Ref. [67], in which the governing equation was addressed as

$$\theta''(x) - \epsilon^2 \theta^k(x) = 0, \tag{2.15}$$

where the prime stands for differentiation with respect to the nondimensional fin length x, the exponent $k \in [-3, 6] \subset \mathbb{R}$, and ϵ^2 is denoted as the fin parameter. The boundary equations for an insulated fin tip are

$$\theta'(0) = 0, \qquad \theta(1) = 1. \tag{2.16}$$

Due to the significance of the fin applications, several researchers studied the problem and reported approximate analytical explicit solutions such as in Ref. [68] with Adomian's decomposition method; in Refs. [69, 70] with perturbation, homotopy perturbation and homotopy analysis methods; and in Ref. [71] with modified variational iteration method. With redefining the boundary conditions, Ref. [57] reported implicit HAM and HPM solutions, which improved the solutions of [69, 70]. Recently, with the aid of computer algebra software the exact, but still implicit, solutions based on special functions were obtained in Ref. [72] for several domains of k values. However, to facilitate engineering studies, we would like to obtain parametric ATET solutions, which are in terms of more elementary functions.

The start point $x_0 = 0.5$ leads to more accurate solutions for this application as well, but we take $x_0 = 0$, for which the resulting solutions are relatively simpler and of sufficient accuracy. Employing eq. (2.4), we write the sixth order parametric ATET solution for $\theta(x)$ for arbitrary values of k as

$$\theta(x) = c_0 + \frac{1}{2!}c_0^k(\epsilon x)^2 + \frac{k}{4!}c_0^{2k-1}(\epsilon x)^4 + \frac{k(4k-3)}{6!}c_0^{3k-2}(\epsilon x)^6, \tag{2.17}$$

where the constant $c_0 = \theta(0)$ is the only unknown, which is identified from the boundary constraint $\theta(1) = 1$, namely,

$$c_0 + \frac{\epsilon^2}{2!}c_0^k + \frac{k\epsilon^4}{4!}c_0^{2k-1} + \frac{k(4k-3)\epsilon^6}{6!}c_0^{3k-2} - 1 = 0. \tag{2.18}$$

As a consequence, obtaining the fin tip point temperature has reduced to the solution of the foregoing equation, which may be readily done by various numerical approaches. However, one may convert eq. (2.18) to a polynomial by taking $c_0^{k_d}$ as a new variable, where k_d is the denominator of the irreducible rationalized k. This allows to obtain the entire solution set easily. Negative and imaginary solutions must be discarded, but care must be taken in picking the right one among the remaining real solutions. The simple criterion $0 < \theta(0) \leq 1$ suffices.

It is worth illuminating that the compact parametric solution (2.17) is given, in particular, for arbitrary values of k, while the existing solutions of Refs. [57, 69–71] are limited to only positive values of k. In fact, the new parametric solution becomes even superior to the numerical techniques such as the numerical differential solver of Mathematica, which due to singularities fails to give a numerical temperature solution for negative values of k. Before proceeding to the parametric studies, exact solutions, which exist for some special values of k, are used to benchmark the ATET solution (2.17).

Special case $k = 0$

When $k = 0$, eq. (2.15) becomes a linear differential equation, whose exact solution considering the boundary conditions (2.16) is

$$\theta^{Exact}(x)\Big]_{k=0} = \overbrace{1 - \frac{\epsilon^2}{2}}^{c_0} + \frac{1}{2}(\epsilon x)^2 = \theta(x)\Big]_{k=0}, \tag{2.19}$$

which states the exactness of the parametric solution (2.17) for this special case.

Special case $k = 1$

On the other hand, the exact solution of eq. (2.15) and the boundary conditions (2.16) for $k = 1$ may be written as

$$
\begin{aligned}
\theta^{Exact}(x)\Big]_{k=1} &= \overbrace{\frac{1}{\cosh(\epsilon)}}^{c_0}\cosh(\epsilon x) = c_0\left[1+\frac{1}{2!}(\epsilon x)^2+\frac{1}{4!}(\epsilon x)^4+\frac{1}{6!}(\epsilon x)^6\right]+\mathcal{O}(x^8)\\
&= \theta(x)\Big]_{k=1}+\mathcal{O}(x^8),
\end{aligned}
$$

which is exactly the sixth order Taylor series of the exact solution for this special case. Note that for a sufficiently higher order approximation, the ATET solution converges precisely to the exact solution. Nonetheless, considering the fact that $x \in [0, 1]$ and ϵ does not take very large values, the sixth order ATET solution holds sufficient accuracy for this special case.

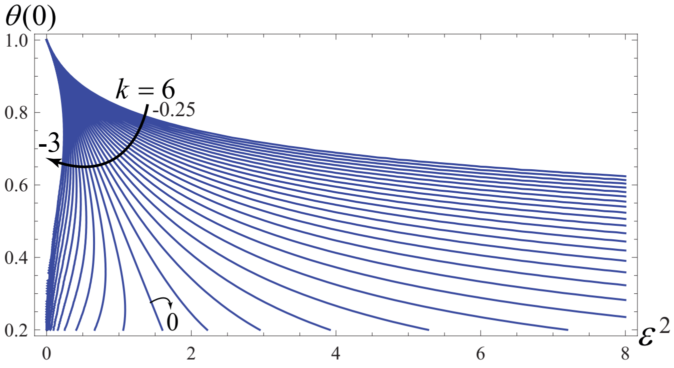

Figure 2.6: The profile of the fin tip point temperature $\theta(0)$ obtained from eq. (2.18) for the heat transfer application.

Parametric Study of the ATET Temperature Solution Profile

Figure 2.6 depicts the profile of the fin tip point temperature $\theta(0)$ obtained from the solution of eq. (2.18) with respect to k and ϵ. As the figure clarifies, the domain of ϵ diminishes as k decreases. This suggests that there may not exist a valid temperature solution $\theta(x)$ for arbitrary values of ϵ and, in particular, negative k.

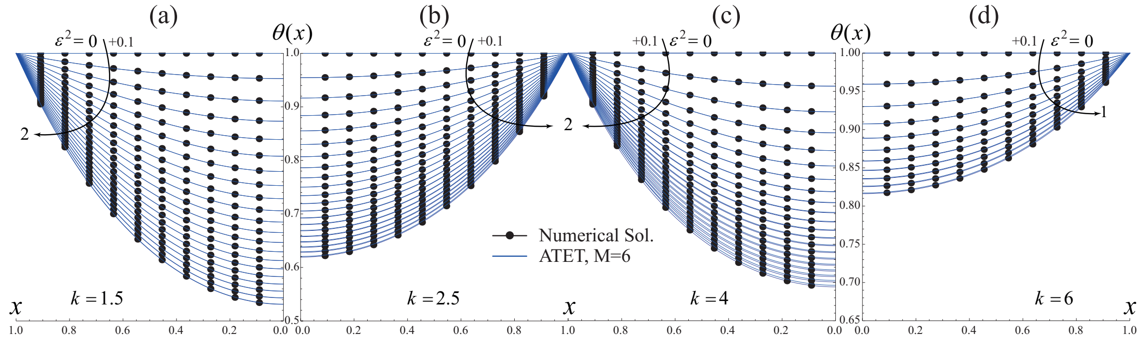

Figure 2.7: Comparison of the numerical solution and sixth order ATET solution (2.17) for the heat transfer application for (a) $k = 1.5$, (b) $k = 2.5$, (c) $k = 4$, and (d) $k = 6$.

In addition, Figure 2.7 compares the accuracy of the obtained solution with the numerical solution obtained from the numerical differential solver of Mathematica for several positive values of k. The comparison justifies the sufficiency and accuracy of the sixth order ATET solution for a variety of ϵ and positive k values for this problem. In addition, Figure 2.8 depicts the profile of the obtained sixth order ATET solution for arbitrary values of k, especially negative values, which we found Mathematica was unable to solve.

Finally, Refs. [69–71] refer to the radiative heat transfer problem when $k = 4$. Specialized from eq. (2.17), the approximate analytical solution

$$\theta(x)\Big]_{k=4} = c_0 \left[1 + \frac{1}{2!}(c_0^{3/2}\epsilon x)^2 + \frac{4}{4!}(c_0^{3/2}\epsilon x)^4 + \frac{52}{6!}(c_0^{3/2}\epsilon x)^6\right], \qquad (2.20)$$

solves the radiative heat transfer problem efficiently.

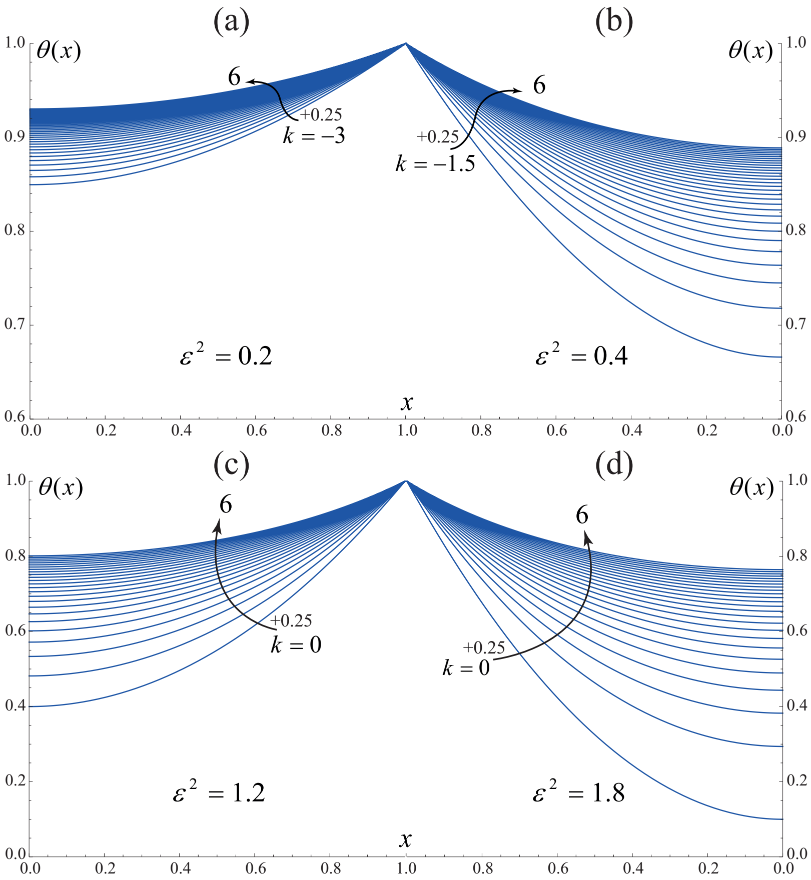

Figure 2.8: The temperature profile obtained from the ATET solution (2.17) for arbitrary k for the heat transfer application for (a) $\epsilon^2 = 0.2$, (b) $\epsilon^2 = 0.4$, (c) $\epsilon^2 = 1.2$, and (d) $\epsilon^2 = 1.8$.

2.4.3 Application 3: Theoretical Biology

Studied in Ref. [73], oxygen diffusion in a spherical cell with Michaelis–Menten oxygen uptake kinetics leads to the singular boundary value problem

$$y''(x) + \frac{2}{x}y'(x) - n\frac{y(x)}{k + y(x)} = 0, \tag{2.21}$$

where n and k are constants, and the boundary conditions are

$$y'(0) = 0, \qquad 5y(1) + y'(1) = 5. \tag{2.22}$$

Numerical techniques are vulnerable to singularities posed by singular boundary value problems. The running BVP is singular at zero, which causes numerical difficulties. For the single case, when $n = 0.76129$ and $k = 0.03119$, Ref. [74] employed variational iteration method, and reported an approximate solution.

ATET readily avoids the singularity, if written about any nonzero point. Taking $x_0 = 0.5$, the explicit second order ATET solution, for any combination of n and k, is

$$y(x) = c_0 + c_1(x^2 - 1/4), \tag{2.23}$$

where the constants $c_0 = y(0.5)$ and $c_1 = y'(0.5)$ are

$$\begin{aligned} c_0 =& \frac{1}{2}\left(1 - k - \frac{23}{120}n \pm \sqrt{(1+k)^2 - \frac{23}{120}n(2 - 2k - \frac{23}{120}n)}\right), \\ c_1 =& \frac{nc_0}{6(k + c_0)}. \end{aligned} \tag{2.24}$$

Note that only one of the plus and minus signs leads to the favorable solution, and the other one would lead to extraneous solution. Figure 2.9(a) depicts the explicit second order ATET solution for various moderate values of n and k. For larger values, we calculated fourth order ATET solutions, which are illustrated in Figure 2.9(b). Note that the numerical differential solver of Mathematica was unable to circumvent the singularity. Therefore, in the absence of a valid numerical solution and for validation purposes, we plugged the solutions in eq. (2.21), and monitored the residuals, which were no more than 0.005 for the second order, and 0.001 for the fourth order solutions.

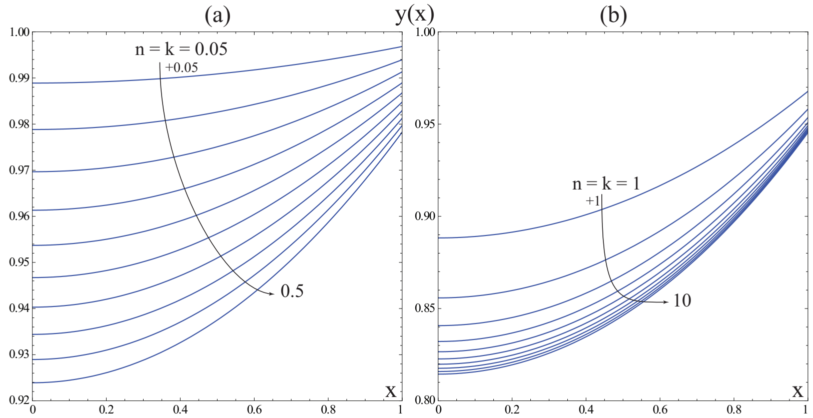

Figure 2.9: Solution profile based on (a) the second order, and (b) fourth order ATET solutions for application 3.

Special case $n = 0$

When $n = 0$, eq. (2.21) is amenable to analytical solution, whose exact solution in view of the boundary conditions is $y(x) = 1$. Likewise, ATET solutions are exact for this case. To be precise, $c_0 = 1$ and $c_1 = 0$ for the second order ATET solution, which lead to the same exact solution.

Special case $k = 0$

When $k = 0$, $y(x) = 1 + \frac{1}{30}n(5x^2 - 7)$ is the exact solution of eq. (2.21) and its boundary conditions. The ATET solution is exact for this case as well. While this may be verified algebraically for the explicit second order ATET solution, higher order solutions may be verified only numerically.

2.5 Summary and Conclusions

It was shown that ATET solutions of boundary value problems become highly accurate when written about the center of the problem domain. This enables us to effectively solve singular boundary value problems, which pose computational difficulties for numerical techniques. In addition, for a system of equations, ATET allows to control the accuracy of each solution independently of that of the other solution components. Three BVPs arising in major engineering and scientific applications, such as micropolar fluids, heat transfer, and theoretical biology were studied. For each application, approximate analytical ATET solutions were obtained and justified by numerical solutions. For the singular BVPs of biology and heat transfer, the obtained parametric solutions, surprisingly, provided accurate solution profiles, while the differential solver of Mathematica, due to singularities, failed to return numerical solutions. For the micropolar fluids application, it was shown that the accuracy of each stream function solution can be safely and desirably controlled without disturbing the accuracy of the remaining solution. Besides the accuracy, the obtained parametric solutions for the studied applications appeared to be very simple and manageable for parametric studies. These are attributed to the automatically recognition of the form of the solution by ATET as it takes advantage of the exact higher order derivatives obtained form the successive differentiation of the target differential equation. While maintaining the accuracy, this drastically reduces the size of the obtained solution. It is envisioned that studying and exploring the pattern of the ATET solutions may be a good starting point for obtaining exact closed form solutions for yet unsolved nonlinear engineering phenomena.

Chapter 3

Parametric Large Deflection Solutions for Euler–Bernoulli Cantilever Beams

The goal of this chapter is to present approximate analytical solutions to the large deflection problem of elastic and uniform Euler–Bernoulli cantilever beams under combined tip point loading. Utilizing the Automatic Taylor Expansion technique, discussed in Chapter 2, parametric angular, horizontal, and vertical deflection components are obtained in terms of the tip point loading parameters. The obtained parametric solutions are easy to manipulate and implement for engineering analyses and designs. Contents of this chapter are documented in Ref. [15].

The rest of this chapter is organized as follows. Section 3.1 gives a review of the Euler–Bernoulli beams and their mathematical modeling. Section 3.2 reformats the modeling equations and gives the ATET solutions with relevant discussions. Section 3.3 introduces the characteristic equation of the beam's deflection. Section 3.4 recognizes several load categories, and for each category, the beam's deflection behavior is studied with the aid of the obtained ATET deflection solutions. Finally, summary and conclusions are given.

3.1 A Brief Review on Euler–Bernoulli Beams

A schematic view of a cantilever beam subjected to a tip point moment M_1 and force f with the inclination ϕ is depicted in Figure 3.1, in which E and I are the Young's modulus and the moment of inertia of the beam's cross section; s and θ are the arc length and the angular deflection of the beam; and x and y are the horizontal and vertical coordinates of the deflected beam, respectively.

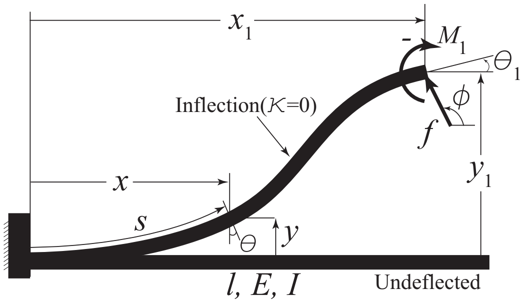

Figure 3.1: A schematic view of a tip point loaded cantilever beam.

Of common beam types is an Euler–Bernoulli beam, whose large deflection (assuming that the cross section has a large aspect ratio) is governed by

$$\kappa(x) = \frac{d^2y/dx^2}{[1+(dy/dx)^2]^{3/2}} = \frac{M}{EI} = \frac{M_1 + f\sin(\phi)(x_1 - x) - f\cos(\phi)(y_1 - y)}{EI}, \quad (3.1)$$

where κ is the curvature, and M is the axial bending moment. The boundary conditions for the cantilever beam are

$$y(0) = 0, \quad \frac{dy}{dx}(0) = 0. \quad (3.2)$$

The behavior of the Euler–Bernoulli beam depends on the choice of the material (E), the geometry of the cross section (I), and even the location of the applied load (M). For obvious reasons, it is a common practice to nondimensionalize the parameters as $s/l \to s$, $x/l \to x$, and $y/l \to y$; and finally parameterize the problem with respect to the beam's arc length. For the case of a beam with constant cross sectional properties, i.e., constant E and I, the resulting equations are

$$\frac{d^2\theta(s)}{ds^2} = \alpha^2 \sin(\theta(s) - \phi), \tag{3.3}$$

$$\theta(0) = 0, \quad \frac{d\theta(1)}{ds} = \beta, \tag{3.4}$$

$$\frac{dx(s)}{ds} = \cos(\theta(s)), \quad x(0) = 0, \tag{3.5}$$

$$\frac{dy(s)}{ds} = \sin(\theta(s)), \quad y(0) = 0, \tag{3.6}$$

where $\alpha^2 = \frac{fl^2}{EI}$ and $\beta = \frac{M_1 l}{EI}$. It is well known that the exact solutions to this weakly decoupled boundary value problem can be written in terms of the implicit elliptic integral solutions as

$$s = \pm \int_0^{\theta(s)} \frac{d\theta}{\sqrt{\beta^2 + 2\alpha^2(\cos(\theta_1 - \phi) - \cos(\theta - \phi))}}, \tag{3.7}$$

$$x = \pm \int_0^{\theta(s)} \frac{\cos(\theta) d\theta}{\sqrt{\beta^2 + 2\alpha^2(\cos(\theta_1 - \phi) - \cos(\theta - \phi))}}, \tag{3.8}$$

$$y = \pm \int_0^{\theta(s)} \frac{\sin(\theta) d\theta}{\sqrt{\beta^2 + 2\alpha^2(\cos(\theta_1 - \phi) - \cos(\theta - \phi))}}, \tag{3.9}$$

where the plus and minus signs in the foregoing deflection components are inherent to the beam's multiple behavior, and often in the literature are denoted as elbow up and elbow down solutions. The implicit elliptic integral solutions pose some challenges. First, they depend on the unknown θ_1, which complicates the integration procedure, even when solved numerically. Second, depending on input loading parameters, the solutions may be very close to singularities, which drastically complicate the numerical integration. Recall that the deflection solutions change sign as the input loading creates inflection points, where the curvature changes sign, such as the one schematically shown in Figure 3.1. The more the number of inflection points, the more the number of solution branches. However, in the next section, we present beam's parametric deflection components, which are sign independent.

3.2 Parametric Large Deflection Solutions

To efficiently solve for the beam's deflection components, we first define $\psi(s) \triangleq \theta(s) - \phi$ and rewrite eqs. (3.3)-(3.6) as

$$\frac{d^2\psi(s)}{ds^2} = \alpha^2 \sin(\psi(s)), \tag{3.10}$$

$$\psi(0) = -\phi, \quad \frac{d\psi(1)}{ds} = \beta, \tag{3.11}$$

$$\frac{dx(s)}{ds} = \cos(\psi(s) + \phi), \quad x(0) = 0, \tag{3.12}$$

$$\frac{dy(s)}{ds} = \sin(\psi(s) + \phi), \quad y(0) = 0. \tag{3.13}$$

Employing the ATET, we write the solution of the foregoing differential equations as

$$\psi(s) = c_0 + c_1(s - s_0) + \lim_{\mathcal{M}_1 \to \infty} \sum_{i=2}^{\mathcal{M}_1} \frac{1}{i!} \frac{d^i\psi(s_0)}{ds^i}(s - s_0)^i, \tag{3.14}$$

$$x(s) = x_{\mathcal{M}_2}(s_0) + \lim_{\mathcal{M}_2 \to \infty} \sum_{i=1}^{\mathcal{M}_2} \frac{1}{i!} \frac{d^i x(s_0)}{ds^i}(s - s_0)^i, \tag{3.15}$$

$$y(s) = y_{\mathcal{M}_3}(s_0) + \lim_{\mathcal{M}_3 \to \infty} \sum_{i=1}^{\mathcal{M}_3} \frac{1}{i!} \frac{d^i y(s_0)}{ds^i}(s - s_0)^i, \tag{3.16}$$

where $s_0 \in [0, 1]$, $c_0 = \psi(s_0)$, $c_1 = \frac{d\psi(s_0)}{ds}$,

$$\begin{aligned} x_{\mathcal{M}_2}(s_0) &= \lim_{\mathcal{M}_2\to\infty}\sum_{i=1}^{\mathcal{M}_2}\frac{(-1)^{i+1}}{i!}\frac{d^i x(s_0)}{ds^i}s_0^i, \\ y_{\mathcal{M}_3}(s_0) &= \lim_{\mathcal{M}_3\to\infty}\sum_{i=1}^{\mathcal{M}_3}\frac{(-1)^{i+1}}{i!}\frac{d^i y(s_0)}{ds^i}s_0^i, \end{aligned}$$

and $\mathcal{M}_1$-$\mathcal{M}_3$ are, respectively, the orders of the ATET solutions for $\psi(s)$, (thus, for $\theta(s)$), $x(s)$ and $y(s)$. Furthermore, due to ATET, the higher order derivatives $\frac{d^i\psi(s_0)}{ds^i}$ for $i \geq 2$ and the higher order horizontal and vertical derivatives $\frac{d^i x(s_0)}{ds^i}$ and $\frac{d^i y(s_0)}{ds^i}$ for $i \geq 1$ are calculated by successively differentiating eqs. (3.10), (3.12), and (3.13), respectively. As a result, all of the higher order derivatives, which fully determine the beam's deflection components $\theta(s)$, $x(s)$, and $y(s)$, are at hand except c_0 and c_1, which would be identified by imposing the boundary conditions (3.11).

For example, with taking $\mathcal{M}_1 = \mathcal{M}_2 = \mathcal{M}_3 = 5$, the fifth order ATET solutions for $\theta(s)$, $x(s)$, and $y(s)$ may be written as

$$\theta(s) = \tilde{c}_0+c_1(s-s_0)+\frac{\alpha_s}{2!}(s-s_0)^2+\frac{c_1\alpha_c}{3!}(s-s_0)^3+\frac{\alpha_s\eta_1}{4!}(s-s_0)^4+\frac{c_1\left(\alpha_c\eta_2-3\alpha^4\right)}{5!}(s-s_0)^5, \tag{3.17}$$

$$\begin{aligned} x(s) = x_5(s_0) &+ \cos(\tilde{c}_0)(s-s_0) - \frac{c_1\sin(\tilde{c}_0)}{2!}(s-s_0)^2 - \frac{c_1^2\cos(\tilde{c}_0)+\alpha_s\sin(\tilde{c}_0)}{3!}(s-s_0)^3 \\ &- \frac{c_1\left(3\alpha_s\cos(\tilde{c}_0)+\eta_1\sin(\tilde{c}_0)\right)}{4!}(s-s_0)^4 - \frac{\alpha_s\eta_3\sin(\tilde{c}_0)+\eta_4\cos(\tilde{c}_0)}{5!}(s-s_0)^5, \end{aligned} \tag{3.18}$$

and

$$y(s) = y_5(s_0) + \sin(\tilde{c}_0)(s-s_0) + \frac{c_1\cos(\tilde{c}_0)}{2!}(s-s_0)^2 - \frac{c_1^2\sin(\tilde{c}_0) - \alpha_s\cos(\tilde{c}_0)}{3!}(s-s_0)^3 \\ - \frac{c_1\left(3\alpha_s\sin(\tilde{c}_0) - \eta_1\cos(\tilde{c}_0)\right)}{4!}(s-s_0)^4 + \frac{\alpha_s\eta_3\cos(\tilde{c}_0) - \eta_4\sin(\tilde{c}_0)}{5!}(s-s_0)^5, \tag{3.19}$$

where $\tilde{c}_0 = c_0 + \phi$, $\alpha_s = \alpha^2\sin(c_0)$, $\alpha_c = \alpha^2\cos(c_0)$, $\eta_1 = \alpha_c - c_1^2$, $\eta_2 = 4\alpha_c - c_1^2$, $\eta_3 = \alpha_c - 7c_1^2$, $\eta_4 = c_1^2\eta_2 + 3\alpha_s^2$, and finally

$$\begin{aligned} x_5(s_0) &= \cos(\tilde{c}_0)s_0 + \frac{c_1\sin(\tilde{c}_0)}{2!}s_0^2 - \frac{c_1^2\cos(\tilde{c}_0) + \alpha_s\sin(\tilde{c}_0)}{3!}s_0^3 \\ &\quad + \frac{c_1\left(3\alpha_s\cos(\tilde{c}_0) + \eta_1\sin(\tilde{c}_0)\right)}{4!}s_0^4 - \frac{\alpha_s\eta_3\sin(\tilde{c}_0) + \eta_4\cos(\tilde{c}_0)}{5!}s_0^5, \\ y_5(s_0) &= \sin(\tilde{c}_0)s_0 - \frac{c_1\cos(\tilde{c}_0)}{2!}s_0^2 - \frac{c_1^2\sin(\tilde{c}_0) - \alpha_s\cos(\tilde{c}_0)}{3!}s_0^3 \\ &\quad + \frac{c_1\left(3\alpha_s\sin(\tilde{c}_0) - \eta_1\cos(\tilde{c}_0)\right)}{4!}s_0^4 + \frac{\alpha_s\eta_3\cos(\tilde{c}_0) - \eta_4\sin(\tilde{c}_0)}{5!}s_0^5. \end{aligned}$$

3.2.1 Choice of the Start Point s_0

In general, the obtained ATET solutions (3.14)-(3.16) depend explicitly on the value of s_0, which may take finitely many values. Choice of s_0 has three major impacts, such as on the efficiency and simplicity of the solution procedure, on the accuracy and on the convergence of the solutions.

It was already shown that the obtained ATET solutions contain two unknown constants c_0 and c_1. However, if s_0 is taken as either extreme points of the beam (i.e., 0 or 1), the ATET solutions do become simpler as either c_0 or c_1 becomes a known parameter. This drastically simplifies the solution procedure.

To clarify the effect of s_0 on the solution accuracy, Figure 3.2 illustrates and compares the deflection components of the entire nondimensional beam length for several loading parameters obtained from the numerical differential solver of Mathematica and the obtained fifth order ATET solutions (3.17)-(3.19) with $s_0 = 0$, $s_0 = 0.5$, and $s_0 = 1$. Note that, for the sake of symmetry, we considered counter clock-wise forces, thus, restricted the force angle ϕ to stay within the first and second quadrants.

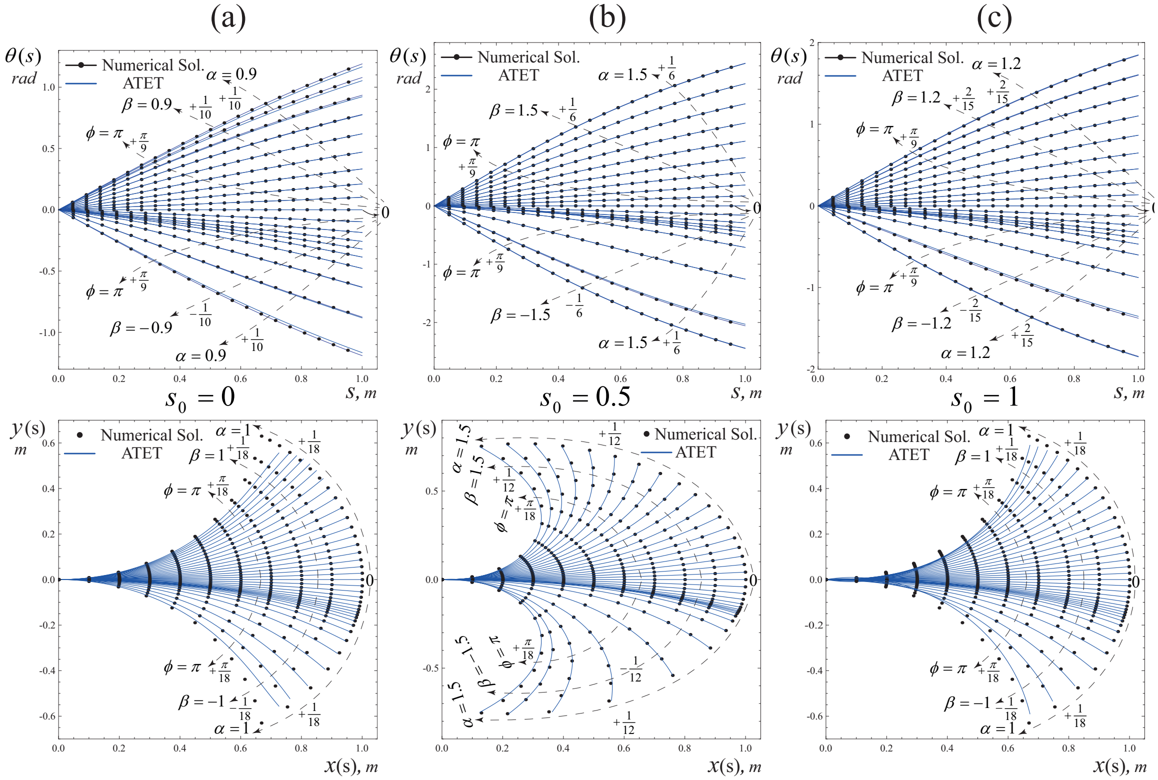

Figure 3.2: Comparison of the numerical solution and the fifth order ATET solutions (3.17)-(3.19) with (a) $s_0 = 0$, (b) $s_0 = 0.5$, and (c) $s_0 = 1$ for the deflection components of the entire nondimensional beam length for several loading parameters.

Subfigures 3.2(a) clearly reveal more accurate solutions in the vicinity of the clamped point, while Subfigures 3.2(c) do the same for the tip point. These are expected, since the ATET solutions exploit the Taylor series expansion written about the clamped and the tip points, respectively. Moreover, referring to the same subfigures, the solutions associated with $s_0 = 0$ accommodate relatively an smaller domain of input loading parameters compared to that of $s_0 = 1$. To be precise, the solutions of the former are valid for $\alpha = |\beta| \leq 0.9$, while those of the latter are valid for $\alpha = |\beta| \leq 1.2$. This is also expected, since the points in the vicinity of the clamped point undergo considerably smaller deflections than those of the tip point. Hence, the obtained solutions associated with $s_0 = 0$ predict relatively small deformations, which indispensably may not be able to capture the larger deformations existing in the vicinity of the tip point.

On the other hand, while Subfigures 3.2(a) and (c) depict reasonably accurate solutions, Subfigures 3.2(b) show that ATET solutions written about the middle of the beam's axis are even more accurate and a larger parameter domain, $\alpha = |\beta| \leq 1.5$, is captured. Again, this may be explained by noting that among all of the points on the beam's axis the point $s_0 = 0.5$ attains the least distance from both extreme points, i.e., the clamped and the tip points. This, in turn, requires the least extrapolation, therefore, the least error.

Finally, solution convergence becomes crucial, once more accurate solutions, thus, higher order ATET solutions are to be sought. Neither $s_0 = 0$ nor $s_0 = 1$ gives rise to convergent solutions. However, with $s_0 = 0.5$ the entire points on the beam's axis are within $|s - s_0| < 1$ which increases the chance of the convergence. Therefore, we choose this point, otherwise mentioned, for the numerical studies given later.

3.2.2 Choice of the Approximation Orders $\mathcal{M}_1$-$\mathcal{M}_3$

For a convergent solution, it is clear that the more the approximation orders $\mathcal{M}_1$-$\mathcal{M}_3$ in eqs. (3.14)-(3.16), the better the accuracy of the approximate ATET solutions; as $\mathcal{M}_1$-$\mathcal{M}_3$ tend to infinity the resulting series solutions converge to the exact solutions. However, a blind increase of the approximation orders is not practical.

Although there are some loading conditions, to be studied later, which do not necessarily require approximation orders increase for larger input loading parameter domains, it is reasonable, in general, to consider a correspondence between the approximation orders and the magnitude of the input loading parameters. Referring to Subfigures 3.2(b), we have already seen that even the fifth order ATET solutions capture a significant domain of the loading parameters, $\alpha^2 \leq 1.5^2 = 2.25$, $|\beta| \leq 1.5$, and $|\phi| < \infty$. In addition, for the very large parameter domains studied later, the approximation orders that we chose never exceeded 30.

Another important point about the approximation orders $\mathcal{M}_1$-$\mathcal{M}_3$ is their independence. Referring to eqs. (3.14)-(3.16), it may be seen that $\theta(s)$, $x(s)$, and $y(s)$ may be obtained independently of one another by simply choosing the approximation orders $\mathcal{M}_1$-$\mathcal{M}_3$ independently. This feature of the ATET solutions enables us to exclusively adjust the accuracy of any of the desired deflection components. For example, considering the fact that the vertical displacements resulted from small acute loading angles dominate the horizontal displacements, $\mathcal{M}_2$ may not be chosen as large as $\mathcal{M}_3$. Utilizing this feature in Section 3.4, we employ relatively lower approximation orders for the angular deflections of the beam, while higher orders for the horizontal and vertical displacements.

3.3 Beam's Characteristic Equation

Several parameters are involved in the beam's deflection. To be precise, the input loading parameters α, β, and ϕ result in three deflection components $\theta(s)$, $x(s)$, and $y(s)$ which would possibly determine the beam's unique deflected configuration. But, three independent equations are required to identify the three deflection components. However, it turns out that, sort of similar to the resultant equation of a system of polynomials in the algebraic elimination theory, there is a unique equation, which governs all of the input and output parameters. To this end, we multiply $x(s)$ and

$y(s)$, given by eqs. (3.8) and (3.9), respectively, by $\sin(\phi)$ and $\cos(\phi)$, and subtract the results, which we integrate and write as

$$\sin(\phi)x(s) - \cos(\phi)y(s) = \begin{cases} \frac{1}{\beta}(\cos(\theta - \phi) - \cos(\phi)) & \text{if } \alpha = 0 \\ \frac{\pm 1}{\alpha^2}\left(\sqrt{C - 2\alpha^2\cos(\phi)} - \sqrt{C - 2\alpha^2\cos(\theta - \phi)}\right) & \text{otherwise} \end{cases},$$

where $C = \beta^2 + 2\alpha^2\cos(\theta_0 - \phi)$. The foregoing resultant equation, which we call the beam's deflection characteristic equation, intertwines the deflection components and the loading parameters which may geometrically be thought of as a multi-dimensional surface in terms of the loading parameters and the resulting deflections. Elaborate assessment of this surface, such as the identification of its contours, solely due to its multi-dimensionality seems almost impossible. However, for a pure end-moment, this surface attains a circular $x - y$ contour, discussed below, which may be exploited as a theoretical tool to validate the accuracy of the obtained ATET solutions for this special loading condition.

3.3.1 A Circular Deflection

In the absence of the end-force (i.e., $\alpha = 0$), eqs. (3.7)-(3.9) are easily integrable as

$$\theta^{Exact}(s)\Big|_{\alpha=0} = \beta s, \tag{3.20}$$

$$x^{Exact}(s)\Big|_{\alpha=0} = \frac{1}{\beta}\sin(\beta s), \tag{3.21}$$

$$y^{Exact}(s)\Big|_{\alpha=0} = \frac{1}{\beta}(1 - \cos(\beta s)). \tag{3.22}$$

These special exact solutions may be used to validate the ATET solutions. For the sake of simplicity, we verify the fifth order ATET solutions as

$$\theta(s)\Big\rfloor_{\alpha=0} = \overbrace{\tilde{c}_0 - c_1 s_0}^{0} + \overbrace{c_1}^{\beta} s = \beta s, \tag{3.23}$$

$$\begin{aligned} x(s)\Big\rfloor_{\alpha=0} &= x_5(s_0)\Big\rfloor_{\alpha=0} + \frac{\cos(\tilde{c}_0)}{c_1}\left[c_1(s-s_0) - \frac{c_1^3}{3!}(s-s_0)^3 + \frac{c_1^5}{5!}(s-s_0)^5\right] \\ &+ \frac{\sin(\tilde{c}_0)}{c_1}\left[-\frac{c_1^2}{2!}(s-s_0)^2 + \frac{c_1^4}{4!}(s-s_0)^4\right] \approx \frac{1}{\beta}\sin(\beta s) + \mathcal{O}(s^6), \end{aligned} \tag{3.24}$$

and

$$\begin{aligned} y(s)\Big\rfloor_{\alpha=0} &= y_5(s_0)\Big\rfloor_{\alpha=0} + \frac{\sin(\tilde{c}_0)}{c_1}\left[c_1(s-s_0) - \frac{c_1^3}{3!}(s-s_0)^3 + \frac{c_1^5}{5!}(s-s_0)^5\right] \\ &+ \frac{\cos(\tilde{c}_0)}{c_1}\left[\frac{c_1^2}{2!}(s-s_0)^2 - \frac{c_1^4}{4!}(s-s_0)^4\right] \approx \frac{1}{\beta}(1-\cos(\beta s)) + \mathcal{O}(s^6). \end{aligned} \tag{3.25}$$

As evidenced above, for the pure end-moment loading, the fifth order ATET solutions become exact for the angular deflections and the fifth order Taylor series expansion of the available exact solutions for the horizontal and the vertical displacements. Clearly, exact ATET solutions for the axial displacements would be obtained if sufficiently higher order approximations were employed.

Figure 3.3 illustrates the beam deflection profile for several values of β. As seen, beam deflects as a circular segment, whose governing equation may be obtained by eliminating s from the parametric $x(s)$ and $y(s)$, given by eqs. (3.21) and (3.22), as

$$x^2 + (y - \frac{1}{\beta})^2 = \frac{1}{\beta^2}. \tag{3.26}$$

It should be emphasized that $x(s)$ and $y(s)$ are both periodic with the frequency $\nu = \frac{\beta}{2\pi}$. Therefore, a nondimensional pure end-moment β makes the beam deflect like a coil of ν rings. For simplicity we call ν as the beam's circularity. Figure 3.4 depicts a deflected beam of five rings, which for illustrative purposes are shown with

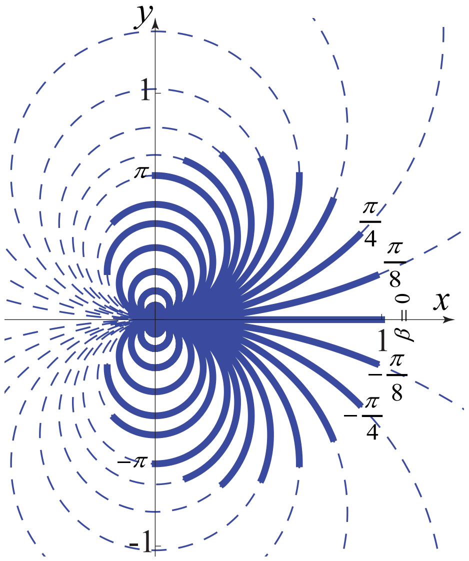

Figure 3.3: Exact large deflection profile of a cantilever beam of unit length subject to nondimensional pure end-moments.

offsets. Note, however, that with this representation, we assumed that the beam's cross section does not geometrically interfere with the deflection governed primarily by eq. (3.1).

3.4 Parametric Study of the Beam's Deflection

We already discussed the pure end-moment loading condition and in the following we consider other loading conditions, such as pure end-force, dominant end-force and -moment, and mixed loading with inflection point for which no exact explicit solutions exist in the literature. The study is twofold.

On the one hand, we discuss how the input loading parameters affect the beam's deflection for each loading case. Whenever significant, we highlight the similarities and the differences between the loading categories.

On the other hand, compared with the numerical solutions obtained from the numerical differential solver of Mathematica, we also show the applicability and the

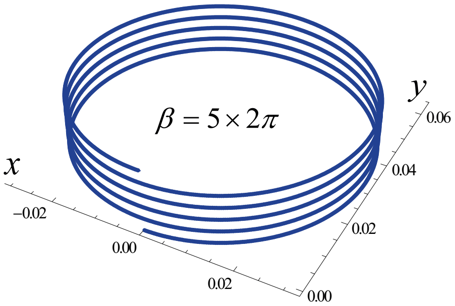

Figure 3.4: A deflected cantilever beam of unit length and circularity 5 subject to a pure end-moment.

accuracy of ATET for the categorized loading conditions. Note that, in doing so, we assume that the beam is of unit length and take the initial point of the ATET solutions, otherwise stated, as $s_0 = 0.5$, which was shown to be an effective choice. In addition, we mostly consider very large loading conditions in order to show the power of ATET and as well as giving to the readers an insight to choosing the sufficient ATET approximation orders.

Amongst the foregoing two considerations, we discuss the former explicitly, and, for succinctness, leave the latter to the reader to judge the accuracy of the method from the comparison graphs.

3.4.1 Pure End-Force

In contrast to the case of a pure end-moment, exact explicit deflection solutions for the case of pure end-forces are not yet known. In an effort to get a better insight to the case of a general combined loading, we study this case first with an exhaustive enumeration of the effects of the loading parameters.

Figure 3.5 shows the beam's angular deflections for applied pure end-forces. It may be seen that the angular deflections, unlike for pure end-moments, no longer monotonically increase by increasing the magnitude of the applied force. To be studied

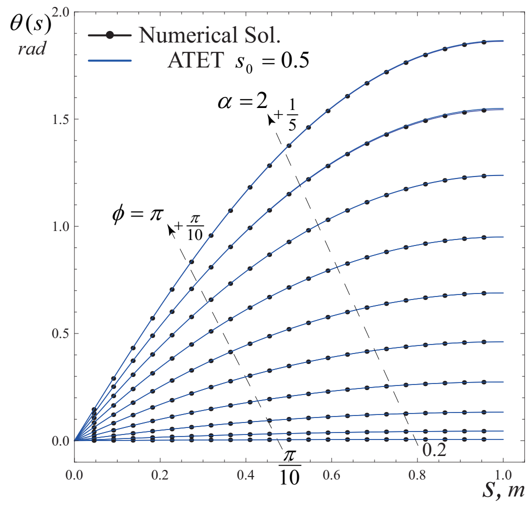

Figure 3.5: Comparison of the numerical and the sixth order ATET solutions ($\mathcal{M}_1 = 8$ for $\alpha = 2$) for the angular deflections of the entire nondimensional beam length for pure end-forces.

later, this may be considered as an indication of the existence of an upper limit, beyond which the angular deflections no longer increase.

In addition, it appears that the smaller the load angle ϕ, the more the length of the undistorted segment of the beam. To better visualize this, Figure 3.6 shows the $x - y$ deflections of the beam for the same loading conditions. As seen, beam's axis after a certain point remains straight and does not distort. This may be considered as a kinematic behavior of the beam, as the straight part of the deflected beam gets pinned and rotates about a point on the beam's axis. This kinematic behavior has led the designers, as in Refs. [11–13], to synthesize simplified pseudo-rigid-body models, which mimic the beam's endpoint trajectory for certain small loading domains.

Force Angle Effects

Figure 3.7 depicts the beam's deflection profiles for pure end-forces with three magnitudes and several angles. In agreement with the human intuition, common to all subfigures is the fact that increasing the force angle for the same force magnitude

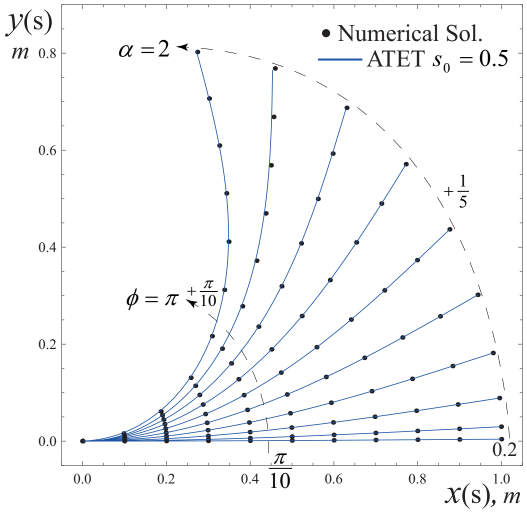

Figure 3.6: Comparison of the numerical and the sixth order ATET solutions ($\mathcal{M}_1 = \mathcal{M}_2 = \mathcal{M}_3 = 8$ for $\alpha = 2$) for the horizontal and vertical deflections of the entire nondimensional beam length for pure end-forces.

does increase the deflections, but the amount of the increase depends on the force magnitude. For example, the maximum angular deflection for $\alpha = 3$ is approximately $2.72/0.49 \approx 5.55$ and $2.72/0.055 \approx 49.45$ times those of $\alpha = 1$ and $\alpha = 1/3$, respectively.

As a consequence, these observations may be considered as hints to how to consider ATET approximation orders, i.e., the more the force angle or the magnitude, the more the approximation order.

In addition, one subtle point may be seen from the same figure is the case once the force is small and pure compressive, i.e., $\phi = \pi$. This special force angle was studied extensively in the existing literature. It is well known that not all pure compressive forces may make the beam deflect. As a matter of fact, only those with $\alpha > \frac{\pi}{2}$ are competent to make deflections. In agreement with this result, both the numerical method and the ATET reveal intelligent results as in Subfigures 3.7(a) and (b).

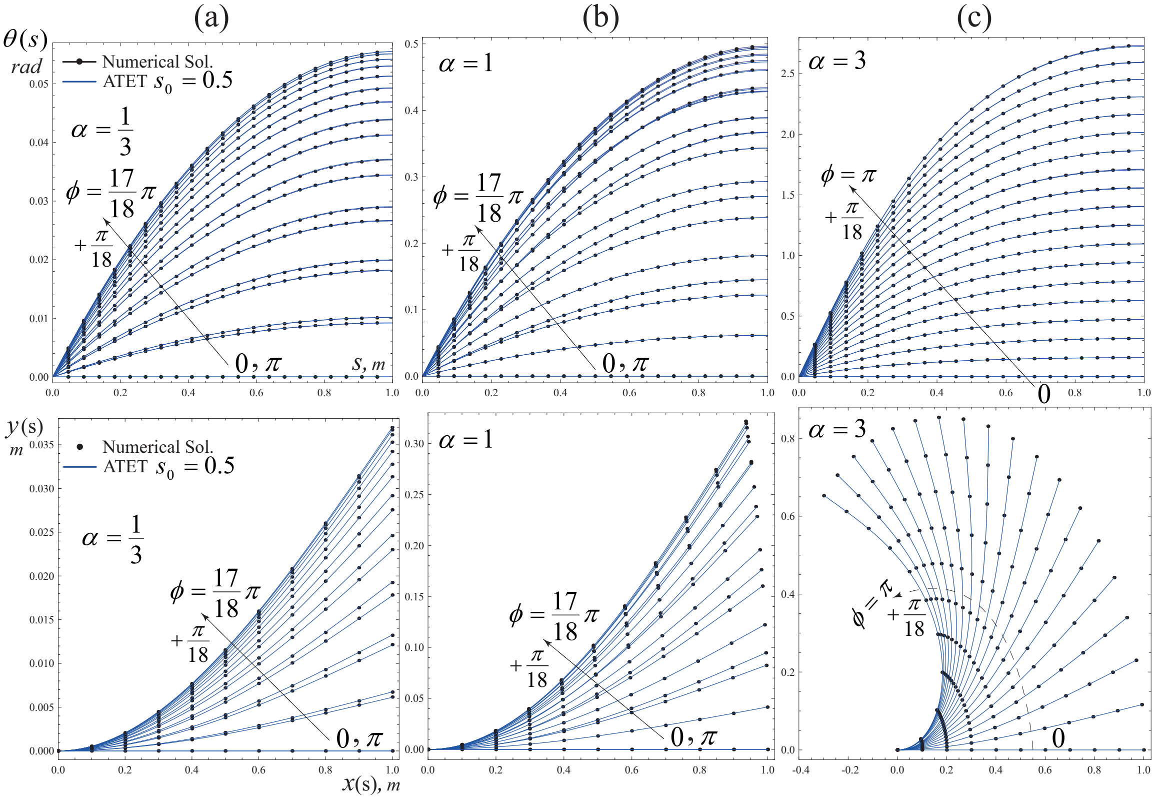

Figure 3.7: Force angle effects on the beam's deflections (a) $\alpha = \frac{1}{3}$ and $\mathcal{M}_1 = \mathcal{M}_2 = \mathcal{M}_3 = 3$, (b) $\alpha = 1$ and $\mathcal{M}_1 = \mathcal{M}_2 = \mathcal{M}_3 = 4$, and (c) $\alpha = 3$, $\mathcal{M}_1 = \mathcal{M}_2 = \mathcal{M}_3 = 8$ for $\phi < \frac{2\pi}{3}$ otherwise $\mathcal{M}_1 = 12$ and $\mathcal{M}_2 = \mathcal{M}_3 = 14$.

Beam's End-Angle Trajectory

Figure 3.8 shows the trajectory of the beam's end-angle with respect to the magnitude of the applied pure end-forces of various angles. From a comparison point of view, it is clear that for very large values of α, the obtained ATET solutions tend to be even more accurate than the numerical solutions obtained from the numerical differential solver of Mathematica. One may clearly see that the numerical solutions either do not exist for some large domains of α or oscillate, even for some cases decrease, with the increase of the magnitude of the applied load which are geometrically not plausible.

As discussed above, the beam's end-angle trajectory associated with the special

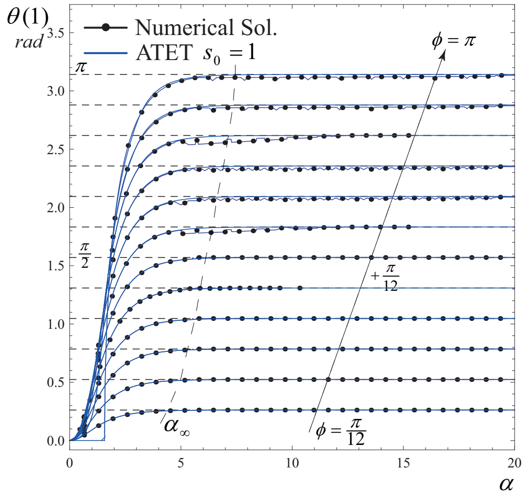

Figure 3.8: Comparison of the numerical and the tenth order ATET solutions with $s_0 = 1$ for the trajectory of the beam's end-angle for pure end-forces.

force angle $\phi = \pi$ is clearly distinct from the other trajectories as the beam's end-angle remains zero for all force magnitudes with $\alpha \in [0, \frac{\pi}{2})$.

In addition, it is clear that with the increase of the magnitude of the applied force in the domain $\alpha \in [0, \alpha_\infty)$, shown in the same figure, the beam's end-angle does increase, but outside the domain converges to the load angle ϕ and never exceeds it, no matter how large α is. This may be geometrically explained by noting that for $\alpha \geq \alpha_\infty$, the applied force becomes almost parallel to the beam's axis, hence, has no significant component normal to the beam's axis to further deflect it. This may be seen in Figure 3.9, which shows the beam's angular deflections for the entire nondimensional beam length for very large pure end-forces of three different angles. For all cases, we see that excessive increase of the force magnitude has no significant effect on the deflection amount. This, again, may be considered as another hint so as not to blindly and needlessly increase the ATET approximation orders.

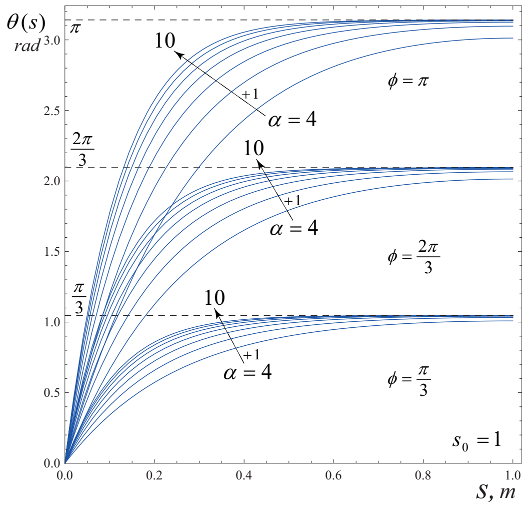

Figure 3.9: Tenth order ATET solutions with $s_0 = 1$ for the angular deflections of the entire nondimensional beam length for large pure end-forces of angles $\frac{\pi}{3}$, $\frac{2\pi}{3}$, and π.

3.4.2 Dominant End-Moment

In Subsection 3.3.1 we have seen that for an applied pure end-moment the angular deflection of the beam becomes linearly proportional to the bending moment along the beam length. We have also seen that the points on the beam axis undergo a circular displacement. With these in mind, for a combined loading condition, once the applied end-moment sufficiently dominates the end-force, it is reasonable to expect similar beam deflections.

Figure 3.10 depicts the beam's angular deflections for combined loadings with dominant end-moments. It may be seen that the angular deflections as expected are almost proportional to the applied nondimensional moments. For example, for $\beta = \pm 6$, we observe $\theta(1) \approx \pm 6$.

In addition, Figure 3.11 portrays the beam's horizontal and vertical displacements for the same loading conditions as above. Again, as expected, points on the beam's axis undergo a semi-circular or almost an elliptical deflection. This observation may

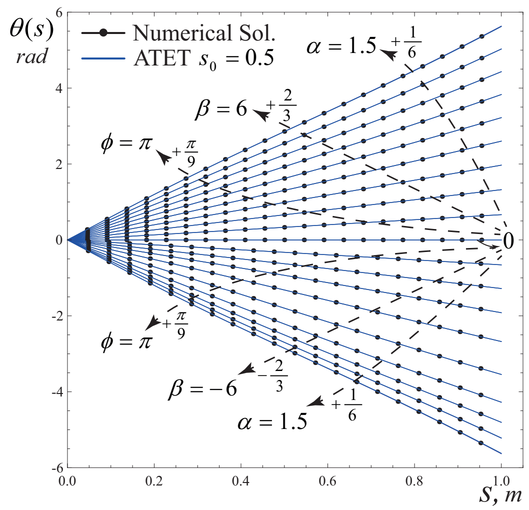

Figure 3.10: Comparison of the numerical and the tenth order ATET solutions for the angular deflections of the entire nondimensional beam length for dominant end-moments.

corroborate the appellation of the elliptic integral solutions as in eqs. (3.7)-(3.9) for the exact implicit large deflections of the Euler–Bernoulli beams.

One more point drawn from Figure 3.11 may be the observation of the beam's circularity. For example, for $\beta = \pm 6$, one may approximately observe $\nu \approx \frac{6}{2\pi} \approx 0.95$ as expected from the case of a pure end-moment.

3.4.3 Dominant End-Force

We just saw that the beam's behavior for dominant end-moments was very much like the case of pure end-moments. Similarly, it is reasonable to expect the same behavior for the case of pure and dominant end-forces. Figures 3.12 and 3.13 depict the beam's deflection for both pure and dominant end-forces with opposite small moments. Clearly, the deflections associated with the opposite moments slightly deviate from and are almost symmetrical with respect to the corresponding pure end-force deflections.

Both figures also show that with the increase of the loading parameters, especially,

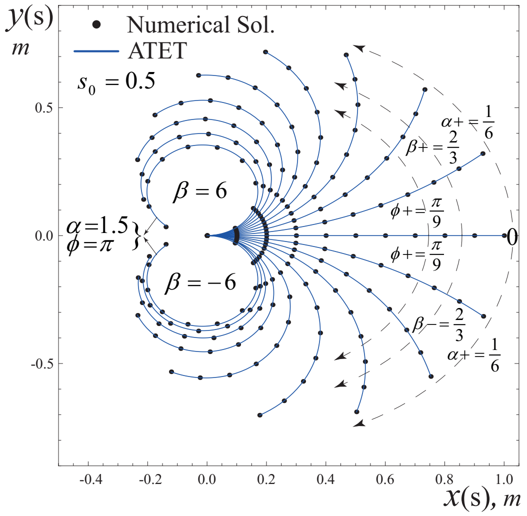

Figure 3.11: Comparison of the numerical and the tenth order ATET solutions for the horizontal and the vertical deflections of the entire nondimensional beam length for dominant end-moments.

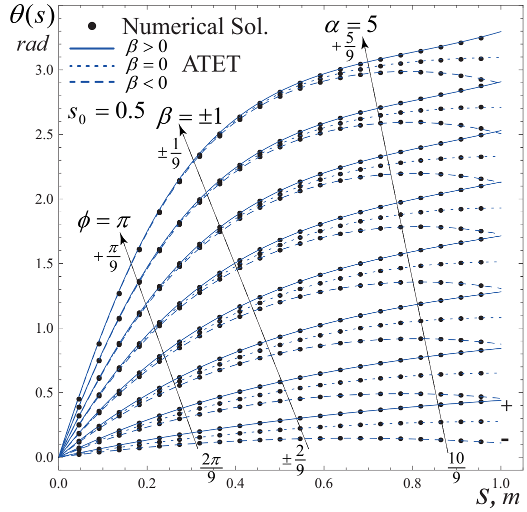

Figure 3.12: Comparison of the numerical and the tenth order ATET solutions ($\mathcal{M}_1 = 15$ for $\alpha = \frac{40}{9}$, and $\mathcal{M}_1 = 16$ for $\alpha = 5$) for the angular deflections of the entire nondimensional beam length for pure and dominant end-forces.

the load angle, the moment's effect becomes local to the beam's tip point, and has minor influence on the remaining parts of the beam.

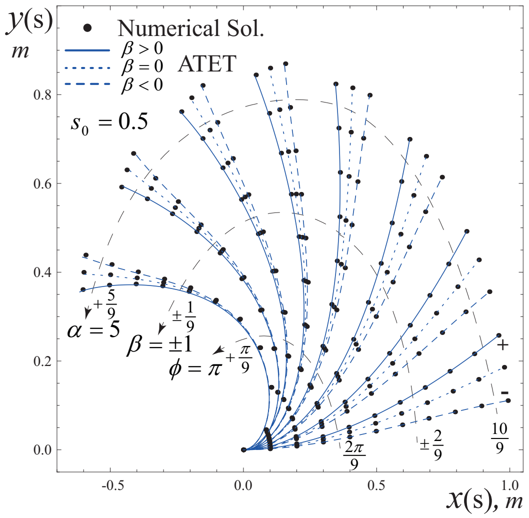

Figure 3.13: Comparison of the numerical and the tenth order ATET solutions ($\mathcal{M}_2 = \mathcal{M}_3 = 12$ for $\alpha = \frac{35}{9}$; $\mathcal{M}_1 = 15$ and $\mathcal{M}_2 = \mathcal{M}_3 = 18$ for $\alpha = \frac{40}{9}$; and $\mathcal{M}_1 = 16$ and $\mathcal{M}_2 = \mathcal{M}_3 = 24$ for $\alpha = 5$) for the horizontal and vertical deflections of the entire nondimensional beam length for pure and dominant end-forces.

3.4.4 Mixed Loading with Inflection Point

It is well known that the inflection points in differential calculus are attributed to the points of a curve at which curvature sign changes occur. From a geometrical point of view, the inflection points connect the convex ($\kappa < 0$) and the concave ($\kappa > 0$) parts of a curve where κ denotes the curvature. The occurrence of such a point has a significant impact on the beam's behavior as evidenced by eqs. (3.7)-(3.9) in that beam's axial deflection solution jumps from one elbow to another. Although a decision should be made on choosing the right sign from the elliptic integral solutions, the ATET solutions are intelligent and obviate such a choice.

Inflection points occur in beam's both angular and axial deflection curves. Figure 3.14 shows the beam's angular and axial deflections for several β values and a counter-clockwise force with $\alpha = 4$ and $\phi = \frac{\pi}{3}$. While Subfigure 3.14(a) reveals the occurrence of the angular inflections for positive moments, Subfigure 3.14(b) shows

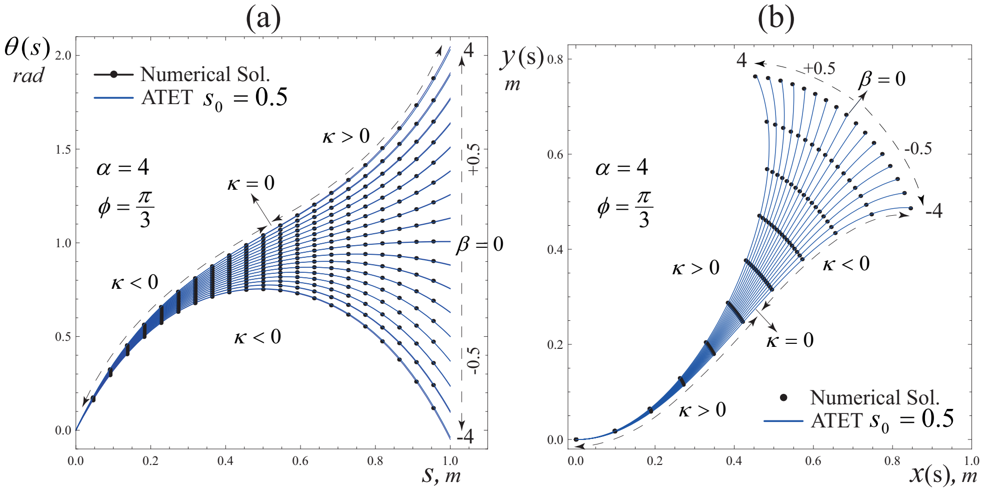

Figure 3.14: Comparison of the numerical and the eighth order ATET solutions for the beam's (a) angular and (b) axial deflections for $\alpha = 4$, $\phi = \frac{\pi}{3}$, and several values of β causing inflection points.

that the axial inflections occur only for negative moments.

From the same figure it may be inferred that the angular inflection points become regular points on the axial deflection curves. In contrast, the extrema (in the running case, the maxima) of the angular deflection curves exhibit themselves as inflection points on the axial deflection curves. This is expected, since due to eq. (3.1) the angular extrema, in other words the angular points with zero derivatives, correspond to the axial points with zero curvature values.

In the following, we study, in depth, the angular and the axial inflection points. In the discussion, without loss of generality, we assume that the applied force is counterclockwise. In addition, we consider the clamped and the tip points as the boundary points, thus, disregard them if being inflection points.

Characteristic Equations of the Angular Inflection Points

Let s_θ denote the set of the angular inflection point/points of the beam which is/are the root/roots of eq. (3.3). Considering this and the definition of the inflection point of a curve, i.e., the curvature sign change criterion, we have

$$s_\theta = \{\varsigma \mid \theta(\varsigma) = n\pi + \phi \text{ and } \sin(\theta(\varsigma - \epsilon) - \phi) \times \sin(\theta(\varsigma + \epsilon) - \phi) < 0\},$$

where ϵ is a small and positive real number and the integer n characterizes the beam's mode shape number. We summarize the existence of the angular inflection point for the different loading conditions as follows.

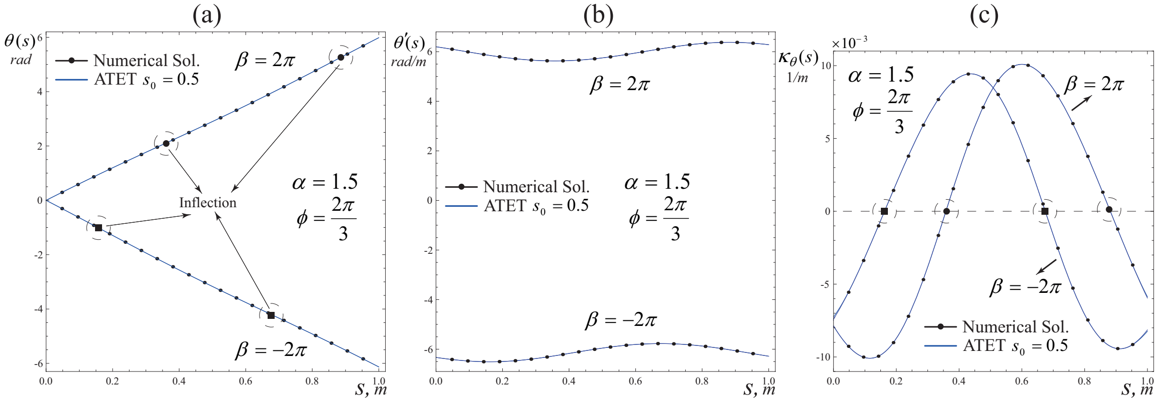

Figure 3.15: Comparison of the numerical and the 20th order ATET solutions for the beam's angular (a) deflection, (b) slope and (c) curvature for $\alpha = 1.5$, $\beta = \pm 2\pi$, and $\phi = \frac{2\pi}{3}$.

- *Pure End-Moment*: No angular inflection point may be caused by this loading since eq. (3.3) is identically zero and no curvature sign change occurs.
- *Pure End-Force*: A pure end-force loading does not cause an angular inflection point either. According to Subsubsection 3.4.1 the angular deflection never exceeds the force angle for this loading condition. Thus, with $\theta(s) \leq \phi$ no curvature sign change occurs.
- *Combined Loading*: Similar to the foregoing loading conditions, the curvature

sign change criterion comes into play. Hence, to have angular inflection points two cases are in order.

(a) $\sin(\theta(s_\theta - \epsilon) - \phi) < 0$ and $\sin(\theta(s_\theta + \epsilon) - \phi) > 0$: These may occur in two conditions.

First, once n is nonnegative and even and $\theta(s)$ is ascending, i.e., $\frac{d\theta(s)}{ds} \geq 0$. Obviously, the latter may not happen, unless the applied moment, surprisingly enough similar to the applied force, is counter-clockwise. See Subfigure 3.14(a) or the first inflection point ($\beta = 2\pi$) in Figure 3.15.

Second, once n is negative and odd and $\theta(s)$ is descending, i.e., $\frac{d\theta(s)}{ds} \leq 0$. However, the latter requires the applied moment to be dominant and clockwise. See the first inflection point ($\beta = -2\pi$) in Figure 3.15.

(b) $\sin(\theta(s_\theta - \epsilon) - \phi) > 0$ and $\sin(\theta(s_\theta + \epsilon) - \phi) < 0$: With similar reasoning, two conditions arise.

First, once n is positive and odd and $\theta(s)$ is ascending which obviously requires the applied moment to be counter-clockwise. See the second inflection point ($\beta = 2\pi$) in Figure 3.15.

Second, once n is negative and even and $\theta(s)$ is descending which necessitates the applied moment to be dominant and clockwise. See the second inflection point ($\beta = -2\pi$) in Figure 3.15.

Characteristic Equations of the Axial Inflection Points

An inflection point of the beam's axis is the root of the Euler–Bernoulli equation (3.1) which requires either the axial bending moment or the angular slope with respect to the nondimensional beam length to vanish. However, similar to the case of angular inflection points, not all such roots are inflection points, unless they experience a curvature sign change. Thus, considering this and with either integrating eq. (3.3) or differentiating eq. (3.7), the characteristic equations governing the inflection points may be written as

$$\beta^2 + 2\alpha^2(\cos(\theta_0 - \phi) - \cos(\theta(s_a) - \phi)) = 0, \tag{3.27}$$

$$\frac{d\theta(s_a - \epsilon)}{ds} \times \frac{d\theta(s_a + \epsilon)}{ds} < 0, \tag{3.28}$$

where ϵ is as before and s_a is an axial inflection point. Note that the foregoing relations are necessary and sufficient to determining whether the loading parameters α, β, and ϕ can cause an inflection point on the beam's axis. The existence of the axial inflection point for the different loading conditions is summarized as follows.

- *Pure End-Moment*: No inflection point may be caused by this loading. Referring to eq. (3.27), $\beta = 0$, which contradicts the loading condition assumption.

- *Pure End-Force*: No inflection point can occur on the beam's axis for a pure end-force loading either. This may be justified by noting that eq. (3.27) requires α to be zero which again contradicts with the loading condition assumption. Note that vanishing the expression $\cos(\theta_0 - \phi) - \cos(\theta(s_a) - \phi)$ results in $s_a = 1$, which is a boundary point and excluded by the assumption.

- *Combined Loading*: This case illuminates the significance of eq. (3.28). Due to eq. (3.27), both positive and negative moments $\pm|\beta|$ may cause inflection points, provided that $\cos(\theta_0 - \phi) - \cos(\theta(s_a) - \phi) < 0$. However, eq. (3.28) suggests that only a clockwise moment, i.e., $\beta < 0$, may cause an inflection point which is in agreement with intuition. See Subfigure 3.14(b).

3.5 Summary and Conclusions

This chapter studied the problem of determining the parametric large deflection components for the entire length of the Euler–Bernoulli cantilever beams subjected to combined tip point loading. Beam's deflection characteristic equation was introduced which is a single and unique equation governing any combination of loading and deflection parameters. Angular, horizontal, and vertical deflection solutions to the Euler–Bernoulli beam's boundary value problem were obtained in terms of the loading parameters with using the Automatic Taylor Expansion technique. The parametric solutions were then validated by comparison with the numerical solutions obtained from the numerical differential solver of Mathematica. The solutions were shown to be independently and efficiently adaptable for very large loading conditions and easily implementable for the analysis and synthesis of beam-based engineering devices. Then, a comprehensive study of the beam's angular and axial deflections behavior for several tip point loading conditions was carried out. The intelligence of the parametric solutions in recognizing the right deflection branch for both axial and the newly recognized angular inflection points was also verified. Adapting the methodology presented here for the cases of variable material and cross sectional properties is considered as a future work.

Chapter 4

Cartesian and Piecewise Parametric Large Deflection Solutions

The parametric large deflection solutions developed in the previous chapter are written about a single start point for the whole beam length. It was shown that this treatment is effective for handling arbitrary cases. However, high approximation orders are needed when the load's magnitude is large. Unfortunately, this increases the number of solutions for the unknown constants, which make up the parametric solutions. This, in turn, complicates the solution procedure, and requires careful implementation.

This chapter, first, presents cartesian large deflection solutions, which are independent of the beam's arc length. A new closed form solution for the case of a large pure end-force is also presented. Then, piecewise large deflection solutions are developed which require low approximation orders for a fast convergence. To demonstrate the robustness of these solutions, they are coded as a stand-alone user-friendly black-box solver.

4.1 Cartesian Large Deflection Solutions

Given in Chapter 3, the parametric large deflection solutions (3.8) and (3.9) are in terms of the intermediate parameter s, which is not explicitly at hand. The goal of this section is to eliminate s from the solutions, and obtain a cartesian large deflection solution, i.e., the vertical large deflection component directly in terms of the horizontal large deflection component. To this end, we employ the coordinates transformation

$$\begin{bmatrix} X \\ Y \end{bmatrix} = \frac{1}{l} \overbrace{\begin{bmatrix} \cos(\phi) & \sin(\phi) \\ -\sin(\phi) & \cos(\phi) \end{bmatrix}}^{\mathbf{R}(\phi)} \begin{bmatrix} x \\ y \end{bmatrix}, \tag{4.1}$$

where $\mathbf{R}(\phi)$ is the orthogonal rotation matrix, which rotates the components x and y clockwise by the angle ϕ about the origin. Keeping in mind that a rotation does not change the curvature, eq. (3.1) simplifies to

$$\frac{d^2Y/dX^2}{[1+(dY/dX)^2]^{3/2}} = \alpha^2 Y + \alpha_1, \tag{4.2}$$

where $\alpha_1 = \beta - \alpha^2(\cos(\phi)y_1 - \sin(\phi)x_1)/l$, α and β are as before, and the new boundary conditions become

$$Y(0) \; = \; 0, \quad \frac{dY}{dX}(0) + \tan(\phi) \; = \; 0. \tag{4.3}$$

We integrate eq. (4.2) once, and employ the second boundary condition of (4.3) to write

$$\frac{1}{\sqrt{1+(dY/dX)^2}} = |\cos(\phi)| - \alpha_1 Y - \frac{\alpha^2}{2} Y^2 \triangleq G(Y). \tag{4.4}$$

Then, integrating the foregoing equation and applying the first boundary condition of eq. (4.3), we write

$$X = \int_0^{Y(X)} \frac{G(Y)}{\sqrt{1 - G(Y)^2}} dY. \tag{4.5}$$

Equation (4.5) is not amenable to an explicit closed form solution in terms of elementary functions. However, letting $G_1 = G(Y(1))$ and simplifying the results, a standard form of elliptic integral solution may be obtained as

$$X = \pm \int_{|\cos(\phi)|}^{G(Y)} \frac{1}{\sqrt{1 - G^2}} \frac{G}{\sqrt{\beta^2 - 2\alpha^2(G - G_1)}} dG. \tag{4.6}$$

Had one replaced $\mathbf{R}(\phi)$ with its transpose ($\mathbf{R}^T(\phi)$) in the coordinates transformation (4.1), a similar result would have been obtained. However, both solutions are qualitatively similar, and have no major advantage over each other. It is worth mentioning that Ref. [75] also reported a solution procedure for obtaining a cartesian large deflection solution. However, their coordinates transformation is not based on rotation and is somewhat more complex than the rather compact eq. (4.6).

The inextensibility of the beam imposes a side condition, which would further constrain the trajectory of the beam's endpoints as

$$1 = \pm \int_{|\cos(\phi)|}^{G_1} \frac{1}{\sqrt{1 - G^2}} \frac{1}{\sqrt{\beta^2 - 2\alpha^2(G - G_1)}} dG. \tag{4.7}$$

It is clear that the new cartesian elliptic integral large deflection solution (4.6) retains the main shortcomings of the elliptic large deflection solutions (3.8) and (3.9). Even though the new solution involves only x and y, it is implicit and highly nonlinear, thus, still requires sophisticated numerical evaluation techniques. Likewise, the new solution has still two branches, and the identification of the right branch for any input loading parameters requires careful assessment. However, the square root in eq. (4.4) is bounded below by one, thus, we have $0 < G(Y) \leq 1$. This paves the way for fairly accurate approximations through neglecting higher powers of the quadratic function $G(Y)$ in the aforementioned formulae. Considered as future work, such assumptions facilitate obtaining efficient approximate closed form solutions in terms of elementary functions. Nonetheless, we aim to obtain solutions, which are accurate for arbitrary applied loadings. In what follows, we develop piecewise parametric large deflection solutions, which are rapidly convergent and easily implementable as a stand-alone black-box solver.

4.2 Piecewise Parametric Large Deflection Solutions

For convenience, eqs. (3.10)-(3.13) are given below:

$$\frac{d^2\psi(s)}{ds^2} = \alpha^2 \sin(\psi(s)), \tag{4.8}$$

$$\psi(0) = -\phi, \quad \frac{d\psi(1)}{ds} = \beta, \tag{4.9}$$

$$\frac{dx(s)}{ds} = \cos(\psi(s) + \phi), \quad x(0) = 0, \tag{4.10}$$

$$\frac{dy(s)}{ds} = \sin(\psi(s) + \phi), \quad y(0) = 0, \tag{4.11}$$

where $\psi(s) \triangleq \theta(s) - \phi$.

From Chapter 3, we know that the foregoing equations have explicit exact solutions for only a pure end-moment loading, and no explicit solution is reported in the literature for a general pure end-force loading. However, for a sufficiently large applied end-force, the results of Subsubsection 3.4.1 from Chapter 3 suggest that beam's end angle approaches the force angle, i.e., $\theta_1 \approx \phi$. Utilizing this result, eq. (3.7) can be simplified and solved analytically. For $\beta = 0$ and $\theta_1 = \phi$, we give the exact solution of eqs. (3.3) and (3.4) as

$$\theta(s) = \phi - 4\arctan(\tan(\frac{\phi}{4})\exp(-\alpha s)), \tag{4.12}$$

which is valid for both elbow up and down solution branches. To get the corresponding axial deflection components, we integrated eqs. (3.8) and (3.9), and used the trigonometric identities

$$\begin{cases} \cos(4\arctan(z)) & = & 1 - 8\frac{z^2}{(1+z^2)^2}, \\ \sin(4\arctan(z)) & = & 4z\frac{1-z^2}{(1+z^2)^2}, \end{cases}$$

to write

$$\begin{bmatrix} x(s) \\ y(s) \end{bmatrix} = \overbrace{\begin{bmatrix} \cos(\phi) & -\sin(\phi) \\ \sin(\phi) & \cos(\phi) \end{bmatrix}}^{\mathbf{R}^{\mathrm{T}}(\phi)} \begin{bmatrix} s - \frac{4}{\alpha}\left(\frac{1}{1+\tan^2(\phi/4)\exp(-2\alpha s)} - \frac{1}{1+\tan^2(\phi/4)}\right) \\ \frac{4}{\alpha}\left(\frac{\tan(\phi/4)\exp(-\alpha s)}{1+\tan^2(\phi/4)\exp(-2\alpha s)} - \frac{\tan(\phi/4)}{1+\tan^2(\phi/4)}\right) \end{bmatrix}, \tag{4.13}$$

in which the manifestation of the rotation matrix $\mathbf{R}(\phi)$ is in analogy with the cartesian solutions given in the previous section. The outrageous discrepancy in the form of the exact circular large deflection solution, given in Subsection 3.3.1 of Chapter 3, and the newly developed closed form large deflection solution just underlines the complexity of the beam behavior and the need for a robust solution procedure.

For $i = 1, \ldots, n$, let $[s_i, s_{i+1}]$ be a subdivision of the computational domain $s \in [0, 1]$ such that $\cup_{i=1}^{n}[s_i, s_{i+1}] = [0, 1]$, where $s_1 = 0$ and $s_{n+1} = 1$. In addition, let $\theta_i(s)$, $x_i(s)$, and $y_i(s)$ denote the deflection components corresponding to $s \in [s_i, s_{i+1}]$. Employing ATET, the parametric large deflection solutions corresponding to each subdivision are written as

$$\theta_i(s) = \phi + c_{0i} + c_{1i}(s - s_{0i}) + \alpha^2 \lim_{\mathcal{M}_{1i}\to\infty} \sum_{j=2}^{\mathcal{M}_{1i}} \frac{1}{j!} \frac{d^{j-2}}{ds^{j-2}} \left(\sin(\psi(s))\right)\Big]_{s=s_{0i}} (s - s_{0i})^j, \quad (4.14)$$

$$x_i(s) = x_{0i} + \lim_{\mathcal{M}_{2i}\to\infty} \sum_{j=1}^{\mathcal{M}_{2i}} \frac{1}{j!} \frac{d^{j-1}}{ds^{j-1}} \left(\cos(\psi(s) + \phi)\right)\Big]_{s=s_{0i}} (s - s_{0i})^j, \quad (4.15)$$

and

$$y_i(s) = y_{0i} + \lim_{\mathcal{M}_{3i}\to\infty} \sum_{j=1}^{\mathcal{M}_{3i}} \frac{1}{j!} \frac{d^{j-1}}{ds^{j-1}} \left(\sin(\psi(s) + \phi)\right)\Big]_{s=s_{0i}} (s - s_{0i})^j, \quad (4.16)$$

where $s_{0i} \in [s_i, s_{i+1}]$, $c_{0i} = \psi_i(s_{0i})$, $c_{1i} = \frac{d\psi_i(s_{0i})}{ds}$, $x_{0i} = x_i(s_{0i})$, $y_{0i} = y_i(s_{0i})$, and finally $\mathcal{M}_{1i}$, $\mathcal{M}_{2i}$, and $\mathcal{M}_{3i}$ are the approximation orders. Note that all of the summation terms are at hand, as the higher order derivatives of $\psi(s)$ can be found in terms of c_{0i} and c_{1i} upon successively differentiating eq. (4.8). Accordingly, there are $4n$ unknowns, i.e., $\mathcal{C}_{4n} = \{c_{0i}, c_{1i}, x_{0i}, y_{0i}\}$, which are needed to be identified to fully define the piecewise parametric large deflection solutions. To this end, requiring the continuity in the zeroth and first order derivatives of the piecewise angular solutions at the interfaces, and continuity in piecewise axial deflections, together with the original boundary conditions (4.9)-(4.11) constitute the $4n$ algebraic-trigonometric constraints

$$\mathcal{B}(\mathcal{C}_{4n}) = \left\{ \begin{array}{c} \theta_1(0) = 0 \\ \\ \frac{d\theta_n}{ds}(1) = \beta \\ \\ x_1(0) = 0 \\ \\ y_1(0) = 0 \end{array} \right\} \cup \left\{ \left. \begin{array}{c} \theta_j(s_{j+1}) = \theta_{j+1}(s_{j+1}) \\ \\ \frac{d\theta_j}{ds}(s_{j+1}) = \frac{d\theta_{j+1}}{ds}(s_{j+1}) \\ \\ x_j(s_{j+1}) = x_{j+1}(s_{j+1}) \\ \\ y_j(s_{j+1}) = y_{j+1}(s_{j+1}) \end{array} \right. , \quad j = 1, \ldots, n-1 \right\}, \quad (4.17)$$

which may be solved for the entire unknowns.

For instance, taking $n = 2$ (i.e., $i = 1, 2$) and $\mathcal{M}_{1i} = \mathcal{M}_{2i} = \mathcal{M}_{3i} = 5$, the fifth order piecewise ATET solutions for $\theta_i(s)$, $x_i(s)$, and $y_i(s)$ may be written as

$$\theta(s) = \begin{cases} \left\{ \begin{array}{r} \phi + c_{01} + \frac{c_{11}}{1!}(s - s_{01}) + \frac{\alpha_{s1}}{2!}(s - s_{01})^2 + \frac{c_{11}\alpha_{c1}}{3!}(s - s_{01})^3 \\ + \frac{\alpha_{s1}\eta_{11}}{4!}(s - s_{01})^4 + \frac{c_{11}\left(\alpha_{c1}\eta_{21} - 3\alpha^4\right)}{5!}(s - s_{01})^5 \end{array} \right. , & 0 \leq s \leq s_2, \\ \left\{ \begin{array}{r} \phi + c_{02} + \frac{c_{12}}{1!}(s - s_{02}) + \frac{\alpha_{s2}}{2!}(s - s_{02})^2 + \frac{c_{12}\alpha_{c2}}{3!}(s - s_{02})^3 \\ + \frac{\alpha_{s2}\eta_{12}}{4!}(s - s_{02})^4 + \frac{c_{12}\left(\alpha_{c2}\eta_{22} - 3\alpha^4\right)}{5!}(s - s_{02})^5 \end{array} \right. , & s_2 \leq s \leq 1, \end{cases} \tag{4.18}$$

$$x(s) = \\ \begin{cases} \left\{ \begin{array}{c} x_{01} + \frac{\cos(\tilde{c}_{01})}{1!}(s - s_{01}) - \frac{c_{11}\sin(\tilde{c}_{01})}{2!}(s - s_{01})^2 \\ - \frac{c_{11}^2\cos(\tilde{c}_{01}) + \alpha_{s1}\sin(\tilde{c}_{01})}{3!}(s - s_{01})^3 - \frac{c_{11}(3\alpha_{s1}\cos(\tilde{c}_{01}) + \eta_{11}\sin(\tilde{c}_{01}))}{4!}(s - s_{01})^4 \\ - \frac{\alpha_{s1}\eta_{31}\sin(\tilde{c}_{01}) + \eta_{41}\cos(\tilde{c}_{01})}{5!}(s - s_{01})^5, \end{array} \right. & 0 \leq s \leq s_2, \\ \left\{ \begin{array}{c} x_{02} + \frac{\cos(\tilde{c}_{02})}{1!}(s - s_{02}) - \frac{c_{12}\sin(\tilde{c}_{02})}{2!}(s - s_{02})^2 \\ - \frac{c_{12}^2\cos(\tilde{c}_{02}) + \alpha_{s2}\sin(\tilde{c}_{02})}{3!}(s - s_{02})^3 - \frac{c_{12}(3\alpha_{s2}\cos(\tilde{c}_{02}) + \eta_{12}\sin(\tilde{c}_{02}))}{4!}(s - s_{02})^4 \\ - \frac{\alpha_{s2}\eta_{32}\sin(\tilde{c}_{02}) + \eta_{42}\cos(\tilde{c}_{02})}{5!}(s - s_{02})^5, \end{array} \right. & s_2 \leq s \leq 1, \end{cases} \tag{4.19}$$

and

$$y(s) = \\ \left\{ \begin{array}{ll} \left\{ \begin{array}{c} y_{01} + \frac{\sin(\tilde{c}_{01})}{1!}(s - s_{01}) + \frac{c_{11}\cos(\tilde{c}_{01})}{2!}(s - s_{01})^2 \\ -\frac{c_{11}^2 \sin(\tilde{c}_{01}) - \alpha_{s1}\cos(\tilde{c}_{01})}{3!}(s - s_{01})^3 - \frac{c_{11}(3\alpha_{s1}\sin(\tilde{c}_{01}) - \eta_{11}\cos(\tilde{c}_{01}))}{4!}(s - s_{01})^4 \\ + \frac{\alpha_{s1}\eta_{31}\cos(\tilde{c}_{01}) - \eta_{41}\sin(\tilde{c}_{01})}{5!}(s - s_{01})^5, \end{array} \right. & 0 \le s \le s_2, \\ \left\{ \begin{array}{c} y_{02} + \frac{\sin(\tilde{c}_{02})}{1!}(s - s_{02}) + \frac{c_{12}\cos(\tilde{c}_{02})}{2!}(s - s_{02})^2 \\ -\frac{c_{12}^2 \sin(\tilde{c}_{02}) - \alpha_{s2}\cos(\tilde{c}_{02})}{3!}(s - s_{02})^3 - \frac{c_{12}(3\alpha_{s2}\sin(\tilde{c}_{02}) - \eta_{12}\cos(\tilde{c}_{02}))}{4!}(s - s_{02})^4 \\ + \frac{\alpha_{s2}\eta_{32}\cos(\tilde{c}_{02}) - \eta_{42}\sin(\tilde{c}_{02})}{5!}(s - s_{02})^5, \end{array} \right. & s_2 \le s \le 1, \end{array} \right. \tag{4.20}$$

where $\tilde{c}_{0i} = c_{0i} + \phi$, $\alpha_{si} = \alpha^2 \sin(c_{0i})$, $\alpha_{ci} = \alpha^2 \cos(c_{0i})$, $\eta_{1i} = \alpha_{ci} - c_{1i}^2$, $\eta_{2i} = 4\alpha_{ci} - c_{1i}^2$, $\eta_{3i} = \alpha_{ci} - 7c_{1i}^2$, and finally $\eta_{4i} = c_{1i}^2\eta_{2i} + 3\alpha_{si}^2$ for $i = 1, 2$. Note that s_{01}, s_{02}, and s_2 are to be chosen as input parameters, thus, leaving only eight unknowns $\mathcal{C}_8 = \{c_{01}, c_{11}, c_{02}, c_{12}, x_{01}, x_{02}, y_{01}, y_{02}\}$, which would be identified upon imposing the boundary conditions $\mathcal{B}(\mathcal{C}_8)$, an adaptation of $\mathcal{B}(\mathcal{C}_{4n})$ for this special case.

4.2.1 Choice of the Number of Subdivisions n

The more the number of subdivisions, the more accurate the piecewise solutions. However, more subdivisions introduce significant number of intermediate unknowns, which would burden the computation. Nevertheless, an increase in the number of subdivisions reduces the need for large approximation orders, which are generally required for attaining a significant accuracy. To get a good balance between solution accuracy and computational cost, we set $n = 2$, for which the resulting large deflection solutions are highly accurate and rather compact.

4.2.2 Choice of the Segments' Endpoints s_i and s_{i+1}

Recall that the premise of the piecewise solutions is the Taylor series expansion, which approximates the unknown exact large deflection solutions with polynomials in the arc length of the beam. It is clear that the smaller the computational domain, i.e., the length of the arc length for each piecewise solution, the better the accuracy of the approximations. However, for a fixed number of subdivisions and fixed approximations orders, improving the accuracy of each piecewise solution requires shortening the length of that segment, which would force compromising the accuracy of the remaining segment solutions. Therefore, to avoid this, the optimal subdivision is to subdivide the beam length equally, i.e., $[s_i, s_{i+1}] = [(i-1), i]/n$ for $i = 1, \ldots, n$.

4.2.3 Choice of the Start Points s_{0i}

The piecewise solutions also depend on start points s_{0i}, which are to be chosen. Like the parametric solution presented in Chapter 3, start points can simplify the solution procedure. For example, the unknowns $\{c_{01}, c_{1n}, x_{01}, y_{01}\}$ would become known parameters, if s_{01} and s_{0n} are taken as $s_1 = 0$ and $s_{n+1} = 1$, respectively. In contrast, setting s_{0i} to the center of each segment provides the most accuracy and convergence.

4.2.4 Independence of the Approximation Orders

Following the discussion of Subsection 2.3.6, any of the approximation orders $\mathcal{M}_{1i}$, $\mathcal{M}_{2i}$, and $\mathcal{M}_{3i}$ can be chosen independently. This is significant in two ways. The accuracy of any of the angular and axial deflection components can be exclusively adjusted without disturbing the accuracy of the remaining solution components. Likewise, the accuracy of each segment solution can be adapted without affecting the accuracy of the remaining segment solutions. Taken the piecewise solutions given by eq. (4.18) as an example, the accuracy of the angular solution on the domain of $s \in [0, s_2]$ can be controlled independently of that of $s \in [s_2, 1]$, and vice versa.

4.2.5 Solution of the Boundary Constraints $\mathcal{B}(\mathcal{C}_{4n})$

The system of boundary constraints $\mathcal{B}(\mathcal{C}_{4n})$ (4.17) is a decoupled system of algebraic-trigonometric equations. To solve it efficiently, the angular constraints can be solved for c_{0i} and c_{1i} independently of the axial constraints. Then, the resulting solutions can be inserted into the horizontal and vertical deflection constraints so as to solve for x_{0i} and y_{0i}, respectively.

One major advantage of the piecewise solution procedure over the single-piece solution approach of Chapter 3 is that the boundary constraints, i.e., $\mathcal{B}(\mathcal{C}_{4n})$, of the former are relatively far more well-conditioned than those of the latter. For the latter, the boundary constraints can be converted into a system of polynomial equations, and solved for the entire solution set, among which the true solutions can be sought. However, this approach is rather inefficient, and impractical for daily engineering applications.

In contrast, we employ the Newton–Raphson technique, which initiates at a given start solution and iteratively updates it to converge to a feasible solution. Even though multiple solutions may exist, we have found that the Newton–Raphson technique, starting at a zero solution set, has constantly converged to the true solution for $\mathcal{B}(\mathcal{C}_{4n})$. This feature has led us to coding the algorithm as a black-box simulation software, which is discussed in the next section.

4.3 ***BeamSol***: A Large Deflection ***Beam Sol***ver

To demonstrate the effectiveness of our solution procedure, we coded our algorithm as a black-box solver using *Visual C++*. Our large deflection beam solver, *BeamSol 1.0*, provides various user-friendly functionalities, including plotting, sampling, and exporting the solutions to a data file.

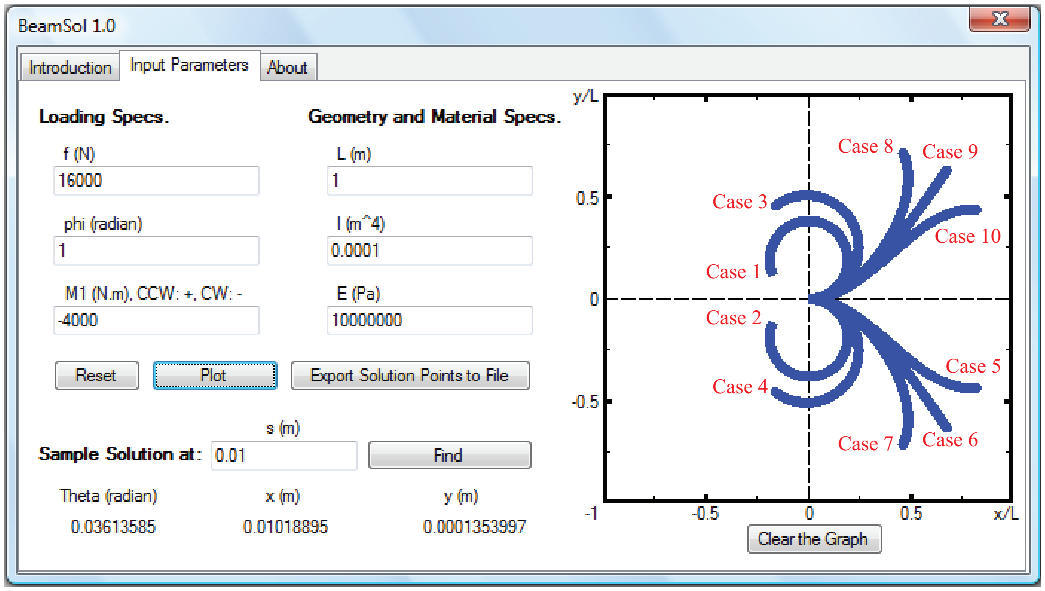
BeamSol 1.0
Introduction
Input Parameters
About
Reset
Plot
Export Solution Points to File
Find
Clear the Graph
y/L
x/L
0.5
0
-0.5
-1
-0.5
0
0.5
Case 1
Case 2
Case 3
Case 4
Case 5
Case 6
Case 7
Case 8
Case 9
Case 10

Loading Specs.

f (N): 16000

phi (radian): 1

M1 (N.m), CCW: +, CW: -: -4000

Geometry and Material Specs.

L (m): 1

I (m^4): 0.0001

E (Pa): 10000000

Sample Solution at: s (m): 0.01

Theta (radian)	x (m)	y (m)
0.03613585	0.01018895	0.0001353997

Figure 4.1: A snapshot of *BeamSol 1.0* corresponding to the ten cases of input data given in Table 4.1. The annotations in red are added manually for illustration purposes.

For the special case of pure end-moment, *BeamSol 1.0* employs the circular exact solution of Subsection 3.3.1, and for a general loading it employs, currently, the two-piece fifth order ATET solutions given by eqs. (4.18)-(4.20), but is envisioned to offer various number of pieces and approximation orders in the very near future. For the solution of boundary constraints, as discussed earlier, the Newton–Raphson technique is implemented and a zero solution set is used. To validate the results of *BeamSol 1.0*, we ran it for many randomly generated input data, and the results were successfully compared against those of the previous chapter and the numerical differential solver of Mathematica. The executable is to be posted online for free download.

Figure 4.1 depicts a snapshot of *BeamSol 1.0*, which plots the cartesian large deflection components for ten cases that are listed in Table 4.1.

Table 4.1: Input data used for Figure 4.1. For all cases: $l = 1$ (m), $I = 10^{-4}$ (m^4), and $E = 10$ (MPa).

Parameter \ Case #	1	2	3	4	5	6	7	8	9	10
f (kN)	0	0	1	1	16	16	16	16	16	16
ϕ $(radian)$	–	–	2	-2	-1	-1	-1	1	1	1
M_1 $(kN.m)$	5	-5	4	-4	4	0	-4	4	0	-4

4.4 Summary and Conclusions

This chapter presented cartesian large deflection solutions, which are independent of the beam's arc length. The solutions are implicit and in terms of elliptic integrals, but are envisioned to guide the development of approximate closed form large deflection solutions. For the case of a large pure end-force, a new closed form solution was also presented which incorporated the rotation matrix employed for developing the aforementioned cartesian large deflection solutions. To add further efficiency and robustness to the single piece parametric solutions of the previous chapter, piecewise large deflection solutions were also developed which require low approximation orders for a fast convergence. These solutions were coded as a stand-alone black-box solver, which offers several functionalities for the solution of large deflection of Euler–Bernoulli cantilever beams. The executable will be posted for free download for those who are interested in beam applications.

Chapter 5

Calculation of the 3D Hysteretic Magnetization and Magnetostriction of Iron-Gallium Alloys

Thus far, simulation tools were discussed and developed for a passive Euler–Bernoulli material. From this chapter on, the focus is given to smart materials, in particular, *Magnetostrictive* materials. Results of this chapter are also documented in Ref. [44].

The Discrete Energy-Averaged model (DEA) calculates the magnetization unit directions that minimize a Gibbs free energy defined locally about the six easy directions. However, the resulting minimization problem is not amenable to an explicit analytical solution. To alleviate this shortcoming, Evans and Dapino [42] linearized the normalization constraint about each easy direction, which is valid for small rotations of the magnetic moments about the easy directions. This novel treatment resulted in an explicit approximate solution, whose error is minimal since moments that have rotated far from the easy axes are more energetic, thus, are less probable. Nonetheless, the approximate magnetization directions may significantly violate the unity norm constraint for large inputs. Post-normalization of the directions was proposed by Chakrabarti and Dapino [76], but the resulting directions can still deviate from the true energy minima for generic 3D inputs. Additionally, this solution procedure is prone to singularities, which could burden the computation, especially when the method is integrated into finite-element solvers.

Design and optimization of magnetostrictive systems using finite-element techniques require constitutive models that are robust and valid for arbitrary magnetic field and stress inputs. The primary objective of this chapter is to develop a robust solution procedure for the DEA model that avoids singularities. First, the DEA model is improved by incorporating the more thorough expression for the magnetostriction in cubic ferromagnets and by formulating the model based on the average of hysteretic data, which precludes the need for additional anhysteretic data. Then, an analytical solution of the resulting model is derived that exactly solves the constrained energy minimization. Depending on the dimension of the application, the solution procedure offers multiple solutions for each easy direction which allows it to circumvent singularities and to completely reveal the material behavior for arbitrary magnetic field and stress inputs. By using the analytical solution, the model is significantly reduced for 2D and 1D applications. A novel parameter optimization routine is developed, which decouples the model parameters into two sets. One set is quickly calculated through a preprocessing step, while the other is determined through a sophisticated constrained minimization. It is shown that the increased robustness of the proposed model comes at no expense for 1D applications, but requires twice the computation time for generic 3D applications. The model is validated through comparison with existing measurements and the former model.

The rest of this chapter is organized as follows. A brief review of the DEA model and the existing approximate solution is shown in Section 5.1. Subsection 5.2.1 presents a reformulation of the DEA model and the analytical solution procedure. Section 5.3 gives the reduced formulation of the model for 2D and 1D applications. Parameter optimization is discussed in Section 5.4, which is followed by model validation and the conclusions.

5.1 Review of calculation of the 3D magnetostriction and magnetic flux density for Galfenol

Evans and Dapino [42] proposed a discrete energy-averaged (DEA) model that computes the magnetization directions of mesoscopic magnetic domains by minimizing the Gibbs free energy that is defined locally about each easy crystallographic direction. Gibbs free energy was chosen, as it takes magnetic field and stress vectors as independent variables. The Gibbs free energy in the vicinity of the kth easy direction is composed of magnetocrystalline (anisotropy), magnetoelastic (magnetomechanical coupling), and magnetic field (Zeeman) energies. The minimization procedure applied to Evans and Dapino's formulation requires as many matrix inversions as the number of easy directions. To reduce the number of matrix inversions to one, Chakrabarti [43] slightly modified the anisotropy energy. Accordingly, the Gibbs free energy can be written in matrix notation as

$$\overset{k}{G} = \frac{1}{2}\,\overset{k}{\mathbf{m}}\cdot\overline{\mathbf{K}}\,\overset{k}{\mathbf{m}} - \overset{k}{\mathbf{b}}\cdot\overset{k}{\mathbf{m}} + \frac{1}{2}K + \overset{k}{K}_0, \tag{5.1}$$

where K and $\overset{k}{K}_0$ are anisotropy energy constants; $\overset{k}{\mathbf{m}} = [\overset{k}{m}_1; \overset{k}{m}_2; \overset{k}{m}_3]$ is the magnetization direction having unit magnitude; k takes values $\pm 1, \ldots, \pm\frac{r}{2}$; and r is the number of easy crystallographic directions (the $\langle 100\rangle$ family of six directions for Galfenol). The magnetic stiffness matrix $\overline{\mathbf{K}}$ and magnetic force vector $\mathbf{b}$ along the kth easy direction are given by

$$\overline{\mathbf{K}} = K\mathbf{I} - 3\begin{bmatrix} \lambda_{100}T_1 & \lambda_{111}T_4 & \lambda_{111}T_6 \\ \lambda_{111}T_4 & \lambda_{100}T_2 & \lambda_{111}T_5 \\ \lambda_{111}T_6 & \lambda_{111}T_5 & \lambda_{100}T_3 \end{bmatrix}, \tag{5.2}$$

and

$$\overset{k}{\mathbf{b}} = K \overset{k}{\mathbf{c}} + \mu_0 M_s \mathbf{H}, \tag{5.3}$$

respectively, where $\mathbf{I}$ is the 3×3 identity matrix; λ_{100} and λ_{111} are magnetostriction constants; μ_0 and M_s are, respectively, the vacuum permeability and saturation magnetization; $\mathbf{H} = [H_1; H_2; H_3]$ is the magnetic field vector; and $\mathbf{T} = [T_1; T_2; T_3; T_4; T_5; T_6]$ stands for the stress tensor written in contracted vector notation, where $T_1 = T_{11}$, $T_2 = T_{22}$, $T_3 = T_{33}$, $T_4 = T_{12}$, $T_5 = T_{23}$, and $T_6 = T_{13}$.

The macroscopic 3D magnetostriction $\boldsymbol{\lambda}$ and magnetization $\mathbf{M}$ are defined as weighted sums of the response due to the r minimum energy directions,

$$\boldsymbol{\lambda} \triangleq \overline{\boldsymbol{\lambda}} = \sum_{k=\pm 1}^{\pm r/2} \overset{k}{\xi}_{an} \overset{k}{\boldsymbol{\lambda}}, \tag{5.4}$$

$$\mathbf{M} \triangleq \overline{\mathbf{M}} = M_s \sum_{k=\pm 1}^{\pm r/2} \overset{k}{\xi}_{an} \overset{k}{\mathbf{m}}, \tag{5.5}$$

where $\overset{k}{\xi}_{an}$ and $\overset{k}{\boldsymbol{\lambda}}$ denote, respectively, the bulk anhysteretic volume fraction and the magnetostriction tensor written in vector notation for the kth easy direction. Letting Ω be a smoothing factor, the former is calculated as a Boltzman-type, energy-weighted average as

$$\overset{k}{\xi}_{an} = \exp\left(-\frac{\overset{k}{G}}{\Omega}\right) \sum_{j=\pm 1}^{\pm r/2} \exp\left(\frac{\overset{j}{G}}{\Omega}\right), \tag{5.6}$$

and the magnetostriction in tensor notation is given as

$$\begin{aligned} &\overset{k}{\boldsymbol{\lambda}}_{uu} = \frac{3}{2}\lambda_{100} \overset{k}{m}_u{}^2 \\ &\overset{k}{\boldsymbol{\lambda}}_{uv} = 3\lambda_{111} \overset{k}{m}_u \overset{k}{m}_v, \quad u \neq v \end{aligned} \quad , \quad u, v \in \{1, 2, 3\}. \tag{5.7}$$

5.1.1 Calculation of $\overset{k}{\mathbf{m}}$ (approximate solution)

The application of an external magnetic field or stress changes the energy surface in the vicinity of each easy crystallographic direction, which may shift the kth minimum energy direction away from the kth easy direction. Thus, the unit magnitude, minimum energy directions **m** are not known *a priori* for each easy direction, and must be calculated by minimizing the local free energies (5.1) before evaluating the volume fractions (5.6). Following Evans and Dapino [42], the constrained minimization is formulated as the following inhomogeneous eigenvalue problem through the application of the Lagrange multipliers method

$$(\overline{\mathbf{K}} - \overset{k}{\gamma}\, \mathbf{I})\, \overset{k}{\mathbf{m}} = \overset{k}{\mathbf{b}}, \tag{5.8a}$$

$$\overset{k}{\mathbf{m}} \cdot \overset{k}{\mathbf{m}} = 1, \tag{5.8b}$$

where $\overset{k}{\gamma}$ is the unknown Lagrange multiplier corresponding to the kth minimum energy direction. In the absence of an explicit, analytical solution to the foregoing system of equations, Evans and Dapino [42] relaxed the normalization constraint through the approximation $\mathbf{m}\cdot\mathbf{m} \approx \mathbf{c}\cdot\mathbf{m} = 1$ for each easy direction. As a result, the following explicit, approximate solution was reported:

$$\overset{k}{\mathbf{m}} \approx [\overline{\mathbf{K}}]^{-1} \left[\overset{k}{\mathbf{b}} + \left(\frac{1 - \overset{k}{\mathbf{c}} \cdot [\overline{\mathbf{K}}]^{-1}\, \overset{k}{\mathbf{b}}}{\overset{k}{\mathbf{c}} \cdot [\overline{\mathbf{K}}]^{-1}\, \overset{k}{\mathbf{c}}} \right) \overset{k}{\mathbf{c}} \right]. \tag{5.9}$$

5.1.2 Magnetomechanical hysteresis

Dissipation of energy creates a history dependence on the material's response. Material's lag in response for the same inputs but at different states is commonly known as hysteresis. The anisotropy energy is one source to account for the dissipation of energy in the aforementioned Gibbs free energy formulation. Evans and Dapino [42] presented an incremental form of hysteresis based upon an evolution equation for the volume fractions,

$$\Delta \overset{k}{\xi}(i) = (1-c)\Delta \overset{k}{\xi}_{irr}(i) + c\Delta \overset{k}{\xi}_{an}(i), \tag{5.10}$$

where i is the increment index, c is a dimensionless constant quantifying the reversible processes during domain wall motion, and finally the change in the irreversible volume fractions for 3D stress and field inputs is defined as

$$\begin{aligned} \Delta \overset{k}{\xi}_{irr}(i) = & \frac{\zeta}{k_p}\left(\overset{k}{\xi}_{an}(i) - \overset{k}{\xi}_{irr}(i-1)\right) \\ & \times \left[\mu_0 M_s \sum_{p=1}^{3} |\Delta H_p(i)| + (3/2)\lambda_{100} \sum_{p=1}^{3} |\Delta T_p(i)| + 3\lambda_{111} \sum_{q=4}^{6} |\Delta T_q(i)| \right], \end{aligned} \tag{5.11}$$

where ζ is a binary number for avoiding a nonphysical negative susceptibility, and k_p is a pinning site density constant that characterizes the energy loss associated with domain wall rotation. Note that this hysteresis model is not self-starting, because the initial irreversible volume fractions are undefined. However, it is common practice to assume that $\xi_{irr}(0) = 0$.

5.2 Reformulation of the DEA Model with Exact Solution Procedure

The ultimate goal of this chapter is to model Galfenol's hysteretic behavior. Therefore, we reformulate the DEA model based on the average of hysteretic data, as opposed to anhysteretic data, which would require additional measurements for parameter optimization and validation. In essence, we employ the averaged hysteretic volume fractions, i.e., $\overline{\xi}_{hys}$, which correspond to the median curves obtained from averaging the hysteretic measurement data. Thus, every occurrence of ξ_{an} in the previous model is replaced by $\overline{\xi}_{hys}$ in the new model. To be precise, eqs. (5.4)-(5.6), which define the nonhysteretic model, become

$$\boldsymbol{\lambda} \triangleq \overline{\boldsymbol{\lambda}} = \sum_{k=\pm1}^{\pm r/2} \overset{k}{\overline{\xi}}_{hys} \overset{k}{\boldsymbol{\lambda}}, \tag{5.12}$$

$$\mathbf{M} \triangleq \overline{\mathbf{M}} = M_s \sum_{k=\pm1}^{\pm r/2} \overset{k}{\overline{\xi}}_{hys} \overset{k}{\mathbf{m}}, \tag{5.13}$$

$$\overset{k}{\overline{\xi}}_{hys} = \exp\left(-\frac{\overset{k}{G}}{\Omega}\right) \sum_{j=\pm1}^{\pm r/2} \exp\left(\frac{\overset{j}{G}}{\Omega}\right), \tag{5.14}$$

where the parameters in the Gibbs free energy are optimized against the averaged hysteretic data; and finally eqs. (5.10) and (5.11), which constitute the hysteretic model, become

$$\Delta \overset{k}{\xi}(i) = (1-c)\Delta \overset{k}{\xi}_{irr}(i) + c\Delta \overset{k}{\overline{\xi}}_{hys}(i), \tag{5.15}$$

$$\begin{aligned} \Delta \overset{k}{\xi}_{irr}(i) = & \frac{\zeta}{k_p}\left(\overset{k}{\overline{\xi}}_{hys}(i) - \overset{k}{\xi}_{irr}(i-1)\right) \\ & \times \left[\mu_0 M_s \sum_{p=1}^{3} |\Delta H_p(i)| + (3/2)\lambda_{100} \sum_{p=1}^{3} |\Delta T_p(i)| + 3\lambda_{111} \sum_{q=4}^{6} |\Delta T_q(i)|\right], \end{aligned} \tag{5.16}$$

We also reformulate the magnetoelastic energy. Evans and Dapino [42] used the tensor-valued magnetostriction, eq. (5.7), given by Engdahl [77]. Instead, we use the more thorough formulation of Kittel [78] with a constant term not present in the book by Engdahl. Kittel's expressions are given in component tensor notation as

$$\begin{aligned}\overset{k}{\boldsymbol{\lambda}}_{uu} &= \frac{3}{2}\lambda_{100}(\overset{k}{m}_u{}^2 - \overbrace{\frac{c_{12}}{c_{11}+2c_{12}}}^{\triangleq\, c_0}), \\ \overset{k}{\boldsymbol{\lambda}}_{uv} &= 3\lambda_{111}\ \overset{k}{m}_u \overset{k}{m}_v, \quad u \neq v,\end{aligned} \tag{5.17}$$

where $u, v \in \{1, 2, 3\}$, and c_{11} and c_{12} are two of the three independent elastic moduli for crystals with cubic symmetry. Relative to Engdahl's equation used in the prior work, employment of eq. (5.17) provides a better fit of the model to experimental data for the sensing case, as detailed in Subsection 5.5.1.

5.2.1 Calculation of $\overset{k}{\mathbf{m}}$ (exact solution)

The approximate solution (5.9) has the advantage of simplicity and explicitness. However, the approximate magnetization direction obtained from eq. (5.9) violates the unity norm constraint when the material is saturated by large magnetic fields or stresses. Referring to eq. (5.5), this results in a nonphysical magnetization (i.e., larger than the saturation magnetization M_s). One way to circumvent this issue is to normalize the approximate solution following its calculation [42, 43]. Although this might seem effective, the solution does not truly reflect the genuine solution of the system of eqs. (5.8). Additionally, the approximate method fails to provide a solution when the matrix $\overline{\mathbf{K}}$ becomes singular. For a planar stress state, i.e., $T_3 = T_5 = T_6 = 0$, this singularity occurs on the surface depicted in Figure 5.1, where the determinant sub-locus of the matrix $\overline{\mathbf{K}}$ is shown. An ill-conditioned matrix $\overline{\mathbf{K}}$ can also cause numerical difficulties, expanding the failure surface into a volume. Although planar stress is a special case, it is apparent that the singularity zone enlarges when the stress state is generic. The failure zone of such a case has too many dimensions to show graphically, but it is governed by the determinant constraint $|\overline{\mathbf{K}}| < \epsilon$, where ϵ is a small number. The need for a more robust model is further motivated considering that this constitutive model has been integrated into finite-element models for the simulation of Galfenol-based systems [76, 79]. The utility of such finite-element models for use by non-experts is hampered if the model does not incorporate a black-box constitutive model that is valid for all inputs.

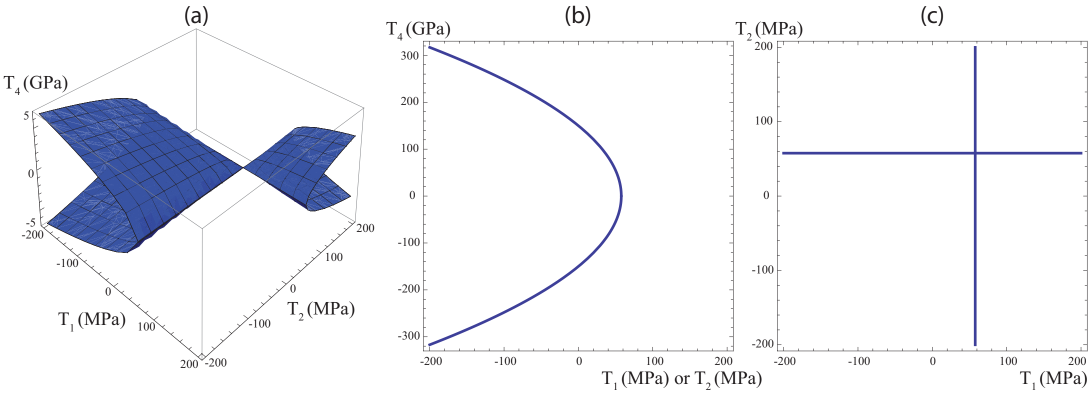

Figure 5.1: (a) The determinant sub-locus of the matrix $\overline{\mathbf{K}}$ corresponding to planar stress for $K = 3 \times 10^4$, $3\lambda_{100} = 520 \times 10^{-6}$, and $3\lambda_{111} = -20 \times 10^{-6}$, (b) slice plot for $T_1 = 0$ or $T_2 = 0$, and (c) slice plot for $T_4 = 0$.

Before developing the exact solution procedure, we simplify the Gibbs free energy (5.1) using the unity norm constraint on the magnetization directions (5.8b) as

$$\overset{k}{G} = \frac{1}{2}\overset{k}{\mathbf{m}} \cdot \overline{\mathbf{K}}\,\overset{k}{\mathbf{m}} - \overset{k}{\mathbf{b}} \cdot \overset{k}{\mathbf{m}} + \frac{1}{2}K + \overset{k}{K_0} = \frac{1}{2}\overset{k}{\mathbf{m}} \cdot \mathbf{K}\,\overset{k}{\mathbf{m}} - \overset{k}{\mathbf{b}} \cdot \overset{k}{\mathbf{m}} + K + \overset{k}{K_0}, \qquad (5.18)$$

where the simplified magnetic stiffness matrix is

$$\mathbf{K} = -3 \begin{bmatrix} \lambda_{100}T_1 & \lambda_{111}T_4 & \lambda_{111}T_6 \\ \lambda_{111}T_4 & \lambda_{100}T_2 & \lambda_{111}T_5 \\ \lambda_{111}T_6 & \lambda_{111}T_5 & \lambda_{100}T_3 \end{bmatrix}, \tag{5.19}$$

as a result of which the energy minimization problem becomes

$$(\mathbf{K} - \overset{k}{\gamma}\,\mathbf{I})\,\overset{k}{\mathbf{m}} = \overset{k}{\mathbf{b}}, \tag{5.20a}$$

$$\overset{k}{\mathbf{m}} \cdot \overset{k}{\mathbf{m}} = 1. \tag{5.20b}$$

In addition, we take the dot product of eq. (5.20a) with $\overset{k}{\mathbf{m}}$, solve for the quadratic term, and using eq. (5.20b), we write

$$\overset{k}{\mathbf{m}} \cdot \mathbf{K}\,\overset{k}{\mathbf{m}} = \overset{k}{\gamma} + \overset{k}{\mathbf{b}} \cdot \overset{k}{\mathbf{m}}, \tag{5.21}$$

which after a uniform shifting of the base energy of those of the entire easy axes simplifies the Gibbs free energy as

$$\overset{k}{G} = \frac{1}{2}\,\overset{k}{\mathbf{m}} \cdot \mathbf{K}\,\overset{k}{\mathbf{m}} - \overset{k}{\mathbf{b}} \cdot \overset{k}{\mathbf{m}} + \overset{k}{K_0} = \frac{1}{2}(\overset{k}{\gamma} - \overset{k}{\mathbf{b}} \cdot \overset{k}{\mathbf{m}}) + \overset{k}{K_0}\,. \tag{5.22}$$

Such simplifications reduce computation time and are crucial when the model is integrated into finite-element constructs, which evaluate the model many times for each solution step. To make the model more robust, an exact solution to the system given by eqs. (5.20a) and (5.20b) is derived as follows. By employing the eigenvalue decomposition, eq. (5.20a) can be rewritten as

$$\begin{aligned}\overset{k}{\mathbf{b}} &= (\mathbf{K}- \overset{k}{\gamma}\, \mathbf{I})\, \overset{k}{\mathbf{m}}= (\mathbf{Q}\boldsymbol{\Lambda}\mathbf{Q}^{\mathrm{T}}- \overset{k}{\gamma}\, \mathbf{I})\, \overset{k}{\mathbf{m}} \\ &= (\mathbf{Q}\boldsymbol{\Lambda}\mathbf{Q}^{\mathrm{T}}- \overset{k}{\gamma}\, \mathbf{Q}\mathbf{Q}^{\mathrm{T}})\, \overset{k}{\mathbf{m}} \\ &= \mathbf{Q}(\boldsymbol{\Lambda}- \overset{k}{\gamma}\, \mathbf{I})\mathbf{Q}^{\mathrm{T}}\, \overset{k}{\mathbf{m}},\end{aligned} \tag{5.23}$$

where $\mathbf{Q}$ is an orthogonal matrix containing the eigenvectors of $\mathbf{K}$, and $\boldsymbol{\Lambda}$ is a diagonal matrix composed of the corresponding eigenvalues, i.e., λ_1-λ_3, of $\mathbf{K}$. Solving eq. (5.23) for $\overset{k}{\mathbf{m}}$ and substituting it into eq. (5.20b), one gets

$$\overset{k}{\mathbf{b}}{}^{\mathrm{T}}\mathbf{Q}(\boldsymbol{\Lambda}- \overset{k}{\gamma}\, \mathbf{I})^{-2}\mathbf{Q}^{\mathrm{T}}\, \overset{k}{\mathbf{b}}= 1. \tag{5.24}$$

The matrix inversion required in the foregoing equation is easily avoided by using the simplification

$$(\boldsymbol{\Lambda}- \overset{k}{\gamma}\, \mathbf{I})^{-n} = \begin{bmatrix} \frac{1}{(\lambda_1-\overset{k}{\gamma})^n} & 0 & 0 \\ 0 & \frac{1}{(\lambda_2-\overset{k}{\gamma})^n} & 0 \\ 0 & 0 & \frac{1}{(\lambda_3-\overset{k}{\gamma})^n} \end{bmatrix}, \quad n \in \mathbb{N}. \tag{5.25}$$

When expanded, eq. (5.24) reduces to the following sixth order polynomial:

$$\begin{aligned} \overset{k}{\bar{\gamma}}{}^{6} + 2(\bar{\lambda}_2 + \bar{\lambda}_3)\, \overset{k}{\bar{\gamma}}{}^{5} + \left(\bar{\lambda}_2^2 + 4\bar{\lambda}_2\bar{\lambda}_3 + \bar{\lambda}_3^2 - \bar{Q}_1 - \bar{Q}_2 - \bar{Q}_3\right) \overset{k}{\bar{\gamma}}{}^{4} \\ +2\left(\bar{\lambda}_2^2\bar{\lambda}_3 + \bar{\lambda}_2\bar{\lambda}_3^2 - \bar{\lambda}_2\bar{Q}_1 - \bar{\lambda}_3\bar{Q}_1 - \bar{\lambda}_3\bar{Q}_2 - \bar{\lambda}_2\bar{Q}_3\right) \overset{k}{\bar{\gamma}}{}^{3} \\ + \left(\bar{\lambda}_2^2\bar{\lambda}_3^2 - \bar{\lambda}_2^2\bar{Q}_1 - 4\bar{\lambda}_2\bar{\lambda}_3\bar{Q}_1 - \bar{\lambda}_3^2\bar{Q}_1 - \bar{\lambda}_3^2\bar{Q}_2 - \bar{\lambda}_2^2\bar{Q}_3\right) \overset{k}{\bar{\gamma}}{}^{2} \\ -2\bar{\lambda}_2\bar{\lambda}_3\bar{Q}_1\left(\bar{\lambda}_2 + \bar{\lambda}_3\right) \overset{k}{\bar{\gamma}} -\bar{\lambda}_2^2\bar{\lambda}_3^2\bar{Q}_1 = 0 \,, \end{aligned} \tag{5.26}$$

where $\overset{k}{\bar{\gamma}}= \lambda_1- \overset{k}{\gamma}$, $\bar{\lambda}_2 = \lambda_2 - \lambda_1$, $\bar{\lambda}_3 = \lambda_3 - \lambda_1$, and $[\sqrt{\bar{Q}_1}; \sqrt{\bar{Q}_2}; \sqrt{\bar{Q}_3}] = \mathbf{Q}^{\mathrm{T}}\, \overset{k}{\mathbf{b}}$. For the kth easy direction, this polynomial can be easily solved to obtain the entire solution set of γ, which is consequently used to calculate a set of magnetization directions after solving eq. (5.23) for $\mathbf{m}$ as

$$\overset{k}{\mathbf{m}} = \mathbf{Q}(\boldsymbol{\Lambda} - \overset{k}{\gamma}\,\mathbf{I})^{-1}\mathbf{Q}^{\mathrm{T}}\,\overset{k}{\mathbf{b}}\,. \tag{5.27}$$

Again, the matrix inversion is easily avoided using eq. (5.25).

Multiplicity of the solution set for $\overset{k}{\mathbf{m}}$

Due to the dimensionality of the problem and the unity norm constraint (5.20b), eq. (5.26) is a sixth order polynomial, giving rise to six possible solutions for $\mathbf{m}$ for each k. The complex solutions of eq. (5.26) can be neglected. Since the expression for G for each k is only valid in the vicinity of the kth easy magnetization direction, the direction solutions oriented sufficiently far from the corresponding easy axis can also be ignored. For example, Figure 5.2 shows the volume of valid magnetization directions about $\overset{-2}{\mathbf{c}} = [0; -1; 0]$. The remaining solutions of eq. (5.26) correspond to valid minima of the local energy function G for each k. Figure 5.3 depicts a surface plot of Gibbs free energy (scaled down by K), showing the real, exact solutions (5.27) and the approximate solution (5.9) of $\mathbf{m}$ for each k. Clearly, the approximate solution does not truly correspond to the Gibbs free energy minimizer.

The proposed modeling framework has the capability of considering all valid solutions of $\mathbf{m}$ for each k; however, the volume fraction of magnetic domains oriented along each minima depends upon the history of stress and magnetic field application as well as thermal activation, which energizes magnetic moments allowing them to overcome the energy barriers between energy minima. Thus, if more than one magnetization direction for each easy direction is considered, the energy weighting expression (5.14) should be modified to incorporate these effects, while ensuring that multiple minima about a single easy direction are not excessively weighted. Following

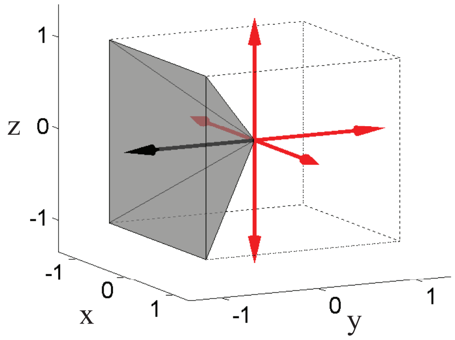

Figure 5.2: Volume of valid magnetization directions (shaded region) for $\overset{-2}{\mathbf{m}}$ in the vicinity of $\overset{-2}{\mathbf{c}} = [0; -1; 0]$ (black arrow), shown in relation to the 5 other easy magnetization directions (red arrows) for a material with cubic anisotropy and $\overset{k}{K} > 0$.

the approach of Evans and Dapino [42], this work strikes a balance between accuracy and efficiency by considering only six magnetization directions. For each easy direction, the solutions for $\mathbf{m}$ are selected using the criteria that each minimizes most the Gibbs free energy within their respective volume of valid magnetization directions.

5.3 Simplification of the Model for Lower Dimensional Applications

Galfenol can be utilized in complex 3D systems, because it can withstand 3D stresses. However, not all applications require Galfenol's 3D capability. For such applications, lower dimensional models are sufficient or are useful for preliminary analysis of the system. In fact, many experiments are conducted on magnetostrictive rods, which are exposed to an axial magnetic field and stress, thus, warranting even a 1D formulation of the proposed model.

While the exact solution procedure presented in Section 5.2 is general and valid for arbitrary applications, a special magnetic field or stress state may reduce the number of locally-minimum energy directions. For such cases, eq. (5.26) degenerates

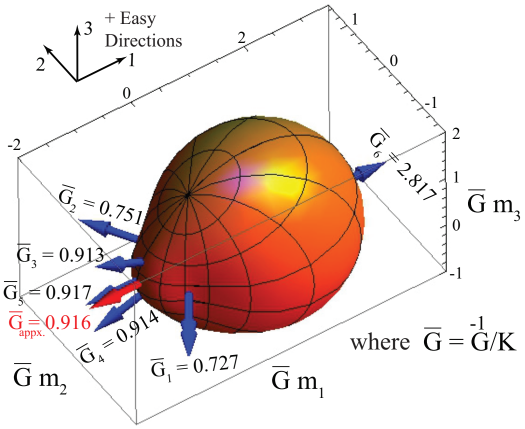

Figure 5.3: The cartesian surface plot of Gibbs free energy (5.1), scaled down by K, relative to the second easy direction $\overset{-1}{\mathbf{c}}$ with $K = 30$ (kJ/m^3), $K_{100} = 0$ (kJ/m^3), $3\lambda_{100} = 520$ (ppm) and $3\lambda_{111} = -20$ (ppm) for $\mathbf{H} = [1; 0; 0]$ (kA/m) and $\mathbf{T} = -[100; 0; 40; 40; 40; 0]$ (MPa); real solutions of eq. (5.27) shown by blue arrows (orientation most minimizing energy by a double-headed arrow); approximate solution (5.9) shown by a red arrow.

into lower order polynomials, which can be solved more efficiently. Two cases are considered: 2D (plane stress) and 1D. Note that the over index k is dropped within subsections that specify its value to improve clarity.

5.3.1 2D Applications

Consider a state of plane stress and planar magnetic field (i.e., $H_3 = T_3 = T_5 = T_6 = 0$). For this case, eq. (5.26) still has six solutions for ± 3 easy directions. However, a simplified approach can be used for the remaining easy directions.

$k = \pm 1, \pm 2$

For the easy crystallographic directions $\pm \langle 100 \rangle$ and $\pm \langle 200 \rangle$, the magnetic force vector (5.3) has one zero component, namely, $b_3 = 0$. From eqs. (5.20), this results in a planar magnetization direction (i.e., $m_3 = 0$) since γ cannot equal 0. The remaining direction components are

$$m_2 = \frac{K_{12}(2m_1^2 - 1) - b_2 m_1}{\hat{K}_{12} m_1 - b_1} = \pm\sqrt{1 - m_1^2}, \tag{5.28}$$

where $K_{11} = -\frac{3}{2}\lambda_{100}T_1$, $K_{12} = -\frac{3}{2}\lambda_{111}T_4$, and $\hat{K}_{12} = -\frac{3}{2}\lambda_{100}(T_1 - T_2)$. Substituting the foregoing result into eq. (5.20b) gives the fourth order polynomial

$$\begin{aligned} (\hat{K}_{12}^2 + 4K_{12}^2)m_1^4 - 2(b_1\hat{K}_{12} + 2b_2K_{12})m_1^3 + (b_1^2 + b_2^2 - \hat{K}_{12}^2 - 4K_{12}^2)m_1^2 \\ +2(b_1\hat{K}_{12} + b_2K_{12})m_1 + K_{12}^2 - b_1^2 = 0. \end{aligned} \tag{5.29}$$

5.3.2 1D Applications

Consider 1D loading along $\pm\langle 100\rangle$, for which the only nonzero stress and field components are T_1 and H_1.

$k = \pm 1$

For the easy crystallographic directions $\pm\langle 100\rangle$, the magnetic force vector (5.3) has components $b_2 = b_3 = 0$, and the system of eqs. (5.20) has the explicit solutions $\overset{1}{\mathbf{m}}=\overset{1}{\mathbf{c}}$ and $\overset{-1}{\mathbf{m}}=\overset{-1}{\mathbf{c}}$, since γ cannot equal 0.

$k = \pm 2, \pm 3$

Magnetic domains tend to orient parallel to magnetic fields and tensile stresses, and perpendicular to compressive stresses. For a 1D application, there is no driving force to rotate the basal plane magnetization directions (i.e., those of $k = \pm 2, \pm 3$) about the loading axis $\pm\langle 100\rangle$. The basal plane directions, therefore, respond equivalently to axial loading; thus, it is sufficient to consider only the case $k = 2$. Solving eq. (5.20a) for m_2 one gets

$$m_2 = \frac{b_2 m_1}{b_1 - K_{11} m_1} = \pm\sqrt{1 - m_1^2}. \tag{5.30}$$

Substitution of the foregoing result into eq. (5.20b) gives

$$K_{11}^2 m_1^4 - 2b_1 K_{11} m_1^3 + \left(b_1^2 + b_2^2 - K_{11}^2\right) m_1^2 + 2b_1 K_{11} m_1 - b_1^2 = 0. \tag{5.31}$$

Unlike the exact solution procedure for 3D inputs, the reduced 1D and 2D models do not require a solution for the intermediate variable γ; rather, the exact minimum energy directions are directly found by solving the corresponding fourth order polynomials. In particular, due to the equivalence of the four basal plane directions for 1D applications, eq. (5.31) must be solved only once. As detailed later, the 1D simplification is over twice as efficient as the proposed 3D model.

5.4 Parameter Optimization

The goal of the parameter optimization procedure is to identify the constant model parameters $\{M_s, E, \lambda_{100}, \lambda_{111}, c_0, K, K_0, \Omega\}$ that provide the best fit of the model to experimental data. With optimized parameters, the model should adequately calculate the magnetization and magnetostriction response for arbitrary input sets (i.e., interpolated within or extrapolated outside the inputs used for experimental validation).

The optimization procedure presented below is dichotomous. First, averaged experimental data is found from 1D hysteretic measurements through an effective averaging technique. Second, a sophisticated objective error function relating the family of simulated responses and the family of averaged data is minimized to determine the optimal material parameters.

5.4.1 Extracting the averaged responses from hysteretic measurements

The aim is to average the upper and lower branches of hysteretic data. Chakrabarti [43] proposed a technique that averages in an incremental sense with a user-defined step size. However, even for a carefully chosen step size, some portions of the averaged curves obtained from this approach may go outside the two hysteretic curves, suggesting that the technique lacks robustness. To alleviate this shortcoming, the following two issues must be addressed. First, for sampled hysteretic actuation and sensing curves, the values of the independent variable for points on the upper and lower branches may not match. To alleviate this, each branch is fit with piecewise linear Hermite functions and re-sampled using the same discretization.

Second, the data in highly-sloped burst regions may need to be treated differently from that in the flat saturation regions. For the former, a major change is observed in the vertical direction, thus, the data should be averaged in the horizontal direction. For the latter, the opposite is true. Accordingly, this switch of the averaging direction is taken into account in the discretization procedure discussed above.

5.4.2 Objective Error Function

MATLAB's built-in constrained optimization function, *fmincon*, is used. This function needs an initial guess and bounds for each parameter, and a globally-defined, scalar objective function. For c_0 and Ω, respectively, 10^{-5} and 1200 were used as start guesses. For the remaining initial guesses, the approximate analytical expressions developed by Chakrabarti [43] were utilized. Furthermore, the bounds for all parameters were selected to be 80% above and below the corresponding initial guesses, except the smoothing factor Ω, for which a range from 0.01 to 3 kJ/m^3 was selected. Finally, the objective function is a weighted average error for an entire family of curves that is constructed as follows.

1. For the ith curve of N_i points in a data set, the modeling error is quantified as

$$error_i = \frac{1}{N_i} \sum_{j=1}^{N_i} \left| w_{ij} \frac{Y_{ij} - X_{ij}}{range(X_i)} \right|^n , \tag{5.32}$$

   where Y_{ij} and X_{ij} are the jth component of the ith calculated response and averaged data, respectively, which contain N_i points; $range(X_i)$ is the difference between the upper and lower bound for that curve; w_{ij} is a weighting factor for each point; n is a positive number, which when taken as 1 gives rise to a 1-norm, and when taken as 2 yields the square of the common Euclidean 2-norm.

2. The data is split into two sub-families: actuation and sensing. The mean error for each sub-family is obtained by averaging the individual errors within the sub-family.

3. The total error is the sum of the two sub-family errors.

Note that the error function definition (5.32) retains the main feature of that from Chakrabarti [43] in that the error is normalized with respect to the range of each curve, allowing for the safe combination of the magnetization and magnetostriction errors. In contrast, the new error function definition generalizes the former definition in two aspects. First, instead of taking n to be 2, n can be any number, or can even be a parameter to be identified through optimization. Our experience suggests that $n = 1$ provides good performance. Second, with the user-defined weighting factors w_{ij}, one can have more control over how much error is attributed to the different regions of the curves. In essence, the error observed in the burst regions dominates that of the saturation regions; thus, the latter error, even if large, does not contribute much to the total error. Therefore, the parameters may be overly optimized for the burst regions. For such cases, a relatively large weighting factor is devised so that the resulting saturation error is comparable to that from the burst regions. We do not report values for the weighting factors, as their determination is done through trial and error and is dependent on the given data.

5.4.3 Some Notes on the Optimization

Finding the globally-optimal parameter set can be time consuming, because the parameter space has eight dimensions. To reduce the computational burden, the following notes may be considered.

- When calculating the averaged data, one may discretize each curve using the same number of points. This allows for N_i to be removed from the error function (5.32).

- For ideal actuation measurements, the magnetization and magnetostriction curves are symmetric with respect to magnetic field. Thus, only half of the actuation data may need to be considered.

- The parameter set may be split into three sets: $\{M_s, E, \lambda_{100}\}$, and $\{c_0, K, K_0, \Omega\}$, and $\{\lambda_{111}\}$. The first set may be directly calculated from sensing and actuation responses (i.e., a preprocessing step), while the second set is found through optimization. For 1D measurements of a $\langle 100 \rangle$-oriented sample, the third set cannot be calculated directly or through optimization, as the 1D model is independent of λ_{111}. In the absence of shear stresses, λ_{111} can be arbitrarily set to zero. In other cases, this parameter must be taken from the literature or measured from 1D measurements of a $\langle 111 \rangle$-oriented sample.

5.5 Validation of the Model: Results and Discussion

The model consists of two parts: the nonhysteretic and hysteretic parts. The former models the averaged hysteretic data, and is governed by eqs. (5.12)-(5.14) and (5.20), while the latter is built on the former, and is defined by eqs. (5.15) and (5.16). Validation of each part is discussed in the subsections below.

Due to the significant difficulty in obtaining 3D measurements, it is common practice to conduct 1D experiments, in which a magnetostrictive rod is exposed to load and magnetic field along its main axis, say $\pm \langle 100 \rangle$ direction. As detailed above, a key benefit of the DEA model is that all but one parameter can be determined from 1D measurements. For validation, existing data obtained by Evans and Dapino [42] is used. The data was obtained using a textured, $\langle 100 \rangle$-oriented $\mathrm{Fe}_{81.5}\mathrm{Ga}_{18.5}$ rod grown with the Free Stand Zone Melt method (FSZM) at Etrema Products Inc.

5.5.1 Validation of the Nonhysteretic Model

The constant parameters $\{M_s, E, \lambda_{100}, \lambda_{111}, c_0, K, K_0, \Omega\}$ must be identified to fully define the nonhysteretic model. The aforementioned measurement data is used to initiate the optimization routine discussed in Section 5.4. The optimized parameters are tabulated in Table 5.1. Figure 5.4 depicts the measured data, together with the extracted averaged curves along with the calculated nonhysteretic model. The figure clearly demonstrates the effectiveness of the averaging technique, and the close agreement between the nonhysteretic model and the averaged hysteretic data. Due to the decoupled optimization procedure (namely, the calculated effective elastic modulus and saturation magnetization and magnetostriction), excellent fits are obtained in the saturation regimes.

Common to all subfigures of Figure 5.4, the model underestimates both magneti-

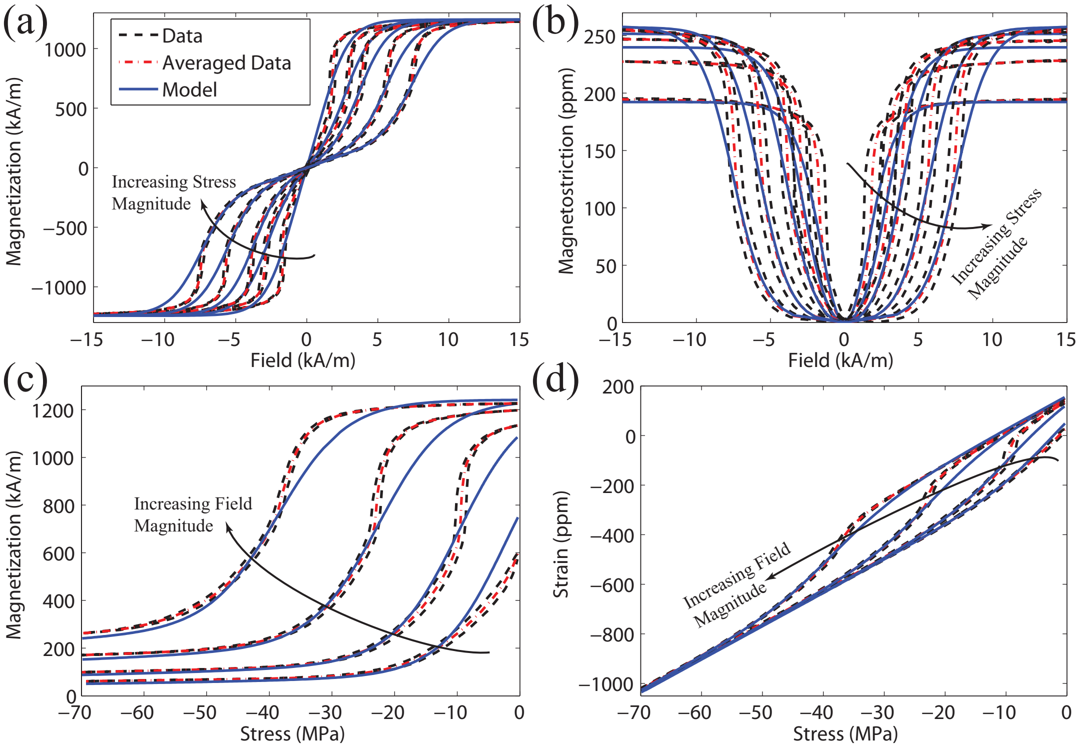

Figure 5.4: Comparison of averaged hysteretic measurements and nonhysteretic model for ⟨100⟩ $Fe_{81.5}Ga_{18.5}$ grown with FSZM at (a),(b) constant compressive stress values of 0.32, 8.00, 13.40, 23.10, and 32.30 MPa, and (c),(d) constant field values of 1.85, 3.24, 5.65, and 8.88 kA/m. Strain is the superposition of the mechanical strain (T/E) and the magnetostriction (λ).

Table 5.1: Optimized parameters for the nonhysteretic model.

Par.	M_s (kA/m)	E (GPa)	λ_{100} (ppm)	λ_{111} (ppm)
Value	1,242.20	74.49	172.31	–

Par.	c_0	K (kJ/m^3)	K_{100} (J/m^3)	Ω (J)
Value	0.38	35.58	412.18	1,330.00

zation and magnetostriction as the material leaves the burst region and approaches saturation. For instance, in Subfigure 5.4(a) for the 32.3 MPa bias stress, the model starts to deviate from the averaged data near 7.3 kA/m and exhibits a maximum relative error of 19% at 8.2 kA/m before tending to zero as it saturates around 11 kA/m. This consistent lack of agreement over all subfigures suggests that some of the underlying physics are not captured by the local free energy formulation (5.22). Improvements to this energy will be the subject of future research.

Table 5.2 compares the normalized error of the proposed model and the approximate model [42, 43] for magnetization and strain for actuation and sensing cases. The error was calculated according to Subsection 5.4.2 with all the weighting factors set to one. The number of uniformly-distributed samples was increased until the error was unchanged. The table demonstrates that the total error of the new model is extremely low, i.e., only 9.3% of that of the approximate model.

Table 5.2: Comparison of the normalized error of the exact and approximate nonhysteretic models. Model parameters for the latter are: $M_s = 1,225.00$ (kA/m), $E = 75.31$ (GPa), $\lambda_{100} = 166.31$ (ppm), $K = 34.84$ (kJ/m^3), $K_{100} = 498.00$ (J/m^3), and $\Omega = 1,014.70$ (J).

Model	Actuation error		Sensing error		Total error
	M	S	M	S	
Exact	0.04	0.06	0.09	0.09	0.28
Approximate	0.04	0.05	0.08	2.84	3.01

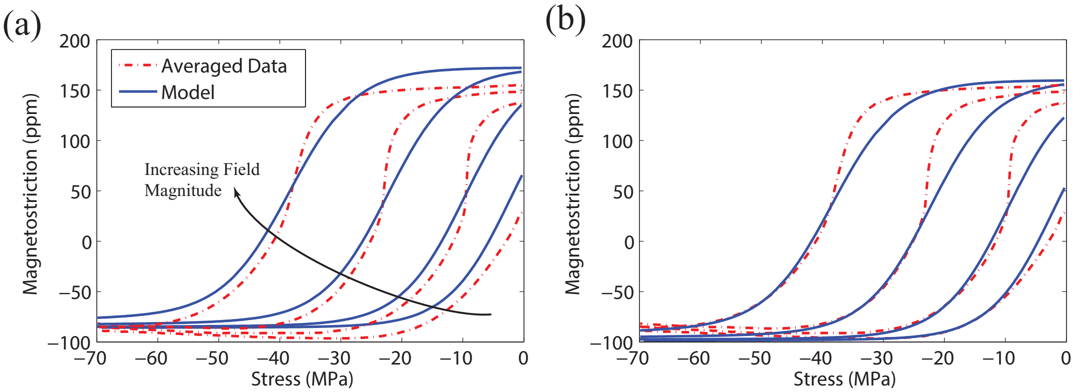

Figure 5.5: Magnetostriction calculated with (a) eq. (5.7) and (b) eq. (5.17), and compared with the averaged hysteretic data at constant field values of 1.85, 3.24, 5.65, and 8.88 kA/m. For each case, material parameters are optimized for the full family of actuation and sensing measurements using identical objective error functions.

The major error of the approximate model for the sensing case originates from the magnetostriction equation, given by eq. (5.7), which is replaced by eq. (5.17) in the proposed model. Figure 5.5 illustrates the effectiveness of incorporating the magnetostriction constant c_0 by comparing averaged hysteretic data to simulations that use the current and previous magnetostriction expressions: eqs. (5.17) and (5.7), respectively. Since the stiffness moduli c_{11} and c_{12} are positive, c_0 is also positive. Consequently, the magnetostriction obtained from the prior formulation exceeds that from the current expression, which provides a better fit to the data. Furthermore, even though the constant c_0 appears to take part only in the calculation of the strain–stress sensing curves, the improved fitting accuracy, as shown in Subfigure 5.5(b), leads to a reduced total objective error value, thus, improving the overall optimization procedure as demonstrated in Table 5.2.

5.5.2 Computational Efficiency

The analysis of an algorithm primarily concerns its computation time [80]. For modeling the macroscopic behavior of cubic magnetostrictive materials, the approximate formulation of the DEA model developed by Evans and Dapino [42] currently has the best combination of speed and accuracy. Since the same hysteresis model is used for the current (exact) and prior (approximate) works, the computational speed of the nonhysteretic models are compared. For the approximate model, optimized material parameters were obtained from Chakrabarti [43], while for the exact model, the optimized properties given in Table 5.1 were used.

To incorporate any effect of the input parameters on computation time, the input parameters were varied for each execution using quasi-random sampling; thus, the *expected* execution time was determined by simulating each model a large number of times and dividing by the number of executions [80]. Components of the input were sampled from the nine-dimensional parameter space (three for $\mathbf{H}$, and six for $\mathbf{T}$) using a Sobol' quasi-random (QR) sequence [81], which are commonly used in sensitivity analysis [82]. QR sequences generate points in the unit hypercube more uniformly than sequences of random numbers, thereby minimizing the number of samples required to form a representative sample of the parameter space. The Sobol' QR sequence is scaled such that $-70 \leq H_j \leq 70$ kA/m and $-250 \leq T_i \leq 250$ MPa, with the constraint that if a sampled stress state corresponds to a von Mises stress larger than 400 MPa, it is discarded.

The models were coded as compiled MATLAB functions and executed on two computers. Since the performance of the 2D version of the exact model is bounded by that of the 1D and 3D versions, only the averaged results for 1D and 3D formulations of the models are shown in Figure 5.6. While the exact model is slightly faster than the approximate model for 1D inputs, it is slower than the approximate model for 3D

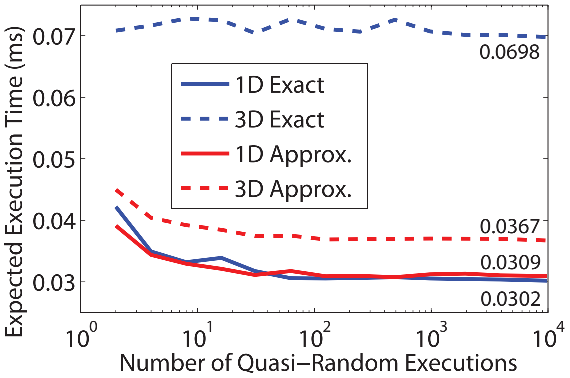

Figure 5.6: Expected execution time (averaged over 2 computers) of the exact and approximate constitutive models (coded as compiled MATLAB functions).

inputs, requiring about 1.9 times the CPU time. This is to be expected, due to the multiplicity of the solution set for $\mathbf{m}$, which requires more computation. Nonetheless, the exact model is more accurate and defined for all inputs, which is crucial for implementation in black-box finite-element models. Additionally, results of the next chapter on the material Jacobian and Hessian derived from the exact model reveal that material derivatives are significantly simplified relative to those derived from the approximate model. This suggests that the exact model may be faster than the approximate model for 3D system-level modeling, which requires the Jacobian and/or Hessian for inversion of the constitutive model and calculation of Galfenol's stiffness and sensitivities. This last feature with relevant applications will be discussed in the following chapters.

5.5.3 Validation of the Hysteretic Model

By employing the optimization routine developed in Section 5.4, the hysteretic model parameters $\{c, k_p\}$ are determined and listed in Table 5.3. Figure 5.7 compares the hysteretic model against the measured data. As illustrated, the hysteretic model is in close agreement with the data.

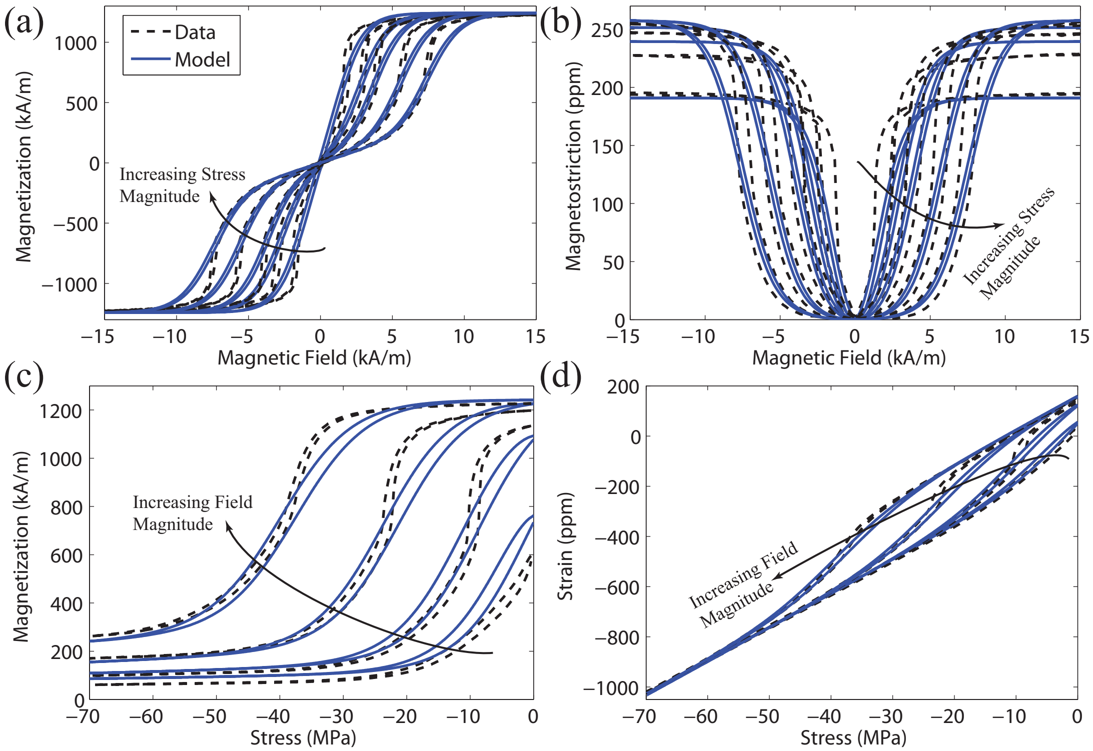

Figure 5.7: Comparison of hysteretic measurements and hysteretic model for $\langle 100 \rangle$ Fe$_{81.5}$Ga$_{18.5}$ grown with FSZM at (a),(b) constant compressive stress values of 0.32, 8.00, 13.40, 23.10, and 32.30 MPa, and (c),(d) constant field values of 1.85, 3.24, 5.65, and 8.88 kA/m. Strain is the superposition of the mechanical strain (T/E) and the magnetostriction (λ).

Table 5.3: Optimized parameters for the hysteretic model.

Parameter	c	k_p (J)
Optimized value	0.2	430.0

The performance of the hysteretic model hinges on two sources. First, the averaged curves underlie the hysteresis model. Thus, errors in the calculation of the averaged curves (i.e., in the nonhysteretic model) will propagate to the hysteretic response. For instance, the saturation regimes of the curves corresponding to a compressive stress of 8.00 MPa in Figures 5.7(b) and 5.4(b) appear to have the same error. This illustrates the benefit to improving the nonhysteretic model.

The second source is how to control the width of the hysteresis, which, as per Evans and Dapino [42], is done through the employment of the parameters c and k_p. Ideally, to get the hysteretic curves from the proposed nonhysteretic model, the hysteretic model must apply a symmetric shift about the averaged curve obtained from the nonhysteretic model. However, there is no guarantee that the current hysteretic model does so. For example, consider the curve corresponding to a bias field of 1.85 kA/m in Figure 5.4(c), for which the nonhysteretic model accurately predicts the lower saturation magnetization. In this region, the hysteretic model should have a negligible effect, as demonstrated in Figure 5.7(c). However, the hysteretic model shifts the response away from the accurately calculated averaged curve. In addition, the hysteretic model overestimates the hysteresis width for sensing cases (5.7(c) and (d)), but underestimates it for actuation cases (5.7(a) and (b)). These problems suggest that the parameters c and k_p control more than just the hysteresis width. The development of a hysteresis model that overcomes these issues is left for future research.

5.6 Summary and Conclusions

Several improvements were proposed for the Discrete Energy-Averaged model, which calculates the 3D hysteretic magnetization and magnetostriction of iron-gallium alloys. In particular, the magnetoelastic energy was enhanced through the utilization of the more thorough expression of the magnetostriction tensor, and the Gibbs free energy was simplified through the reduction of the magnetic stiffness matrix. An analytical solution procedure based on an eigenvalue decomposition was then presented. It was shown that the exact solution procedure offers multiple (up to the number of easy directions) local minimum energy directions for each individual easy direction. These additional minima provide two advantages. First, the singularities that are present in the existing approximate solution are avoided. Second, the material's complex response to arbitrary stress and magnetic field inputs can be better understood.

The resulting robustness comes at an expense. For general loadings, the model requires the solution of six 6th order polynomials. As a result, the exact solution procedure is about two times slower than the approximate procedure for 3D applications. However, analytical reductions of the model were presented for 2D and 1D applications. In the simplest case (i.e., 1D applications), only a single 4th order polynomial must be solved, thus, making the exact solution procedure as efficient as the approximate procedure.

Another novelty is in finding the model parameters. Rather than employing anhysteretic curves, our approach utilizes the average of the hysteretic data, which obviates taking additional measurements. A novel optimization routine was developed that retains the number of model constants, but decouples the parameters into exclusive sets. Consequently, the set $\{M_s, E, \lambda_{100}\}$ was found efficiently and accurately through a preprocessing step, which fits the magnetization and magnetostriction saturation regimes with lines. Only the remaining parameters were estimated through a global optimization procedure that used a sophisticated objective error function. The effectiveness of the model was verified through comparison with existing measurement data. The hysteretic model has two sources of error: the nonhysteretic model and the hysteresis formulation itself. Even though the nonhysteretic model closely agreed with the averaged hysteretic data, the observed error propagated to the hysteretic simulations. Additionally, the parameters of the hysteretic model, which were previously thought to control only the hysteresis width, appeared to introduce unexpected error. For instance, the hysteresis model added error to the nonhysteretic magnetization response in the lower saturation region, where the hysteresis effects should have been negligible. Further research is required to develop a hysteresis model that avoids these issues.

Chapter 6
Derivative terms for the direct model for Galfenol

In magnetostrictive actuators, magnetic field and stress inputs generate magnetic flux density and strain. In this dissertation, the constitutive models that follow this scheme are referred to as *direct* models. However, in certain design and control situations, inverse models are necessary in which the magnetic field and stress are found from specified magnetic flux density and strain. This inversion typically involves an iterative procedure, and requires Jacobian and/or Hessian derivative terms of the direct model. Note that Jacobian and Hessian are the matrices of, respectively, the first and second order derivative terms.

This chapter presents analytical derivation of the Jacobian and Hessian derivative terms (in indicial notation) for the Galfenol direct model presented in the previous chapter. The results are collectively documented in Refs. [45, 46], and will be utilized in the following chapters.

6.1 Derivative terms for the direct model, given in Chapter 5

The macroscopic 3D magnetic flux density and strain vectors are defined as weighted sums of the response due to the r minimum energy directions as

$$\mathbf{B}=\mu_0(\mathbf{H}+\overline{\mathbf{M}})=\mu_0(\mathbf{H}+M_s\sum_{k=\pm1}^{\pm r/2}\overset{k}{\overline{\xi}}_{hys}\overset{k}{\mathbf{m}}), \tag{6.1}$$

$$\mathbf{S}=\mathbf{s}\mathbf{T}+\overline{\boldsymbol{\lambda}}=\mathbf{s}\mathbf{T}+\sum_{k=\pm1}^{\pm r/2}\overset{k}{\overline{\xi}}_{hys}\overset{k}{\boldsymbol{\lambda}}, \tag{6.2}$$

where $\mathbf{s}$ stands for the 6×6 mechanical compliance matrix, and the remaining terms were defined in the previous chapter. The first and second order derivatives of the foregoing equations with respect to magnetic field and stress are derived in the following.

First, we rewrite the Gibbs free energy given by eq. (5.22) as

$$\overset{k}{G}=\frac{1}{2}\overset{k}{\mathbf{m}}\cdot\mathbf{K}\overset{k}{\mathbf{m}}-(K\overset{k}{\mathbf{c}}+\mu_0M_s\mathbf{H})\cdot\overset{k}{\mathbf{m}}+\overset{k}{K}_0+\frac{3}{2}c_0\lambda_{100}\ tr(\mathbf{T}),\quad k\in\pm\{1,\ldots,\frac{r}{2}\}, \tag{6.3}$$

which leaves the direct model unchanged, as we are shifting the base energy of all of the easy axes the same amount. Let the subscripts $p,q\in\{1,\ldots,3\}$ and $i,j\in\{1,\ldots,6\}$. Differentiating the foregoing equation with respect to field and stress gives

$$
\begin{aligned}
\frac{\partial \overset{k}{G}}{\partial H_p} &= \frac{\partial \overset{k}{\mathbf{m}}}{\partial H_p} \cdot \mathbf{K} \overset{k}{\mathbf{m}} - \mu_0 M_s m_p - (K \overset{k}{\mathbf{c}} + \mu_0 M_s \mathbf{H}) \cdot \frac{\partial \overset{k}{\mathbf{m}}}{\partial H_p} \\
&= \frac{\partial \overset{k}{\mathbf{m}}}{\partial H_p} \cdot (\mathbf{K} \overset{k}{\mathbf{m}} - K \overset{k}{\mathbf{c}} - \mu_0 M_s \mathbf{H}) - \mu_0 M_s m_p \\
&= \overset{k}{\gamma} \frac{\partial \overset{k}{\mathbf{m}}}{\partial H_p} \cdot \overset{k}{\mathbf{m}} - \mu_0 M_s m_p = -\mu_0 M_s m_p,
\end{aligned}
\tag{6.4}
$$

and

$$
\begin{aligned}
\frac{\partial \overset{k}{G}}{\partial T_i} &= \frac{\partial \overset{k}{\mathbf{m}}}{\partial T_i} \cdot \mathbf{K} \overset{k}{\mathbf{m}} + \frac{1}{2} \overset{k}{\mathbf{m}} \cdot \frac{\partial \mathbf{K}}{\partial T_i} \overset{k}{\mathbf{m}} - \frac{\partial \overset{k}{\mathbf{m}}}{\partial T_i} \cdot (K \overset{k}{\mathbf{c}} + \mu_0 M_s \mathbf{H}) \\
&\qquad + \frac{3}{2} c_0 \lambda_{100} \frac{\partial tr(\mathbf{T})}{\partial T_i} \\
&= \frac{\partial \overset{k}{\mathbf{m}}}{\partial T_i} \cdot \mathbf{K} \overset{k}{\mathbf{m}} + \frac{1}{2} \overset{k}{\mathbf{m}} \cdot \frac{\partial \mathbf{K}}{\partial T_i} \overset{k}{\mathbf{m}} - \frac{\partial \overset{k}{\mathbf{m}}}{\partial T_i} \cdot (\mathbf{K} - \overset{k}{\gamma} \mathbf{I}) \overset{k}{\mathbf{m}} \\
&\qquad + \frac{3}{2} c_0 \lambda_{100} \frac{\partial tr(\mathbf{T})}{\partial T_i} \\
&= \frac{1}{2} \overset{k}{\mathbf{m}} \cdot \frac{\partial \mathbf{K}}{\partial T_i} \overset{k}{\mathbf{m}} + \frac{3}{2} c_0 \lambda_{100} \frac{\partial tr(\mathbf{T})}{\partial T_i} \\
&= - \left\{ \begin{array}{ll} \frac{3}{2} \lambda_{100} (m_i^k m_i^k - c_0), & i \in \{1,2,3\} \\ 3\lambda_{111} \overset{k}{m}_1 \overset{k}{m}_2, & i = 4 \\ 3\lambda_{111} \overset{k}{m}_2 \overset{k}{m}_3, & i = 5 \\ 3\lambda_{111} \overset{k}{m}_3 \overset{k}{m}_1, & i = 6 \end{array} \right\} = - \overset{k}{\lambda}_i,
\end{aligned}
\tag{6.5}
$$

where we use the identities

$$
\begin{aligned}
\frac{\partial \overset{k}{\mathbf{m}}}{\partial H_p} \cdot \overset{k}{\mathbf{m}} &= 0, \\
\frac{\partial \overset{k}{\mathbf{m}}}{\partial T_i} \cdot \overset{k}{\mathbf{m}} &= 0,
\end{aligned}
$$

which originate from differentiating eq. (5.20b) with respect to field and stress. These derivatives have major roles in the analytical reduction of the derivative terms given as follows.

6.1.1 Jacobian terms

The Jacobian terms can be obtained from differentiating eqs. (6.1) and (6.2) with respect to H_p and T_i as

$$\frac{\partial \mathbf{B}}{\partial H_p} = \mu_0 \overset{p}{\mathbf{e}} + \mu_0 M_s \sum_{k=\pm 1}^{\pm r/2} \left(\frac{\partial \overset{k}{\bar{\xi}}_{hys}}{\partial H_p} \overset{k}{\mathbf{m}} + \overset{k}{\bar{\xi}}_{hys} \frac{\partial \overset{k}{\mathbf{m}}}{\partial H_p} \right), \tag{6.6a}$$

$$\frac{\partial \mathbf{B}}{\partial T_i} = \mu_0 M_s \sum_{k=\pm 1}^{\pm r/2} \left(\frac{\partial \overset{k}{\bar{\xi}}_{hys}}{\partial T_i} \overset{k}{\mathbf{m}} + \overset{k}{\bar{\xi}}_{hys} \frac{\partial \overset{k}{\mathbf{m}}}{\partial T_i} \right), \tag{6.6b}$$

and

$$\frac{\partial \mathbf{S}}{\partial H_p} = \sum_{k=\pm 1}^{\pm r/2} \frac{\partial \overset{k}{\bar{\xi}}_{hys}}{\partial H_p} \overset{k}{\boldsymbol{\lambda}} + \sum_{k=\pm 1}^{\pm r/2} \overset{k}{\bar{\xi}}_{hys} \frac{\partial \overset{k}{\boldsymbol{\lambda}}}{\partial H_p}, \tag{6.7a}$$

$$\frac{\partial \mathbf{S}}{\partial T_i} = \mathbf{s} \overset{i}{\mathbf{e}} + \sum_{k=\pm 1}^{\pm r/2} \frac{\partial \overset{k}{\bar{\xi}}_{hys}}{\partial T_i} \overset{k}{\boldsymbol{\lambda}} + \sum_{k=\pm 1}^{\pm r/2} \overset{k}{\bar{\xi}}_{hys} \frac{\partial \overset{k}{\boldsymbol{\lambda}}}{\partial T_i}, \tag{6.7b}$$

where $\overset{p}{\mathbf{e}}$ and $\overset{i}{\mathbf{e}}$ are, respectively, 3- and 6-dimensional unit vectors with one as their p^{th} and i^{th} components.

The derivatives of the averaged hysteretic volume fractions occurring in eqs. (6.6) and (6.7) are found upon differentiating eq. (5.14) with respect to field and stress, respectively, and simplifying the results as

$$\frac{\partial \overset{k}{\overline{\xi}}_{hys}}{\partial H_p} = \frac{\mu_0}{\Omega} \overset{k}{\xi}_{hys} \left(M_s \overset{k}{m}_p - \overline{M}_p \right), \tag{6.8a}$$

$$\frac{\partial \overset{k}{\overline{\xi}}_{hys}}{\partial T_i} = \frac{1}{\Omega} \overset{k}{\xi}_{hys} \left(\overset{k}{\lambda}_i - \overline{\lambda}_i \right). \tag{6.8b}$$

The remaining derivative terms in eq. (6.6) can be obtained by differentiating the inhomogeneous eigenvalue (5.20) with respect to field and stress, and solving the resulting equations as

$$\frac{\partial \overset{k}{\mathbf{m}}}{\partial H_p} = [\mathbf{K} - \overset{k}{\gamma} \mathbf{I}]^{-1} \left(\frac{\partial \overset{k}{\gamma}}{\partial H_p} \overset{k}{\mathbf{m}} + \mu_0 M_s \overset{p}{\mathbf{e}} \right), \tag{6.9a}$$

$$\frac{\partial \overset{k}{\mathbf{m}}}{\partial T_i} = [\mathbf{K} - \overset{k}{\gamma} \mathbf{I}]^{-1} \left(\frac{\partial \overset{k}{\gamma}}{\partial T_i} \overset{k}{\mathbf{m}} - \frac{\partial \mathbf{K}}{\partial T_i} \overset{k}{\mathbf{m}} \right), \tag{6.9b}$$

where

$$\frac{\partial \overset{k}{\gamma}}{\partial H_p} = -\mu_0 M_s \frac{\overset{p}{\mathbf{e}} \cdot [\mathbf{K} - \overset{k}{\gamma} \mathbf{I}]^{-1} \overset{k}{\mathbf{m}}}{\overset{k}{\mathbf{m}} \cdot [\mathbf{K} - \overset{k}{\gamma} \mathbf{I}]^{-1} \overset{k}{\mathbf{m}}}, \tag{6.10a}$$

$$\frac{\partial \overset{k}{\gamma}}{\partial T_i} = \frac{\frac{\partial \mathbf{K}}{\partial T_i} \overset{k}{\mathbf{m}} \cdot [\mathbf{K} - \overset{k}{\gamma} \mathbf{I}]^{-1} \overset{k}{\mathbf{m}}}{\overset{k}{\mathbf{m}} \cdot [\mathbf{K} - \overset{k}{\gamma} \mathbf{I}]^{-1} \overset{k}{\mathbf{m}}}. \tag{6.10b}$$

Following a simplification procedure, the foregoing results can be combined as

$$\frac{\partial \overset{k}{\mathbf{m}}}{\partial H_p} = -\mu_0 M_s \overset{k}{\Gamma} \overset{k}{\mathbf{m}} \times \left[[\mathbf{K} - \overset{k}{\gamma} \mathbf{I}] (\overset{k}{\mathbf{m}} \times \overset{p}{\mathbf{e}}) \right], \tag{6.11a}$$

$$\frac{\partial \overset{k}{\mathbf{m}}}{\partial T_i} = \overset{k}{\Gamma} \overset{k}{\mathbf{m}} \times \left[[\mathbf{K} - \overset{k}{\gamma} \mathbf{I}] (\overset{k}{\mathbf{m}} \times \frac{\partial \mathbf{K}}{\partial T_i} \overset{k}{\mathbf{m}}) \right], \tag{6.11b}$$

where

$$\overset{k}{\Gamma} = \frac{|\mathbf{K} - \overset{k}{\gamma}\,\mathbf{I}|^{-1}}{\overset{k}{\mathbf{m}} \cdot [\mathbf{K} - \overset{k}{\gamma}\,\mathbf{I}]^{-1}\,\overset{k}{\mathbf{m}}}.$$

Finally, the remaining derivative terms in eq. (6.7) can be obtained by differentiating eq. (5.17) with respect to field and stress as

$$\begin{aligned}
\frac{\partial \overset{k}{\lambda}_{uu}}{\partial H_p} &= 3\lambda_{100}\, \overset{k}{m}_u \frac{\partial \overset{k}{m}_u}{\partial H_p}, \\
\frac{\partial \overset{k}{\lambda}_{uv}}{\partial H_p} &= 3\lambda_{111} \left(\overset{k}{m}_u \frac{\partial \overset{k}{m}_v}{\partial H_p} + \overset{k}{m}_v \frac{\partial \overset{k}{m}_u}{\partial H_p} \right), \quad u \neq v, \qquad (6.12a) \\
\frac{\partial \overset{k}{\lambda}_{uu}}{\partial T_i} &= 3\lambda_{100}\, \overset{k}{m}_u \frac{\partial \overset{k}{m}_u}{\partial T_i}, \\
\frac{\partial \overset{k}{\lambda}_{uv}}{\partial T_i} &= 3\lambda_{111} \left(\overset{k}{m}_u \frac{\partial \overset{k}{m}_v}{\partial T_i} + \overset{k}{m}_v \frac{\partial \overset{k}{m}_u}{\partial T_i} \right), \quad u \neq v. \qquad (6.12b)
\end{aligned}$$

6.1.2 Hessian terms

The Hessian terms can be obtained from differentiating eq. (6.6) with respect to H_p and T_i as

$$\frac{\partial^2 \mathbf{B}}{\partial H_p \partial H_q} = \mu_0 M_s \sum_{k=\pm 1}^{\pm r/2} \left(\frac{\partial^2 \overset{k}{\bar{\xi}}_{hys}}{\partial H_p \partial H_q} \overset{k}{\mathbf{m}} + \frac{\partial \overset{k}{\bar{\xi}}_{hys}}{\partial H_p} \frac{\partial \overset{k}{\mathbf{m}}}{\partial H_q} + \overset{k}{\bar{\xi}}_{hys} \frac{\partial^2 \overset{k}{\mathbf{m}}}{\partial H_p \partial H_q} + \frac{\partial \overset{k}{\bar{\xi}}_{hys}}{\partial H_q} \frac{\partial \overset{k}{\mathbf{m}}}{\partial H_p} \right), \qquad (6.13)$$

$$\frac{\partial^2 \mathbf{B}}{\partial T_i \partial T_j} = \mu_0 M_s \sum_{k=\pm 1}^{\pm r/2} \left(\frac{\partial^2 \overset{k}{\bar{\xi}}_{hys}}{\partial T_i \partial T_j} \overset{k}{\mathbf{m}} + \frac{\partial \overset{k}{\bar{\xi}}_{hys}}{\partial T_i} \frac{\partial \overset{k}{\mathbf{m}}}{\partial T_j} + \overset{k}{\bar{\xi}}_{hys} \frac{\partial^2 \overset{k}{\mathbf{m}}}{\partial T_i \partial T_j} + \frac{\partial \overset{k}{\bar{\xi}}_{hys}}{\partial T_j} \frac{\partial \overset{k}{\mathbf{m}}}{\partial T_i} \right), \qquad (6.14)$$

and

$$\frac{\partial^2 \mathbf{B}}{\partial H_p \partial T_i} = \mu_0 M_s \sum_{k=\pm 1}^{\pm r/2} \left(\frac{\partial^2 \overset{k}{\overline{\xi}}_{hys}}{\partial H_p \partial T_i} \overset{k}{\mathbf{m}} + \frac{\partial \overset{k}{\overline{\xi}}_{hys}}{\partial H_p} \frac{\partial \overset{k}{\mathbf{m}}}{\partial T_i} + \overset{k}{\overline{\xi}}_{hys} \frac{\partial^2 \overset{k}{\mathbf{m}}}{\partial H_p \partial T_i} + \frac{\partial \overset{k}{\overline{\xi}}_{hys}}{\partial T_i} \frac{\partial \overset{k}{\mathbf{m}}}{\partial H_p} \right), \tag{6.15}$$

and differentiating eq. (6.7) with respect to H_p and T_i as

$$\frac{\partial^2 \mathbf{S}}{\partial H_p \partial H_q} = \sum_{k=\pm 1}^{\pm r/2} \left(\frac{\partial^2 \overset{k}{\overline{\xi}}_{hys}}{\partial H_p \partial H_q} \overset{k}{\boldsymbol{\lambda}} + \frac{\partial \overset{k}{\overline{\xi}}_{hys}}{\partial H_p} \frac{\partial \overset{k}{\boldsymbol{\lambda}}}{\partial H_q} + \overset{k}{\overline{\xi}}_{hys} \frac{\partial^2 \overset{k}{\boldsymbol{\lambda}}}{\partial H_p \partial H_q} + \frac{\partial \overset{k}{\overline{\xi}}_{hys}}{\partial H_q} \frac{\partial \overset{k}{\boldsymbol{\lambda}}}{\partial H_p} \right), \tag{6.16}$$

$$\frac{\partial^2 \mathbf{S}}{\partial T_i \partial T_j} = \sum_{k=\pm 1}^{\pm r/2} \left(\frac{\partial^2 \overset{k}{\overline{\xi}}_{hys}}{\partial T_i \partial T_j} \overset{k}{\boldsymbol{\lambda}} + \frac{\partial \overset{k}{\overline{\xi}}_{hys}}{\partial T_i} \frac{\partial \overset{k}{\boldsymbol{\lambda}}}{\partial T_j} + \overset{k}{\overline{\xi}}_{hys} \frac{\partial^2 \overset{k}{\boldsymbol{\lambda}}}{\partial T_i \partial T_j} + \frac{\partial \overset{k}{\overline{\xi}}_{hys}}{\partial T_j} \frac{\partial \overset{k}{\boldsymbol{\lambda}}}{\partial T_i} \right), \tag{6.17}$$

and

$$\frac{\partial^2 \mathbf{S}}{\partial H_p \partial T_i} = \sum_{k=\pm 1}^{\pm r/2} \left(\frac{\partial^2 \overset{k}{\overline{\xi}}_{hys}}{\partial H_p \partial T_i} \overset{k}{\boldsymbol{\lambda}} + \frac{\partial \overset{k}{\overline{\xi}}_{hys}}{\partial H_p} \frac{\partial \overset{k}{\boldsymbol{\lambda}}}{\partial T_i} + \overset{k}{\overline{\xi}}_{hys} \frac{\partial^2 \overset{k}{\boldsymbol{\lambda}}}{\partial H_p \partial T_i} + \frac{\partial \overset{k}{\overline{\xi}}_{hys}}{\partial T_i} \frac{\partial \overset{k}{\boldsymbol{\lambda}}}{\partial H_p} \right). \tag{6.18}$$

The second order derivatives of the averaged hysteretic volume fractions in the foregoing equations may be obtained from differentiating eq. (6.8) with respect to field and stress as

$$\begin{aligned} \frac{\partial^2 \overset{k}{\overline{\xi}}_{hys}}{\partial H_p \partial H_q} =& \frac{\mu_0}{\Omega} \left(\frac{\partial \overset{k}{\overline{\xi}}_{hys}}{\partial H_q} \left(M_s \overset{k}{m}_p - \overline{M}_p \right) + M_s \overset{k}{\overline{\xi}}_{hys} \frac{\partial \overset{k}{m}_p}{\partial H_q} \right) \\ & - \frac{\mu_0 M_s}{\Omega} \overset{k}{\overline{\xi}}_{hys} \sum_{n=\pm 1}^{\pm r/2} \left(\frac{\partial \overset{n}{\overline{\xi}}_{hys}}{\partial H_q} \overset{n}{m}_p + \overset{n}{\overline{\xi}}_{hys} \frac{\partial \overset{n}{m}_p}{\partial H_q} \right), \end{aligned} \tag{6.19}$$

$$\frac{\partial^2 \overset{k}{\overline{\xi}}_{hys}}{\partial T_i \partial T_j} = \frac{1}{\Omega}\left(\frac{\partial \overset{k}{\overline{\xi}}_{hys}}{\partial T_j}\left(\overset{k}{\lambda}_i - \overline{\lambda}_i\right) + \overset{k}{\overline{\xi}}_{hys}\frac{\partial \overset{k}{\lambda}_i}{\partial T_j}\right) - \frac{1}{\Omega}\overset{k}{\overline{\xi}}_{hys}\sum_{n=\pm 1}^{\pm r/2}\left(\frac{\partial \overset{n}{\overline{\xi}}_{hys}}{\partial T_j}\overset{n}{\lambda}_i + \overset{n}{\overline{\xi}}_{hys}\frac{\partial \overset{n}{\lambda}_i}{\partial T_j}\right), \tag{6.20}$$

and

$$\begin{aligned}\frac{\partial^2 \overset{k}{\overline{\xi}}_{hys}}{\partial H_p \partial T_i} =& \frac{\mu_0}{\Omega}\left(\frac{\partial \overset{k}{\overline{\xi}}_{hys}}{\partial T_i}\left(M_s \overset{k}{m}_p - \overline{M}_p\right) + M_s \overset{k}{\overline{\xi}}_{hys}\frac{\partial \overset{k}{m}_p}{\partial T_i}\right) \\ &- \frac{\mu_0 M_s}{\Omega}\overset{k}{\overline{\xi}}_{hys}\sum_{n=\pm 1}^{\pm r/2}\left(\frac{\partial \overset{n}{\overline{\xi}}_{hys}}{\partial T_i}\overset{n}{m}_p + \overset{n}{\overline{\xi}}_{hys}\frac{\partial \overset{n}{m}_p}{\partial T_i}\right).\end{aligned} \tag{6.21}$$

To obtain a most simplified version of the remaining second order derivative terms in eqs. (6.13)-(6.15), we differentiate the inhomogeneous eigenvalue problem (5.20) twice with respect to field and stress, and solve the resulting equations for the emerging intermediate unknowns, and after a detailed simplification procedure, we finally have

$$\begin{aligned}\frac{\partial^2 \overset{k}{\mathbf{m}}}{\partial H_p \partial H_q} =& -\overset{k}{\Gamma}\ |\mathbf{K} - \overset{k}{\gamma}\,\mathbf{I}|\left(\frac{\partial \overset{k}{\mathbf{m}}}{\partial H_p}\cdot\frac{\partial \overset{k}{\mathbf{m}}}{\partial H_q}\right)[\mathbf{K} - \overset{k}{\gamma}\,\mathbf{I}]^{-1}\,\overset{k}{\mathbf{m}} \\ &- \overset{k}{\Gamma}\,\overset{k}{\mathbf{m}} \times [\mathbf{K} - \overset{k}{\gamma}\,\mathbf{I}]\left(\overset{k}{\mathbf{m}} \times \left[\frac{\partial \overset{k}{\gamma}}{\partial H_p}\frac{\partial \overset{k}{\mathbf{m}}}{\partial H_q} + \frac{\partial \overset{k}{\gamma}}{\partial H_q}\frac{\partial \overset{k}{\mathbf{m}}}{\partial H_p}\right]\right),\end{aligned} \tag{6.22}$$

$$\begin{aligned}\frac{\partial^2 \overset{k}{\mathbf{m}}}{\partial T_i \partial T_j} =& -\overset{k}{\Gamma}\ |\mathbf{K} - \overset{k}{\gamma}\,\mathbf{I}|\left(\frac{\partial \overset{k}{\mathbf{m}}}{\partial T_i}\cdot\frac{\partial \overset{k}{\mathbf{m}}}{\partial T_j}\right)[\mathbf{K} - \overset{k}{\gamma}\,\mathbf{I}]^{-1}\,\overset{k}{\mathbf{m}} \\ &+ \overset{k}{\Gamma}\,\overset{k}{\mathbf{m}} \times [\mathbf{K} - \overset{k}{\gamma}\,\mathbf{I}]\left(\overset{k}{\mathbf{m}} \times \left[[\frac{\partial \mathbf{K}}{\partial T_i} - \frac{\partial \overset{k}{\gamma}}{\partial T_i}\mathbf{I}]\frac{\partial \overset{k}{\mathbf{m}}}{\partial T_j} + [\frac{\partial \mathbf{K}}{\partial T_j} - \frac{\partial \overset{k}{\gamma}}{\partial T_j}\mathbf{I}]\frac{\partial \overset{k}{\mathbf{m}}}{\partial T_i}\right]\right),\end{aligned} \tag{6.23}$$

and

$$\begin{aligned}\frac{\partial^2 \overset{k}{\mathbf{m}}}{\partial H_p \partial T_i} =&- \overset{k}{\Gamma} \ |\mathbf{K}- \overset{k}{\gamma}\,\mathbf{I}| \left(\frac{\partial \overset{k}{\mathbf{m}}}{\partial H_p}\cdot\frac{\partial \overset{k}{\mathbf{m}}}{\partial T_i}\right)[\mathbf{K}-\overset{k}{\gamma}\,\mathbf{I}]^{-1}\,\overset{k}{\mathbf{m}} \\ &+ \overset{k}{\Gamma}\,\overset{k}{\mathbf{m}}\times[\mathbf{K}-\overset{k}{\gamma}\,\mathbf{I}]\left(\overset{k}{\mathbf{m}}\times\left[[\frac{\partial \mathbf{K}}{\partial T_i} - \frac{\partial \overset{k}{\gamma}}{\partial T_i}\mathbf{I}]\frac{\partial \overset{k}{\mathbf{m}}}{\partial H_p} - \frac{\partial \overset{k}{\gamma}}{\partial H_p}\frac{\partial \overset{k}{\mathbf{m}}}{\partial T_i}\right]\right).\end{aligned} \tag{6.24}$$

Finally, the remaining unknown derivative terms in eqs. (6.16)-(6.18) are obtained from differentiating eq. (6.12) with respect to field and stress as

$$\begin{aligned}\frac{\partial^2 \overset{k}{\lambda}_{uu}}{\partial H_p \partial H_q} &= 3\lambda_{100}\left(\overset{k}{m}_u\,\frac{\partial^2 \overset{k}{m}_u}{\partial H_p \partial H_q} + \frac{\partial \overset{k}{m}_u}{\partial H_p}\frac{\partial \overset{k}{m}_u}{\partial H_q}\right), \\ \frac{\partial^2 \overset{k}{\lambda}_{uv}}{\partial H_p \partial H_q} &= 3\lambda_{111}\left(\overset{k}{m}_u\,\frac{\partial^2 \overset{k}{m}_v}{\partial H_p \partial H_q} + \frac{\partial \overset{k}{m}_u}{\partial H_p}\frac{\partial \overset{k}{m}_v}{\partial H_q} + \overset{k}{m}_v\,\frac{\partial^2 \overset{k}{m}_u}{\partial H_p \partial H_q} + \frac{\partial \overset{k}{m}_v}{\partial H_p}\frac{\partial \overset{k}{m}_u}{\partial H_q}\right), \quad u \neq v,\end{aligned} \tag{6.25}$$

$$\begin{aligned}\frac{\partial^2 \overset{k}{\lambda}_{uu}}{\partial T_i \partial T_j} &= 3\lambda_{100}\left(\overset{k}{m}_u\,\frac{\partial^2 \overset{k}{m}_u}{\partial T_i \partial T_j} + \frac{\partial \overset{k}{m}_u}{\partial T_i}\frac{\partial \overset{k}{m}_u}{\partial T_j}\right), \\ \frac{\partial^2 \overset{k}{\lambda}_{uv}}{\partial T_i \partial T_j} &= 3\lambda_{111}\left(\overset{k}{m}_u\,\frac{\partial^2 \overset{k}{m}_v}{\partial T_i \partial T_j} + \frac{\partial \overset{k}{m}_u}{\partial T_i}\frac{\partial \overset{k}{m}_v}{\partial T_j} + \overset{k}{m}_v\,\frac{\partial^2 \overset{k}{m}_u}{\partial T_i \partial T_j} + \frac{\partial \overset{k}{m}_v}{\partial T_i}\frac{\partial \overset{k}{m}_u}{\partial T_j}\right), \quad u \neq v,\end{aligned} \tag{6.26}$$

and

$$\begin{aligned}\frac{\partial^2 \overset{k}{\lambda}_{uu}}{\partial H_p \partial T_i} &= 3\lambda_{100}\left(\overset{k}{m}_u\,\frac{\partial^2 \overset{k}{m}_u}{\partial H_p \partial T_i} + \frac{\partial \overset{k}{m}_u}{\partial H_p}\frac{\partial \overset{k}{m}_u}{\partial T_i}\right), \\ \frac{\partial^2 \overset{k}{\lambda}_{uv}}{\partial H_p \partial T_i} &= 3\lambda_{111}\left(\overset{k}{m}_u\,\frac{\partial^2 \overset{k}{m}_v}{\partial H_p \partial T_i} + \frac{\partial \overset{k}{m}_u}{\partial H_p}\frac{\partial \overset{k}{m}_v}{\partial T_i} + \overset{k}{m}_v\,\frac{\partial^2 \overset{k}{m}_u}{\partial H_p \partial T_i} + \frac{\partial \overset{k}{m}_v}{\partial H_p}\frac{\partial \overset{k}{m}_u}{\partial T_i}\right), \quad u \neq v.\end{aligned} \tag{6.27}$$

6.2 Summary and Conclusions

Compact analytical Jacobian and Hessian derivative terms are derived in indicial for the Galfenol direct model presented in the previous chapter. These terms are utilized in the following chapters for developing globally convergent magnetostrictive inverse models.

Chapter 7

Efficient and Robust Nonlinear Model for Smart Materials with Application to Composite Magnetostrictive Plates

In certain design and control situations, inverse models are necessary in which stresses must be determined from specified strains. This inversion typically involves an iterative procedure, and requires employment of sophisticated criteria to find the right solution, especially, when multiple solutions exist. Chakrabarti and Dapino [76] proposed an inverse model that describes the full nonlinear coupling in 3D Galfenol transducers. However, this model is susceptible to convergence issues, which are drastically alleviated by the further developments of Deng and Dapino [83]. Nonetheless, both of these models are built on the direct model given in Ref. [43] which is prone to singularities, and can burden computation, especially, when the model is integrated into finite-element solvers. This shortcoming was addressed through the exact solution procedure given in Chapter 5.

Much effort has recently been devoted to developing sophisticated 3D nonlinear models that improve the accuracy and scope of the transducer devices built with such materials, as in Refs. [79, 84, 85]. However, for certain geometries and applications, reduced dimensional constitutive models are sufficient, and would offer computational speed up. For instance, Mindlin [86] developed a first-order plate theory for high frequency piezoelectric crystals. Reddy [87] developed a third order plate theory for laminated composites with integrated sensors and actuators that works reasonably well even for rather thick composites. Kannan and Dasgupta [88] presented a two-dimensional, quasi-static, finite-element scheme to model the nonlinear magnetostrictive material systems. Datta et al. [89, 90] used classical laminated plate theory with the Armstrong model to characterize laminated sensors and actuators in the absence of current-induced magnetic fields. As far as capturing the dynamic behavior of smart materials, Shu et al. [91] recently developed a 1D nonlinear model that simulates the dynamic response of Galfenol-driven unimorph actuators.

Documented in Ref. [45], we develop, in this chapter, a computational framework that consists of a rapidly convergent inverse model, which can effectively and efficiently solve for system unknowns in a finite-element scheme to design smart material based transducers. The inversion scheme is general, and can be applied to any nonlinear smart material with a given direct model. To illustrate the model, Galfenol is taken as an example, and the direct model presented in Chapter 5 together with the analytical Jacobian terms developed in Chapter 6 are utilized. Subsequently, this model is integrated with a finite-element software to model a magnetostrictive material based composite actuator with thin plate geometry. Utilizing a reduced 2D formulation for this application, we demonstrate the improvement in computational efficiency and numerical robustness.

The rest of this chapter is organized as follows. In the following section, 3D system model for embedded smart composites is discussed, and an inverse system model for smart materials is presented. A reduced 2D system model for embedded smart composites is given in Section 7.2. To demonstrate the computational framework, a Galfenol-aluminium plate actuator is considered as a case study in Section 7.3, and the simulation results are given accordingly. Finally, discussions and conclusions are given.

7.1 3D System Model for Embedded Smart Composites

Consider a composite structure consisting of (i) smart material domain, i.e., an *active domain* and (ii) non-smart material domain, i.e., a *passive domain.* The structural behavior of the composite is governed by 3D Navier's equation along with constitutive equations that describe the material behavior specific to each domain. Referring, for example, to Ref. [79], the 3D weak form of Navier's equation is

$$\int_{V_{tot}} \left[\rho \frac{\partial^2 \mathbf{u}}{\partial t^2} \cdot \delta \mathbf{u} + c \frac{\partial \mathbf{u}}{\partial t} \cdot \delta \mathbf{u} + \mathbf{T} \cdot \delta \mathbf{S} \right] dV = \int_{\partial V_{tot}} \mathbf{t} \cdot \delta \mathbf{u} \, d\partial V + \int_{V_{tot}} \mathbf{f}_B \cdot \delta \mathbf{u} \, dV, \quad (7.1)$$

where t is the time, ρ is the density, c represents the damping coefficient, and $\mathbf{T}$ and $\mathbf{f}_B$ denote, respectively, the stress tensor and external body force acting on the domain V_{tot}; the traction vector $\mathbf{t}$ acts on the boundary ∂V_{tot}; and $\mathbf{S}$ and $\mathbf{u}$ represent, respectively, the strain tensor and displacement vector at each point in the domain V_{tot} with the fact that

$$\mathbf{S} = \frac{1}{2} \left(\nabla \mathbf{u} + \nabla \mathbf{u}^{\mathrm{T}} \right). \quad (7.2)$$

Stresses are evaluated using material specific constitutive equations. The passive domain (typically non-magnetic metals such as steel, brass, and aluminum) is governed by Hooke's law, i.e.,

$$\mathbf{T}_p = \mathbf{C}_p \mathbf{S}_p, \quad (7.3)$$

where the subscript p signifies the passive domain, and $\mathbf{C}_p$ is the 3×3 stiffness matrix.

Experimentally, active materials are controlled by stress and field (e.g., electric, magnetic, or thermal) as independent variables; and strain and electric/magnetic/thermal flux density are measured as dependent variables. We write, for example, the constitutive model for strain in the general form

$$\mathbf{S}_a = \mathbf{S}(\mathcal{F}, \mathbf{T}_a), \tag{7.4}$$

where $\mathbf{S}_a$ and $\mathbf{T}_a$ are the strain and stress in active domain; and $\mathcal{F}$ represents the external field vector that can include quantities such as electric field, magnetic field, or temperature. When the stress and external field quantities are unknown, the resulting system is *fully coupled.* For such a case, additional constitutive equations and balance laws (e.g., Maxwell's equations for a magnetomechanical system) are required to complete the mathematical model. However, the focus of this chapter is on systems, for which the field $\mathcal{F}$ is fully defined, and stress is unknown. We refer to such systems as *one-way coupled* systems, and discuss fully coupled systems in the next chapter.

In practice, the constitutive relationship (7.4) is quite nonlinear, and not amenable to a closed form solution for the stress tensor $\mathbf{T}_a$ as a function of strain and field. Hence, when using eq. (7.1) to solve for the displacements, an inversion procedure is inevitable. In what follows, we develop a unified inversion procedure for arbitrary smart materials, and demonstrate its application through magnetostrictive materials.

7.1.1 Inversion Procedure for One-way Coupled Constitutive Model

For convenience, as before, let stress and strain tensors be written in contracted vector notation. Let $\mathbf{S}(\mathcal{F}, \mathbf{T}) = [S_1; S_2; S_3; S_4; S_5; S_6]$ be a given continuous and differentiable direct model for the strain vector, which takes field and stress vectors as input. Finally, let $\mathcal{F}^*$ and $\mathbf{S}^*$ denote any discrete external field and strain vectors specified from experimental measurements or finite-element simulations. The goal of the inverse model is to find the unknown stress vector $\mathbf{T}^*$ that, together with $\mathcal{F}^*$, would give rise to $\mathbf{S}^*$. That is, find $\mathbf{T}$ that satisfies

$$\mathbf{S}(\mathcal{F}^*, \mathbf{T}) - \mathbf{S}^* = 0. \tag{7.5}$$

Our approach to solving the foregoing equation is based on the Newton method. We expand the direct strain model $\mathbf{S}$ in a first order Taylor's series as

$$\mathbf{S}(\mathcal{F}, \mathbf{T} + \Delta\mathbf{T}) \approx \mathbf{S}(\mathcal{F}, \mathbf{T}) + \overbrace{\frac{\partial \mathbf{S}(\mathcal{F}, \mathbf{T})}{\partial \mathbf{T}}}^{\mathbf{J}} \Delta\mathbf{T}, \tag{7.6}$$

where $\Delta\mathbf{T}$ is an incremental stress vector, and $\mathbf{J}$ is the Jacobian matrix. To find $\mathbf{T}$, we employ the foregoing equation, and write a recursive formula based on the Newton method as

$$\mathbf{T}(i+1) \approx \mathbf{T}(i) + \left[\frac{\partial \mathbf{S}(\mathcal{F}^*, \mathbf{T}(i))}{\partial \mathbf{T}}\right]^{-1} (\mathbf{S}^* - \mathbf{S}(\mathcal{F}^*, \mathbf{T}(i)), \tag{7.7}$$

where i is the iteration index. When the Jacobian terms are known, the algorithm initiates at given start solution stress vector $\mathbf{T}(0)$, and gets corrected in successive iterations, until the algorithm is terminated when the residual error is below a predetermined threshold. At this point, the desired $\mathbf{T}^*$ is obtained.

The premise of the model is the material Jacobian of the direct model $\mathbf{S}(\mathcal{F}, \mathbf{T})$, which is material specific. In fact, such terms for Galfenol are already given in Chapter 6.

7.2 Reduced 2D System Model for Embedded Smart Composites

The computational efficiency of the foregoing inverse model is further improved by reducing the 3D system model, described in Section 7.1, to a 2D model for thin composite plate structures. For the analysis of thin composite plates, the conventional modeling approach is based on equivalent single layer (ESL) theories, which are derived from 3D continuum theories by making suitable assumptions concerning the kinematics of deformation or the stress state through the thickness of the laminate. These theories allow the reduction of a 3D problem to a reasonable 2D problem [92]. The simplest form of laminate plate theory is the classical plate theory, where the time-dependent 3D cartesian displacements are approximated using asymptotic expansion along the thickness (z-direction), i.e.,

$$u(x,y,z,t) = u_0(x,y,t) \; + \; z\phi_x(x,y,t), \tag{7.8a}$$

$$v(x,y,z,t) = v_0(x,y,t) \; + \; z\phi_y(x,y,t), \tag{7.8b}$$

$$w(x,y,z,t) = w_0(x,y,t), \tag{7.8c}$$

which reduces the dependence of displacement components u, v, and w to 2D. Here, u_0, v_0, and w_0 are the leading order displacement terms; and ϕ_x and ϕ_y denote rotations about the y and x axes, respectively. Assuming that the deformation has only bending and in-plane stretching components (i.e., transverse normal and transverse shear effects are negligible), these rotations are represented as

$$\phi_x \;=\; -\frac{\partial w_o}{\partial x}, \qquad \phi_y \;=\; -\frac{\partial w_o}{\partial y}. \tag{7.9}$$

As the thickness increases, higher order approximations need to be considered.

However, classical plate theories work well for composite plates with small thickness ratios ($r \leq 0.1$) [87]. Considering this assumption, the displacement forms described by eqs. (7.8)-(7.9) constitute a reduced plane strain problem, in which the strain components S_{zz}, S_{xz}, and S_{yz} are neglected. The remaining strain components can be written as

$$\begin{bmatrix} S_{xx} \\ S_{yy} \\ S_{xy} \end{bmatrix} = \begin{bmatrix} S_{xx}^{(0)} \\ S_{yy}^{(0)} \\ S_{xy}^{(0)} \end{bmatrix} + z \begin{bmatrix} S_{xx}^{(1)} \\ S_{yy}^{(1)} \\ S_{xy}^{(1)} \end{bmatrix}, \tag{7.10}$$

where

$$\begin{aligned} S_{xx}^{(0)} &= \frac{\partial u_0}{\partial x}, \quad S_{yy}^{(0)} = \frac{\partial v_0}{\partial y}, \quad S_{xy}^{(0)} = \frac{1}{2}\left(\frac{\partial u_0}{\partial y} + \frac{\partial v_0}{\partial x}\right), \\ S_{xx}^{(1)} &= \frac{\partial \phi_x}{\partial x}, \quad S_{yy}^{(1)} = \frac{\partial \phi_y}{\partial y}, \quad S_{xy}^{(1)} = \frac{1}{2}\left(\frac{\partial \phi_x}{\partial y} + \frac{\partial \phi_y}{\partial x}\right). \end{aligned} \tag{7.11}$$

The variational form for 2D plate theory is derived by substituting stress, displacement, and strain expressions (7.8)-(7.11) into 3D Navier's equation (7.1) as

$$\begin{aligned} &\int_{\tau} \Bigg\{ \int_{\Omega_e} \Bigg[\left(\bar{\rho}_o \frac{\partial^2 u_o}{\partial t^2} + \bar{c}_o \frac{\partial u_o}{\partial t} + \bar{\rho}_1 \frac{\partial^2 \phi_x}{\partial t^2} + \bar{c}_1 \frac{\partial \phi_x}{\partial t} \right) \delta u_o \\ &+ \left(\bar{\rho}_o \frac{\partial^2 v_o}{\partial t^2} + \bar{c}_o \frac{\partial v_o}{\partial t} + \bar{\rho}_1 \frac{\partial^2 \phi_y}{\partial t^2} + \bar{c}_1 \frac{\partial \phi_y}{\partial t} \right) \delta v_o + \left(\bar{\rho}_o \frac{\partial^2 w_o}{\partial t^2} + \bar{c}_o \frac{\partial w_o}{\partial t} \right) \delta w_o \\ &+ \left(\bar{\rho}_1 \frac{\partial^2 u_o}{\partial t^2} + \bar{c}_1 \frac{\partial u_o}{\partial t} + \bar{\rho}_2 \frac{\partial^2 \phi_x}{\partial t^2} + \bar{c}_2 \frac{\partial \phi_x}{\partial t} \right) \delta \phi_x \\ &+ \left(\bar{\rho}_1 \frac{\partial^2 v_o}{\partial t^2} + \bar{c}_1 \frac{\partial v_o}{\partial t} + \bar{\rho}_2 \frac{\partial^2 \phi_y}{\partial t^2} + \bar{c}_2 \frac{\partial \phi_y}{\partial t} \right) \delta \phi_y \\ &+ N_{xx} \delta S_{xx}^{(0)} + N_{xy} \delta S_{xy}^{(0)} + N_{yy} \delta S_{yy}^{(0)} + M_{xx} \delta S_{xx}^{(1)} + M_{xy} M_{yy} \delta S_{xy}^{(1)} + M_{yy} \delta S_{yy}^{(1)} \Bigg] dx\, dy \\ &- \int_{\partial \Omega_e} \left[\hat{N}_{nn} \delta u_{on} + \hat{N}_{ns} \delta u_{os} - \hat{M}_{nn} \frac{\partial \delta w_o}{\partial n} - \hat{M}_{ns} \frac{\partial \delta w_o}{\partial s} + \hat{Q}_n \delta w_o \right] ds \Bigg\} dt \; = \; 0, \end{aligned} \tag{7.12}$$

where Ω_e represents the total plate area; $\partial\Omega_e$ represents the boundary to Ω_e; τ represents the time over which the dynamic system is studied. Also, the density terms ρ_o, ρ_1, and ρ_2, damping coefficient terms c_0, c_1, and c_2, and stress resultants N_{xx}, N_{yy}, N_{xy}, M_{xx}, M_{yy}, and M_{xy} are defined as

$$\bar{\rho}_k = \int_{t_{tot}} \rho\, z^k\, dz, \qquad \bar{c}_k = \int_{t_{tot}} c\, z^k\, dz, \quad (k = 0,1,2), \tag{7.13}$$

$$\begin{bmatrix} N_{xx} \\ N_{yy} \\ N_{xy} \end{bmatrix} = \int_{t_{tot}} \begin{bmatrix} T_{xx} \\ T_{yy} \\ T_{xy} \end{bmatrix} dz, \tag{7.14}$$

$$\begin{bmatrix} M_{xx} \\ M_{yy} \\ M_{xy} \end{bmatrix} = \int_{t_{tot}} \begin{bmatrix} T_{xx} \\ T_{yy} \\ T_{xy} \end{bmatrix} z\, dz, \tag{7.15}$$

where t_{tot} is the total plate thickness, and the boundary terms $\hat{N}_{nn}, \hat{N}_{ns}, \hat{M}_{nn}$, and $\hat{M}_{ns}$ are the normal and tangential components defined as

$$\begin{bmatrix} \hat{N}_{nn} \\ \hat{N}_{ns} \end{bmatrix} = \int_{t_{tot}} \begin{bmatrix} \hat{\sigma}_{nn} \\ \hat{\sigma}_{ns} \end{bmatrix} dz, \tag{7.16}$$

$$\begin{bmatrix} \hat{M}_{nn} \\ \hat{M}_{ns} \end{bmatrix} = \int_{t_{tot}} \begin{bmatrix} \hat{\sigma}_{nn} \\ \hat{\sigma}_{ns} \end{bmatrix} zdz, \quad \hat{Q}_n = \int_{t_{tot}} \hat{\sigma}_{nz} dz, \tag{7.17}$$

with $\hat{\sigma}_{nn}, \hat{\sigma}_{ns}$, and $\hat{\sigma}_{nz}$ as the specified stress components on the portion of the boundary $\partial\Omega_e$.

Note that the integrals listed in eqs. (7.13)-(7.15) can be directly calculated when the geometry and material properties are specified. However, the stress resultant terms are calculated utilizing the inverse model developed in Subsection 7.1.1.

In what follows, the aforementioned mathematical framework is applied to a Galfenol-aluminium composite structure, and relevant simulation results are presented.

7.3 Case study: Galfenol-aluminium structure for actuator applications

Figure 7.1 depicts a schematic view of a Galfenol-aluminium composite structure. The material parameters for aluminium are: $E = 69$ GPa, $\nu = 0.3$, and $\rho = 2,700$ kg/m^3; and those for Galfenol are tabulated in Table 7.1.

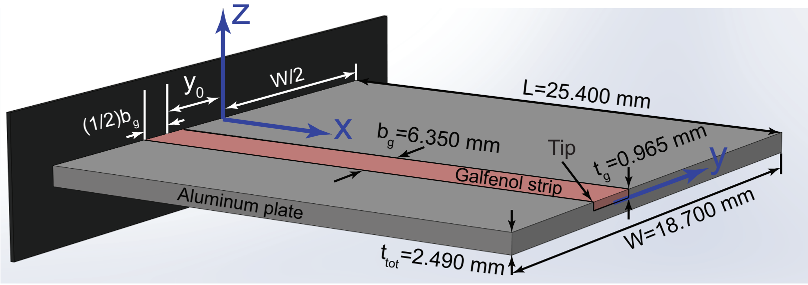

Figure 7.1: Schematic of a Galfenol-aluminium composite structure. The x-y plane of the coordinate system is coincident with the bottom plane of the Galfenol strip, and the x-z plane is a plane of symmetry ($y_0 = 0$).

The actuator geometry presented in this chapter mirrors the sample utilized in the experimental set-up presented in Ref. [93]. The composite plate actuator, consisting of embedded magnetostrictive domain, was manufactured using an Ultrasonic Additive Manufacturing facility. To obtain a bending actuator configuration, the plate was excited using 1D magnetic fields along the Galfenol length, and cantilevered boundary conditions were imposed at the clamped edge. The input alternating and bias magnetic fields of different amplitudes and frequencies (ranging from 0.1 Hz to 500 Hz) were generated using a conductive coil and the displacement data at the tip of the Galfenol patch (labeled in Figure 7.1) was collected. The measured data was subsequently reproduced within a reasonable tolerance, using a dynamic 2D plate model, which employed the inversion procedure presented in Ref. [76]. Additionally, this model assumed approximately uniform magnetic fields throughout the Galfenol volume, which is a reasonable assumption for a plate actuator undergoing small deformations.

In what follows, our novel inversion scheme and the 2D plate model, developed in Sections 7.1 and 7.2, are utilized to study the actuator displacements. Through this application, we demonstrate the computational efficiency and numerical robustness of the proposed computational framework through a comparison with the aforementioned existing approach.

Table 7.1: Parameters for the Galfenol direct model, given in Chapter 5.

Par.	M_s (kA/m)	E (GPa)	λ_{100} (ppm)	λ_{111} (ppm)	c_0	ρ (kg/m^3)
Value	1,273.24	74.50	173.33	-6.67	0.33	7870.00
Par.	K (kJ/m^3)	K_{100} (J/m^3)	Ω (J)	G (GPa)	ν	c (N.s/m)
Value	30.00	-250.00	1,200.00	120.00	0.30	0.10

7.3.1 Solution Methodology

The actuator system, depicted in Figure 7.1, is analyzed using the 2D weak form described by eqs. (7.12)-(7.17). The 2D equations are implemented in the finite-element software COMSOL Multiphysics (version 4.3b), and the constitutive model (Chapter 5) for Galfenol along with the inversion scheme, presented in Subsection 7.1.1, are coded as MATLAB m-files and supplied to COMSOL.

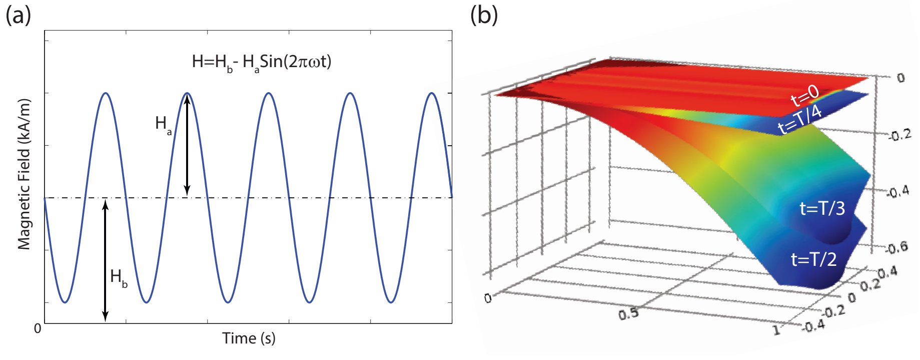

Figure 7.2: (a) A schematic plot of 1D input magnetic field: $H(t) = H_b - H_a \sin(2\pi\omega t)$, and (b) schematic of deflected plate configurations (dimensions in inches) at different fractions of time period (T) corresponding to the frequency ω.

A 1D harmonic magnetic field of the form $H(t) = H_b - H_a \sin(2\pi\omega t)$ is given as input to the system, and the displacements at the tip of the Galfenol patch are analyzed. To generate complete magnetostriction curves, unbiased magnetic field input ($H_b = 0$) of amplitude $H_a = 15$ kA/m greater than the saturation field $H_{sat} \approx 10$ kA/m is applied. To obtain the displacement-field minor loops, a biased magnetic field with $H_b = 3.5$ kA/m and $H_a = 3.25$ kA/m is supplied as input.

Note that no matter what the input field is, the Galfenol patch elongates, and since the centroid of the patch is placed above the neutral axis of the entire plate, it causes the plate to deflect always downward. This is schematically shown in Figure 7.2 for a typical input field. Further results are elaborated in the following section.

7.3.2 Simulation Results

Figure 7.3 depicts the dynamic actuation simulation results, obtained using the proposed model, with unbiased input magnetic field at various frequencies for two periods. At the lowest frequency (0.1 Hz), as expected, hysteresis is minimal, but gets pronounced as the field frequency increases. Hysteresis makes the plate actuator a nonconservative system. To be precise, the displacement vanishes at zero field for both periods as in Subfigures 7.3(a)-(d). In contrast, as shown in Subfigures 7.3(e) and (f), there is a nonzero displacement at zero field at nonzero time.

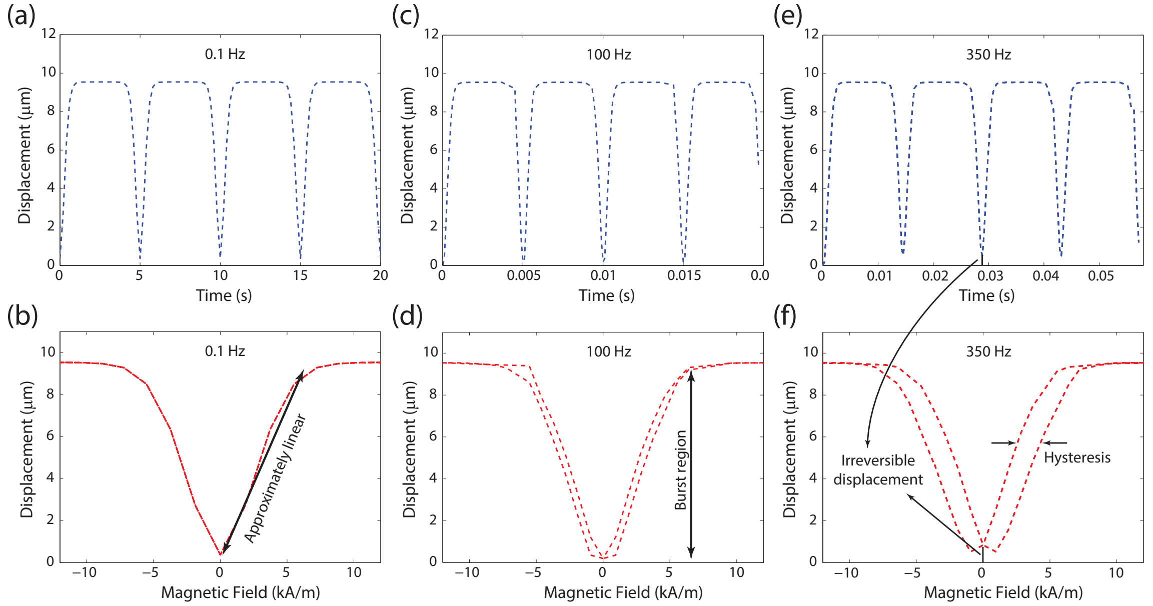

Figure 7.3: Dynamic actuation results, obtained using the proposed model, with 1D unbiased input magnetic field ($H(t) = -15\sin(2\pi\omega t)$ kA/m) for two periods at frequencies: (a),(b) 0.1 Hz; (c),(d) 100 Hz; and (e),(f) 350 Hz. The displacement-field curves are for the last period.

In addition, Subfigures 7.3(b), (d), and (f) show that the plate actuator exhibits an approximately linear response in the “burst” region which forms the basis for the early linear formulations for magnetostrictive transducers. Exploiting the linearity can potentially improve the computational efficiency, but would limit the operational regime of the plate actuator. This motivated our nonlinear solution methodology.

The actuator response to bias input at different frequencies are demonstrated in Figure 7.4, in which an appropriate bias field maps the domain of the input field such that the actuator is operating in the burst region for its entire operational regime. As a further advantage, field biasing can produce bi-directional strains about the bias point, while this is not feasible for the unbiased plate actuator.

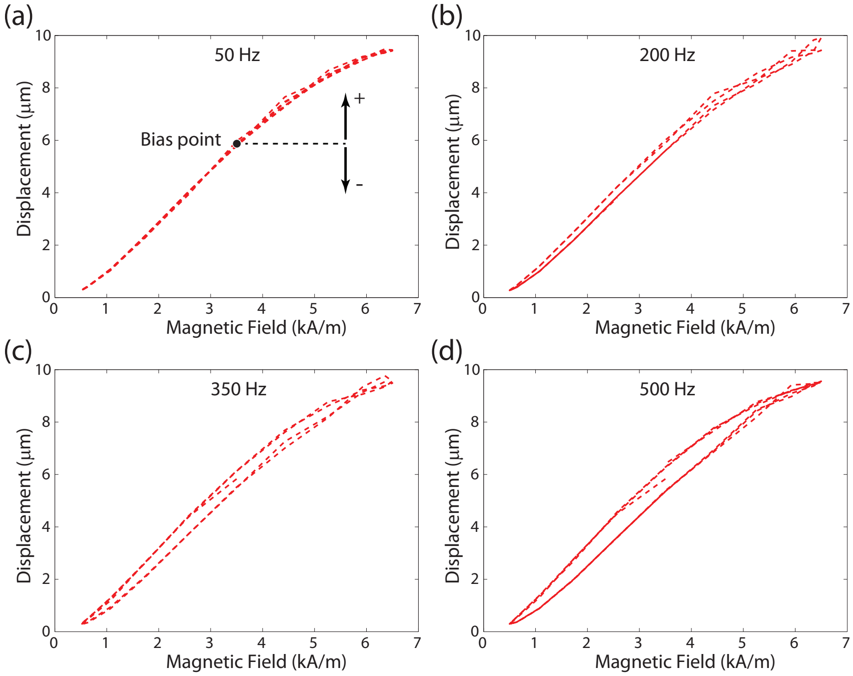

Figure 7.4: Dynamic actuation results with biased input magnetic field $H(t) = 3.50 - 3.25\sin(2\pi\omega t)$ kA/m at different frequencies: (a) 50 Hz, (b) 200 Hz, (c) 350 Hz, and (d) 500 Hz.

In what follows, efficiency and effectiveness of the proposed inverse model is compared to those of the existing approach [76].

Simulation Time Comparison

Employing the same reduced 2D plate model, presented in Section 7.2, we used the existing inverse model to redo the simulation cases, which were discussed above with the proposed inverse model. For all simulations, a physics controlled mesh is used wherein the plate is discretized with triangular mesh elements of size varying from 0.07620 mm to 0.17018 mm, thus, having 5,946 DOFs. The simulations were performed on a quad core 64 bit desktop computer, and the runtimes are tabulated in Table 7.2. Note that the static runtimes correspond to the single initial time instant, and the dynamic simulation runtimes correspond to the averaged time taken to complete one periodic cycle for all of the frequencies discussed above.

Table 7.2: Simulation runtimes for the existing and proposed models.

Model	Existing	Proposed
Static (hh:mm)	00:09	00:02
Dynamic (hh:mm)	30:06	05:09

As per Table 7.2, the proposed inverse model gives dynamic simulation results in almost six times faster than the existing inverse model does. This noticeable time advantage makes the proposed inverse model an effective and efficient tool for the fast design of plate actuators.

Convergence Comparison

The proposed model offers a significant improvement in convergence for dynamic simulations. COMSOL solves for the system state at each instant starting from the initial solution, which is often the previous system state. We observed that the proposed model is able to handle large variation in response between reasonably large time steps, while the existing model requires a very close estimate of the initial solution. This wider convergence zone is attributed to the employment of the analytical strain derivative terms, developed in Chapter 6, by the proposed model.

As a matter of fact, the existing model was not convergent for any of the cases

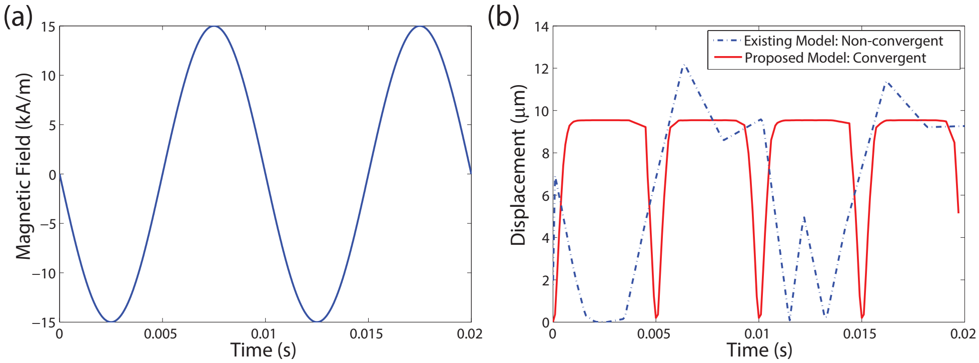

Figure 7.5: Plots of (a) unbiased harmonic magnetic field input, and (b) the response at 100 Hz.

shown already in Figure 7.3. For convenience, field input and strain output plots using both models are shown in Figure 7.5 for the unbiased harmonic magnetic field of frequency 100 Hz over a duration of t = 0.02 s. The figure demonstrates that the existing model converges to a mathematical solution, which is nonphysical. In contrast, the proposed model converges accurately to the physical solution.

Sensitivity to Input Data

Figure 7.6 illustrates the plate's response obtained using the proposed model for a non-smooth input field. The existing model was not convergent, so no result is shown. As demonstrated in Subfigure 7.6(b), the proposed model is intelligent enough to distinguish the sharp corner at $t = 0.005$ s.

7.4 Summary and Conclusions

A computationally efficient and robust nonlinear modeling framework for smart material systems was presented. A novel 3D inversion scheme for nonlinear modeling of smart material based transducers, and a reduced dimensional model (2D) for smart composite plate structures constitute the framework. The framework was integrated

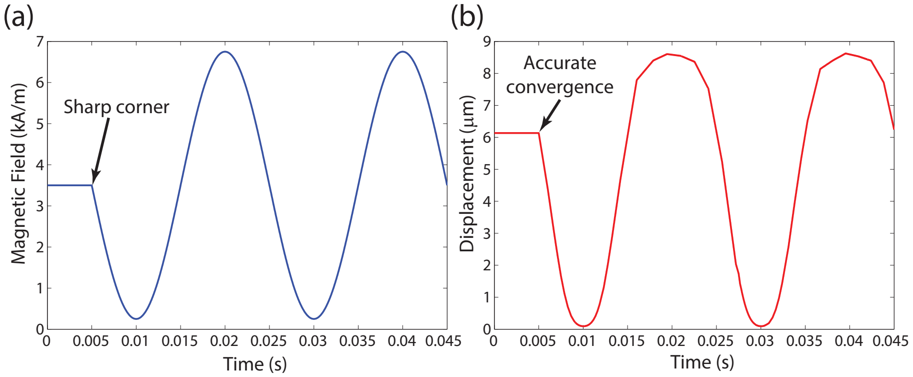

Figure 7.6: (a) Plot of non-smooth 1D magnetic field input, and (b) the response at 50 Hz.

with a finite-element software to analyze an aluminum plate embedded with a Galfenol strip. The resulting nonlinear finite-element framework was utilized to obtain complete and minor magnetostriction curves corresponding to the tip of the Galfenol patch with applying unbiased and biased magnetic fields, respectively. Compared to an existing model, the proposed model gave dynamic simulation results in almost six times faster. Additionally, when an unbiased input field was applied, the proposed model converged accurately to the physical solution, while the existing model converged to a mathematical solution that was nonphysical. The significant advantages in computational time and numerical convergence exhibited by the proposed model are ideal for fast design of plate actuators.

Chapter 8

Fast and Globally Convergent Nonlinear System Model for 3D Magnetostrictive Systems

In the previous chapter, an inverse model for one-way coupled smart material systems was presented. Documented in Ref. [46], the goal of this chapter is to develop an inverse model for fully coupled magnetostrictive systems.

The premise of the existing iterative inverse models for fully coupled magnetostrictive systems is to constitute recursive correction formulae based on first order approximations of some specified error functions. However, the aim of this chapter is to achieve a faster convergence rate by taking second order approximations into account. To do this, the problem is formulated in an optimization framework through defining a novel scalar error function, which allows to effectively incorporate Hessian (matrix of the second order derivatives) of the direct model in the formulation. A continuation approach is then used to achieve global convergence for arbitrary input parameters. The inversion requirement is a continuous and second order differentiable direct model for any chosen magnetostrictive material. The approach is globally convergent, which makes it ideal for use in finite-element frameworks. While the method is developed for arbitrary magnetostrictive materials, Galfenol and the direct model together with the analytical derivative terms, given in Chapters 5 and 6, are chosen to illustrate the inverse model. Finally, convergence rate of the proposed approach is compared successfully to that of Deng and Dapino [83] for the chosen material.

The rest of this chapter is organized as follows. A globally convergent system model for arbitrary magnetostrictive materials is outlined next. The performance of the proposed inverse model is given in Section 8.2. Finally, conclusions are given.

8.1 Magnetostrictive System Model featuring Continuation

As before, let $\mathbf{H} = [H_1; H_2; H_3]$ and $\mathbf{T} = [T_1; T_2; T_3; T_4; T_5; T_6]$ be, respectively, the magnetic field vector and the symmetric stress tensor written in contracted vector notation. Let, further, $\mathbf{B}(\mathbf{H}, \mathbf{T}) = [B_1; B_2; B_3]$ and $\mathbf{S}(\mathbf{H}, \mathbf{T}) = [S_1; S_2; S_3; S_4; S_5; S_6]$ be given continuous and differentiable direct models for, respectively, magnetic flux density and strain vectors, which take magnetic field and stress vectors as input. Finally, let $\mathbf{B}^*$ and $\mathbf{S}^*$ denote any discrete magnetic flux density and strain vectors specified from measurements or finite-element simulations.

The goal is to find the unknown magnetic field and stress vectors $\mathbf{H}^*$ and $\mathbf{T}^*$ that give rise to $\mathbf{B}^*$ and $\mathbf{S}^*$. That is, the goal is to find $\mathbf{H}$ and $\mathbf{T}$ that satisfy the equations

$$\begin{bmatrix} \mathbf{B}(\mathbf{H}, \mathbf{T}) - \mathbf{B}^* \\ \mathbf{S}(\mathbf{H}, \mathbf{T}) - \mathbf{S}^* \end{bmatrix} = 0. \tag{8.1}$$

Our strategy to solving the foregoing system of equations rests on “continuation”, which is an iterative approach that offers global convergence; see Refs. [94, 95] for applications of continuation to kinematic design and analysis of rigid mechanisms.

Let us rewrite the foregoing vector of error functions as a homotopy

$$\begin{bmatrix} \mathbf{B}(\mathbf{H},\mathbf{T}) - \mathbf{B}^\tau \\ \mathbf{S}(\mathbf{H},\mathbf{T}) - \mathbf{S}^\tau \end{bmatrix} \triangleq \begin{bmatrix} \mathbf{B}(\mathbf{H},\mathbf{T}) - ((1-\tau)\mathbf{B}(\mathbf{H}^0,\mathbf{T}^0) + \tau\mathbf{B}^*) \\ \mathbf{S}(\mathbf{H},\mathbf{T}) - ((1-\tau)\mathbf{S}(\mathbf{H}^0,\mathbf{T}^0) + \tau\mathbf{S}^*) \end{bmatrix} = 0, \tag{8.2}$$

where $\mathbf{H}^0$ and $\mathbf{T}^0$ are known start solutions, and $\tau \in [0,1]$ is the continuation parameter. The idea of the continuation is to break the problem into a series of more manageable subproblems, and to solve them sequentially. In doing so, the solutions to the previous subproblem is used as the start solutions to the current subproblem. In essence, continuation initiates at the start solutions $\mathbf{H}^0$ and $\mathbf{T}^0$ at $\tau = 0$, and traces the solution curves of $\mathbf{H}(\tau)$ and $\mathbf{T}(\tau)$ as τ is incremented, until $\tau = 1$ at which point the desired solutions $\mathbf{H}^*$ and $\mathbf{T}^*$ are obtained.

To solve each subproblem effectively, we solve the minimization problem

$$\underset{\mathbf{H}\in\mathbb{R}^3,\ \mathbf{S}\in\mathbb{R}^6}{\text{Minimize}}\ f(\mathbf{H},\mathbf{T}), \tag{8.3}$$

where f is the scalar objective error function

$$f(\mathbf{H},\mathbf{T}) = \frac{1}{2}w_b^2\left[\mathbf{B}(\mathbf{H},\mathbf{T}) - \mathbf{B}^\tau\right]^{\mathrm{T}}\left[\mathbf{B}(\mathbf{H},\mathbf{T}) - \mathbf{B}^\tau\right] + \frac{1}{2}w_s^2\left[\mathbf{S}(\mathbf{H},\mathbf{T}) - \mathbf{S}^\tau\right]^{\mathrm{T}}\left[\mathbf{S}(\mathbf{H},\mathbf{T}) - \mathbf{S}^\tau\right], \tag{8.4}$$

where w_b and w_s are weighting factors chosen to effectively combine the error contributions of magnetic flux density and strain, respectively. Expanding f in a second order Taylor's series as

$$
\begin{aligned}
f(\mathbf{H}+\Delta\mathbf{H},\mathbf{T}+\Delta\mathbf{T}) \approx{}& f(\mathbf{H},\mathbf{T}) + \overbrace{\left[\frac{\partial f(\mathbf{H},\mathbf{T})}{\partial \mathbf{H}}; \frac{\partial f(\mathbf{H},\mathbf{T})}{\partial \mathbf{T}}\right]^{T}}^{[\mathbf{J}^f]^T} [\Delta\mathbf{H};\Delta\mathbf{T}] \\
&+ \frac{1}{2}[\Delta\mathbf{H};\Delta\mathbf{T}]^{\mathrm{T}} \overbrace{\begin{bmatrix} \frac{\partial^2 f(\mathbf{H},\mathbf{T})}{\partial\mathbf{H}\partial\mathbf{H}} & \frac{\partial^2 f(\mathbf{H},\mathbf{T})}{\partial\mathbf{H}\partial\mathbf{T}} \\ \frac{\partial^2 f(\mathbf{H},\mathbf{T})}{\partial\mathbf{T}\partial\mathbf{H}} & \frac{\partial^2 f(\mathbf{H},\mathbf{T})}{\partial\mathbf{T}\partial\mathbf{T}} \end{bmatrix}}^{[\mathbf{H}^f]} [\Delta\mathbf{H};\Delta\mathbf{T}],
\end{aligned} \tag{8.5}
$$

and minimizing it for the incremental magnetic field and stress vectors $\Delta\mathbf{H}$ and $\Delta\mathbf{T}$, may give a recursive correction formula based on the damped Newton method as

$$[\mathbf{H}(i+1);\mathbf{T}(i+1)] = [\mathbf{H}(i);\mathbf{T}(i)] - \alpha_i[\mathbf{H}^f(i)]^{-1}[\mathbf{J}^f(i)], \tag{8.6}$$

where i is the iteration index, and $\mathbf{J}^f$ and $\mathbf{H}^f$ are called the Jacobian (gradient vector for 1D inputs) and Hessian matrices, respectively. When the derivative terms are known, the algorithm initiates at given start solutions $\mathbf{H}(0)$ and $\mathbf{T}(0)$, which get corrected at successive iterations, until the algorithm is terminated when the residual error is below a predetermined threshold. At this point, the desired $\mathbf{H}^\tau$ and $\mathbf{T}^\tau$ are obtained for each subproblem.

For convenience, the derivatives in eq. (8.5) or (8.6) are derived in indicial where it is assumed that the subscripts $p, q \in \{1,\dots,3\}$ and $i, j \in \{1,\dots,6\}$. For brevity, $f(\mathbf{H},\mathbf{T})$, $\mathbf{B}(\mathbf{H},\mathbf{T})$ and $\mathbf{S}(\mathbf{H},\mathbf{T})$ are abbreviated, respectively, as f, $\mathbf{B}$, and $\mathbf{S}$. Accordingly, the first order derivatives are

$$\frac{\partial f}{\partial H_p} = w_h\left(w_b^2\left[\mathbf{B}-\mathbf{B}^\tau\right]^{\mathrm{T}}\frac{\partial\mathbf{B}}{\partial H_p} + w_s^2\left[\mathbf{S}-\mathbf{S}^\tau\right]^{\mathrm{T}}\frac{\partial\mathbf{S}}{\partial H_p}\right), \tag{8.7a}$$

$$\frac{\partial f}{\partial T_i} = w_t\left(w_b^2\left[\mathbf{B}-\mathbf{B}^\tau\right]^{\mathrm{T}}\frac{\partial\mathbf{B}}{\partial T_i} + w_s^2\left[\mathbf{S}-\mathbf{S}^\tau\right]^{\mathrm{T}}\frac{\partial\mathbf{S}}{\partial T_i}\right), \tag{8.7b}$$

and the second order derivatives are

$$\frac{\partial^2 f}{\partial H_p \partial H_q} = w_h^2 \times \\ \left(w_b^2 \left[\mathbf{B} - \mathbf{B}^\tau \right]^\mathrm{T} \frac{\partial^2 \mathbf{B}}{\partial H_p \partial H_q} + w_b^2 \frac{\partial \mathbf{B}^\mathrm{T}}{\partial H_p} \frac{\partial \mathbf{B}}{\partial H_q} + w_s^2 \left[\mathbf{S} - \mathbf{S}^\tau \right]^\mathrm{T} \frac{\partial^2 \mathbf{S}}{\partial H_p \partial H_q} + w_s^2 \frac{\partial \mathbf{S}^\mathrm{T}}{\partial H_p} \frac{\partial \mathbf{S}}{\partial H_q} \right), \tag{8.8a}$$

$$\frac{\partial^2 f}{\partial T_i \partial T_j} = w_t^2 \times \\ \left(w_b^2 \left[\mathbf{B} - \mathbf{B}^\tau \right]^\mathrm{T} \frac{\partial^2 \mathbf{B}}{\partial T_i \partial T_j} + w_b^2 \frac{\partial \mathbf{B}^\mathrm{T}}{\partial T_i} \frac{\partial \mathbf{B}}{\partial T_j} + w_s^2 \left[\mathbf{S} - \mathbf{S}^\tau \right]^\mathrm{T} \frac{\partial^2 \mathbf{S}}{\partial T_i \partial T_j} + w_s^2 \frac{\partial \mathbf{S}^\mathrm{T}}{\partial T_i} \frac{\partial \mathbf{S}}{\partial T_j} \right), \tag{8.8b}$$

$$\frac{\partial^2 f}{\partial H_p \partial T_i} = w_h w_t \times \\ \left(w_b^2 \left[\mathbf{B} - \mathbf{B}^\tau \right]^\mathrm{T} \frac{\partial^2 \mathbf{B}}{\partial H_p \partial T_i} + w_b^2 \frac{\partial \mathbf{B}^\mathrm{T}}{\partial H_p} \frac{\partial \mathbf{B}}{\partial T_i} + w_s^2 \left[\mathbf{S} - \mathbf{S}^\tau \right]^\mathrm{T} \frac{\partial^2 \mathbf{S}}{\partial H_p \partial T_i} + w_s^2 \frac{\partial \mathbf{S}^\mathrm{T}}{\partial H_p} \frac{\partial \mathbf{S}}{\partial T_i} \right), \tag{8.8c}$$

where w_h and w_t are scaling factors for magnetic field and stress vectors. Note that the derivatives of the direct magnetic flux density and stress models present in the foregoing equations must be known. These terms are material specific, and, in the following, we take Galfenol as a case study, for which the direct model and the derivative terms are taken from Chapters 5 and 6, respectively.

8.2 Inverse model performance

No other inverse model corresponding to the direct model that is given in Chapter 5 has been reported in the literature. However, for a slightly different direct model, i.e., that of Ref. [43], Deng and Dapino [83] proposed an inverse model, which is based on the quasi-Newton method. We compare the performance of the two inverse models for two sets of data, 1D and random 3D input data. While each inverse model is implemented in 3D, the former data benchmarks the sensitivity of the two inverse models to the low dimensionality of the data, and the latter tests the generality and stability of the two inverse models for arbitrary input data. These features are pivotal for devising a black-box solver, which is envisioned to be integrated into finite-element frameworks. Note that we provide no timing information since the two direct models are of different formulations. For a fair comparison, we disable continuation in the proposed model by setting τ to one.

To generate comparative data, a series of magnetic field and stress vectors is specified, and fed to the direct model, given in Chapter 5, to produce magnetic induction and strain vectors. The constructed dataset is fed to the two inverse models to see whether the original magnetic field and stress inputs, up to a tolerance of 10^{-9}, are returned.

8.2.1 Performance for 1D inputs

Utilizing the direct model parameters, given earlier in Table 5.1, Figure 8.1 illustrates the direct and inverse model simulations for 1D magnetic field and stress inputs. The solid curves in Subfigures 8.1(a),(b) and (d),(e) represent the direct model simulations for actuation and sensing cases, respectively. Induction and strain curves are discretized into equally spaced points, and are fed to the inverse models. Subfigures 8.1 (c) and (f) depict the maximum number of iterations that the two inverse models take for actuation and sensing cases, respectively. For this 1D case, both the existing and proposed inverse models are able to solve the inverse magnetomechanical problem effectively. Even though the 3D implementations of the two inverse models are employed, the results demonstrate that the two models are not sensitive to 1D data. Nonetheless, the existing inverse model diverges for four runs. In addition, the proposed inverse model converges in fewer iterations than the existing approach. This

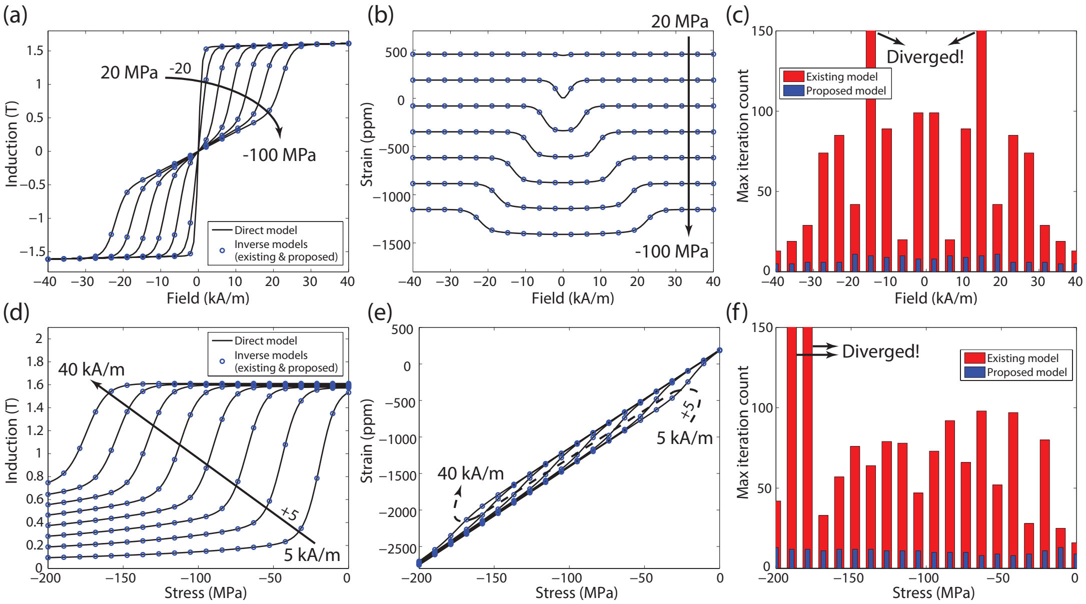

Figure 8.1: Direct and inverse model simulations for ⟨100⟩ $\mathrm{Fe}_{81.5}\mathrm{Ga}_{18.5}$ grown with FSZM for 1D (a),(b),(c) actuation; and (d),(e),(f) sensing. Any run taking more than 500 iterations is assumed to be divergent.

faster rate of convergence is expected, as the proposed model employs exact derivative terms, while the existing approach employs approximate terms, development of which is a premise of the quasi-Newton method.

It is worth indicating that, for a 1D case and at constant stress values, an ideal inversion procedure must be independent of the sign of the field inputs. This is demonstrated in Subfigure 8.1(c), as the iteration counts for both inversion models are symmetric about the origin.

8.2.2 Performance for random 3D inputs

We used the parameters listed in Table 7.1 to generate 3D magnetic induction and strain inputs. To be precise, a set of 1,000,000 magnetic field and stress vectors in the range of, respectively, $[-40, 40]$ kA/m and $[-500, 500]$ MPa is randomly generated, with the constraint that the sampled stress tensor must have a von Mises stress smaller than 500 MPa, which is a rough estimate of the ultimate strength of Galfenol. This randomly generated dataset is fed to the direct model to construct a generic input dataset for the two inverse models.

Table 8.1: Performance of the existing and proposed inverse models for a large 3D generic dataset.

Approach	# runs	# Failures	Avg. iteration count*
Existing model	1,000,000	146,116	101
Proposed model		0	8

* Divergent runs are not considered.

As demonstrated in Table 8.1, the proposed model is globally convergent, while the existing inverse model failed for almost 14.6% of the 1,000,000 runs. This shows that increasing the dimension and generality of the input data has absolutely no effect on the proposed inverse model. Additionally, the proposed model offered, in average, a 13 times faster convergence rate than the existing model for each run. Hence, the proposed model can be employed as a powerful black-box solver in finite-element frameworks.

8.2.3 Choice of the iterative step size α

For both the quasi-Newton method and the damped Newton method, the step size α, present for example in eq. (8.6), must be calculated at each iteration. There is a variety of line search algorithms for this purpose, but they fall into two major categories: exact and approximate. For the simulations, an exact line search based on Golden Section Search (see, for example, Ref. [96]) is used. However, an approximate line search is often sufficient, and can save much computational time. This will be the subject of future work.

8.2.4 Choice of start solution

Start solutions have a major role in the success of iterative techniques, such as quasi- or damped Newton methods. Even if chosen within the convergence zone, an ill-conditioned start solution may lead to a long runtime. Presented in Chapter 6, the exact derivative terms, even if compact, are unwieldy and computationally expensive to evaluate. Even if they lead to minimal number of iterations, they are most efficient when used for local rather than global convergence. Therefore, it is more efficient to carry on a preprocessing step, in which a less robust but faster approach such as quasi-Newton method is used to generate a reasonable approximate solution. Then, feeding this approximate solution as a start solution to the main algorithm would save computational time. Alternatively, one may use continuation, which is self-constructive, as it automatically generates a reasonably well-conditioned start solution through solving a series of intermediate subproblems.

For the simulations, zero start solutions are used. However, the inverse model is devised for use in a finite-element framework. In such a case, the system state is known at some instant, and this state is a good candidate as a start solution for the next state. This feature is useful for control applications.

8.3 Summary and Conclusions

In this chapter, a fully coupled magnetomechanical system model for arbitrary magnetostrictive materials was presented. The model requirement is a continuous and second order differentiable direct model for any chosen magnetostrictive material. The approach is globally convergent, which makes it ideal for use in finite-element frameworks. The premise of the existing iterative system models is to constitute recursive correction formulae based on first order approximations of some specified error functions. However, to achieve a faster convergence rate, the problem is formulated in an optimization framework through defining a novel scalar error function, and took second order approximations into account. A continuation approach was, then, developed to achieve global convergence for arbitrary input parameters.

The inverse model is valid for arbitrary magnetostrictive materials. To illustrate, Galfenol was chosen as the magnetostrictive material, and the direct model and the corresponding derivative terms, developed in Chapters 5 and 6 were utilized. The performance of the proposed approach was compared successfully to an existing system model, which is based on quasi-Newton method. While the existing model failed for 14.6% of the 1,000,000 runs, the proposed model had no failures. In addition, the proposed model converges, in average, in almost 13 times less number of iterations than the existing model for each run. To further improve the proposed model, an efficient line search algorithm and a carefully developed start solution are needed. As for the latter, start solutions are obviated when using continuation, which generates them automatically. Alternatively, when using the model in a finite-element framework, the current system state can be used as a reasonable candidate for the start solution.

Chapter 9
Conclusions and Future Work

This chapter gives a synopsis of the dissertation. Then, the major research contributions are enumerated. Finally, a list of future works is given.

9.1 Summary and Conclusions

Robust and efficient mathematical techniques for modeling and simulation of smart material systems were presented. First, passive materials were discussed which undergo large deformations. Accordingly, Euler–Bernoulli cantilever beams subjected to combined tip point loading were studied, and both cartesian and parametric large deflection solutions were presented. The cartesian solutions are independent of the beam's arc length, but are implicit and in terms of elliptic integrals. However, they are envisioned to guide the development of approximate closed form large deflection solutions. For the case of a large pure end-force, a new closed form explicit solution was also presented which incorporated the rotation matrix employed for developing the aforementioned cartesian solutions. On the other hand, the parametric solutions are in terms of the loading parameters with using the Automatic Taylor Expansion technique. The solutions were shown to be independently and efficiently adaptable for very large loading conditions. To gain further efficiency and robustness, piecewise parametric large deflection solutions were also developed which require low approximation orders for a fast convergence. The solutions were coded as a stand-alone black-box solver, which offers several functionalities for the solution of large deflection of Euler–Bernoulli cantilever beams.

Then, smart materials, particularly, magnetostrictive materials were discussed. Several improvements for the Discrete Energy-Averaged model on calculating the 3D hysteretic magnetization and magnetostriction of iron-gallium alloys were proposed. In particular, the magnetoelastic energy was enhanced through the utilization of the more thorough expression of the magnetostriction tensor, and the Gibbs free energy was improved through the reduction of the magnetic stiffness matrix. Also, an analytical solution procedure was presented which offers multiple (up to the number of easy directions) local minimum energy directions for each individual easy direction. These additional minima help avoid the singularities that are present in the existing approximate solution, and also help better understand the material's complex response to arbitrary stress and magnetic field inputs. Nonetheless, the resulting robustness comes at an expense. For general loadings, the model requires the solution of six 6th order polynomials. As a result, the exact solution procedure is about two times slower than the approximate procedure for 3D applications. However, analytical reductions of the model were presented for 2D and 1D applications. In the simplest case (i.e., 1D applications), only a single 4th order polynomial must be solved, thus, making the exact solution procedure as efficient as the approximate procedure. Our exact solution procedure led us to deriving compact analytical Jacobian and Hessian derivative terms for this model.

A novel optimization routine was also proposed for finding the model parameters. Rather than employing anhysteretic curves, our approach utilizes the average of the hysteretic data, which obviates taking additional measurements. Our optimization routine retains the number of model constants, but divides the parameters into exclusive sets, which are optimized in a decoupled procedure. The effectiveness of the overall model was verified through comparison with existing measurement data. The hysteretic model has two sources of error: the nonhysteretic model and the hysteresis formulation itself. Even though the nonhysteretic model closely agreed with the averaged hysteretic data, the observed error propagated to the hysteretic simulations. Additionally, the parameters of the hysteretic model, which were previously thought to control only the hysteresis width, appeared to introduce unexpected error. For instance, the hysteresis model added error to the nonhysteretic magnetization response in the lower saturation region, where the hysteresis effects should have been negligible.

Then, a computationally efficient and robust nonlinear modeling framework was presented for smart material systems. The framework consists of a novel 3D inversion scheme for nonlinear modeling of smart material based transducers, and a reduced 2D dimensional model for smart composite plate structures. The framework was integrated into a finite-element software to analyze an aluminum plate embedded with a Galfenol strip, for which major and minor magnetostriction curves, corresponding to the tip of the Galfenol patch, were obtained with applying unbiased and biased magnetic fields. Compared to an existing model, the proposed model gave dynamic simulation results in almost six times faster. Additionally, when an unbiased input field was applied, the proposed model converged accurately to the physical solution, while the existing model converged to a mathematical solution that was nonphysical. The significant advantages in computational time and numerical convergence exhibited by the proposed model are ideal for fast design of plate actuators.

Finally, a fully coupled magnetomechanical system model based on continuation for arbitrary magnetostrictive materials was proposed. The problem was formulated in an optimization framework through defining a novel scalar error function, and second order approximations were taken into account. This has led to a faster convergence rate compared to an existing system model, which is based on quasi-Newton method. Our approach is globally convergent, while the existing model failed for 14.6% of the 1,000,000 runs. Additionally, the proposed model offered, in average, a 13 times faster convergence rate than the existing model for each run.

9.2 Research Contributions

Compact and rapidly convergent piecewise parametric large deflection solutions of Euler–Bernoulli cantilever beams have been developed. The proposed methodology can quantify the inherently nonlinear and complex load, deformation, and energy relationships revealed by compliant mechanisms efficiently and effectively, thus, can pave the way for the emergence of novel compliant mechanisms syntheses. Approximate linear theories are still the premise of certain devices in precision engineering. However, the overall dimensions of such devices must be adjusted with the magnitudes of the applied loads. The utilization of the proposed solution methodology can help in the design of new devices with fixed size and no dependence on the load magnitudes.

Computationally efficient and robust nonlinear modeling frameworks have been presented for smart material systems. The speed and global convergence of the proposed models are ideal for use in finite-element frameworks, and can lead to new powerful black-box smart material solvers. With the utilization of such solvers, the analysis and synthesis of, for example, smart material based transducers can be effectively expedited. When many design candidates are at hand, designers can do an exhaustive analysis, and find the optimal solution quickly.

9.3 Future Work

Constant material and cross sectional properties were considered for the Euler–Bernoulli beam application. Aiming to adapt the proposed solution methodology for cases, for which such properties are variable, would be a future work. Furthermore, geometries with non-cantilevered beam boundary conditions, such as those occurring in shafts, would be an additional research consideration.

Research is needed to further enhance the discrete energy-averaged model. The magnetocrystalline and magnetoelastic energies utilized in the derivation of the Gibbs free energy can be further improved. The magnetocrystalline energy is currently based on a phenomenological derivation, which is, in fact, linear in the magnetization direction components. A higher order formulation would lead to further accuracy. On the other hand, the current formulation of the magnetoelastic energy is based on an existing magnetostriction formula, which was derived for pure magnetic field inputs. A new derivation that takes into account contributions from both magnetic field and stress inputs would require further research.

In addition, the current hysteresis model builds on the nonhysteretic formulation of the discrete energy-averaged model. Thus, any inaccuracy manifested by the latter would be propagated to the hysteresis model. Further research is required to develop a stand-alone hysteresis model.

Finally, further research is needed to develop an efficient approximate line search algorithm for the inverse model for fully coupled magnetostrictive systems. In addition, when the system's prior loading history is not known, devising an effective and efficient start solution for the model can save much computational time. This is also the subject of future work.

Bibliography

[1] R. L. Norton, *Design of Machinery, An Introduction to the Synthesis and Analysis of Mechanisms and Machines.* New York: McGraw-Hill, 2008.

[2] L. L. Howell, *Compliant Mechanisms.* John Wiley & Sons, 2001.

[3] D. H. Hodges, *Nonlinear Composite Beam Theory*, vol. 213 in Progress in Astronautics and Aeronautics Series. Reston, VA: AIAA, 2006.

[4] K. E. Bisshop and D. C. Drucker, "Large deflection of cantilever beams," *Quarterly of Applied Mathematics*, vol. 3, pp. 272–275, 1945.

[5] L. L. Howell, "The design and analysis of large-deflection members in compliant mechanisms," M.S. Thesis, Purdue University, 1991.

[6] A. Banerjee, B. Bhattacharya, and A. Mallik, "Large deflection of cantilever beams with geometric non-linearity: Analytical and numerical approaches," *International Journal of Non–Linear Mechanics*, vol. 43, no. 5, pp. 366–376, 2008.

[7] L. Chen, "An integral approach for large deflection cantilever beams," *International Journal of Non–Linear Mechanics*, vol. 45, no. 3, pp. 301–305, 2010.

[8] M. Mutyalarao, D. Bharathi, and B. N. Rao, "On the uniqueness of large deflections of a uniform cantilever beam under a tip-concentrated rotational load,"

International Journal of Non–Linear Mechanics, vol. 45, no. 4, pp. 433–441, 2010.

[9] K. Lee, “Large deflections of cantilever beams of non-linear elastic material under a combined loading,” *International Journal of Non–Linear Mechanics*, vol. 37, no. 3, pp. 439–443, 2002.

[10] E. Solano-Carrillo, “Semi-exact solutions for large deflections of cantilever beams of non-linear elastic behaviour,” *International Journal of Non–Linear Mechanics*, vol. 44, no. 2, pp. 253–256, 2009.

[11] L. L. Howell and A. Midha, “Parametric deflection approximations for end-loaded, large-deflection beams in compliant mechanisms,” *ASME, Journal of Mechanical Design*, vol. 117, no. 1, pp. 156–165, 1995.

[12] M. H. Dado, “Variable parametric pseudo-rigid-body model for large-deflection beams with end loads,” *International Journal of Non–Linear Mechanics*, vol. 36, no. 7, pp. 1123–1133, 2001.

[13] C. Kimball and L.-W. Tsai, “Modeling of flexural beams subjected to arbitrary end loads,” *ASME, Journal of Mechanical Design*, vol. 124, no. 2, pp. 223–235, 2002.

[14] H. Tari, “Effective start point for the automatic Taylor expansion technique with application to micropolar fluids, heat transfer, and theoretical biology,” *In preparation*, 2014.

[15] H. Tari, “On the parametric large deflection study of Euler–Bernoulli cantilever beams subjected to combined tip point loading,” *International Journal of Non-Linear Mechanics*, vol. 49, pp. 90–99, 2013.

[16] H. Tari, G. L. Kinzel, and D. A. Mendelsohn, "Cartesian and piecewise parametric large deflection solutions of tip point loaded Euler–Bernoulli cantilever beams," *In preparation*, 2014.

[17] H. Kwun and K. A. Bartels, "Magnetostrictive sensor technology and its applications," *Ultrasonics*, vol. 36, no. 1, pp. 171–178, 1998.

[18] J. J. Dosch, D. J. Inman, and E. Garcia, "A self-sensing piezoelectric actuator for collocated control," *Journal of Intelligent Material Systems and Structures*, vol. 3, no. 1, pp. 166–185, 1992.

[19] H. A. Sodano, D. J. Inman, and G. Park, "A review of power harvesting from vibration using piezoelectric materials," *Shock and Vibration Digest*, vol. 36, no. 3, pp. 197–206, 2004.

[20] K. Chandrashekhara and A. N. Agarwal, "Active vibration control of laminated composite plates using piezoelectric devices: a finite element approach," *Journal of Intelligent Material Systems and Structures*, vol. 4, no. 4, pp. 496–508, 1993.

[21] R. C. Smith, *Smart material systems: model development*, vol. 32. Siam, 2005.

[22] D. J. Leo, *Engineering Analysis of Smart Material Systems.* Wiley InterScience, Wiley, 2007.

[23] W. G. Cady, *Piezoelectricity: an introduction to the theory and applications of electromechanical phenomena in crystals.* Dover New York, 1964.

[24] S. Chakrabarti and M. J. Dapino, "Fully coupled discrete energy-averaged model for Terfenol-D," *Journal of Applied Physics*, vol. 111, no. 5, 2012.

[25] A. E. Clark, M. Wun-Fogle, J. B. Restorff, and T. A. Lograsso, "Magnetic and magnetostrictive properties of Galfenol alloys under large compressive stresses,"

in *PRICM-4: Int.Symp. on Smart Materials–Fundamentals and system Applications, Pacific Rim Conf. on Advanced Materials and Processing*, 2001.

[26] R. A. Kellogg, *Development and modeling of iron–gallium alloys.* Ph.D. Dissertation, Iowa State University, 2003.

[27] J. Atulasimha and A. B. Flatau, "A review of magnetostrictive iron-gallium alloys," *Smart Materials and Structures*, vol. 20, no. 4, p. 043001, 2011.

[28] L. Landau and E. Lifshitz, "On the theory of the dispersion of magnetic permeability in ferromagnetic bodies," *Physikalische Zeitschrift der Sowjetunion*, vol. 8, p. 153, 1935.

[29] X.-P. Wang, C. J. Garca-Cervera, and W. E, "A GaussSeidel projection method for micromagnetics simulations," *Journal of Computational Physics*, vol. 171, no. 1, pp. 357–372, 2001.

[30] C. J. García-Cervera, Z. Gimbutas, and W. E, "Accurate numerical methods for micromagnetics simulations with general geometries," *Journal of Computational Physics*, vol. 184, no. 1, pp. 37–52, 2003.

[31] B. V. de Wiele, F. Olyslager, and L. Dupré, "Application of the fast multipole method for the evaluation of magnetostatic fields in micromagnetic computations," *Journal of Computational Physics*, vol. 227, no. 23, pp. 9913–9932, 2008.

[32] E. Kritsikis, A. Vaysset, L. D. Buda-Prejbeanu, F. Alouges, and J. C. Toussaint, "Beyond first-order finite element schemes in micromagnetics," *Journal of Computational Physics*, vol. 256, no. 0, pp. 357–366, 2014.

[33] F. Preisach, "Über die magnetische nachwirkung," *Zeitschrift für Physik*, vol. 94, no. 5–6, pp. 277–302, 1935.

[34] A. Globus, “Universal hysteresis loop for soft ferrimagnetic material,” *Proc. Europ. Physical Society, Conference on Soft Magnetic Material*, vol. 2, p. 233, 1975.

[35] D. C. Jiles and D. L. Atherton, “Theory of ferromagnetic hysteresis,” *Journal of Magnetism and Magnetic Materials*, vol. 61, pp. 48–60, 1986.

[36] E. C. Stoner and E. P. Wohlfarth, “A mechanism of magnetic hysteresis in heterogeneous alloys,” *IEEE Transactions on Magnetics*, vol. 27, no. 4, pp. 3475–3518, 1991.

[37] F. Liorzou, B. Phelps, and D. L. Atherton, “Macroscopic models of magnetization,” *IEEE Transactions on Magnetics*, vol. 36, no. 2, pp. 418–428, 2000.

[38] G. P. Carman and M. Mitrovic, “Nonlinear constitutive relations for magnetostrictive materials with applications to 1-D problems,” *Journal of Intelligent Material Systems and Structures*, vol. 6, no. 5, pp. 673–683, 1995.

[39] X. J. Zheng and L. Sun, “A nonlinear constitutive model of magneto-thermo-mechanical coupling for giant magnetostrictive materials,” *Journal of Applied Physics*, vol. 100, no. 6, p. 063906, 2006.

[40] W. D. Armstrong, “An incremental theory of magneto-elastic hysteresis in pseudo-cubic ferro-magnetostrictive alloys,” *Journal of Magnetism and Magnetic Materials*, vol. 263, pp. 208–218, 2003.

[41] J. Atulasimha, G. Akhras, and A. B. Flatau, “Comprehensive three dimensional hysteretic magnetomechanical model and its validation with experimental $\langle 110 \rangle$ single-crystal iron-gallium behavior,” *Journal of Applied Physics*, vol. 103, no. 7, p. 07B336, 2008.

[42] P. G. Evans and M. J. Dapino, "Efficient magnetic hysteresis model for field and stress application in magnetostrictive Galfenol," *Journal of Applied Physics*, vol. 107, no. 6, p. 063906, 2010.

[43] S. Chakrabarti, *Modeling of 3D magnetostrictive systems with application to Galfenol and Terfenol-D transducers.* Ph.D. Dissertation, The Ohio State University, 2011.

[44] H. Tari, J. J. Scheidler, and M. J. Dapino, "Robust solution procedure for the discrete energy-averaged model on calculation of the 3D hysteretic magnetization and magnetostriction of iron-gallium alloys," *Journal of Magnetism and Magnetic Materials, In review*, 2014.

[45] H. Tari, S. Santapuri, and M. J. Dapino, "Efficient and robust nonlinear model for smart materials with application to composite magnetostrictive plates," *Journal of Computational Physics, In preparation*, 2014.

[46] H. Tari and M. J. Dapino, "Fast and globally convergent nonlinear system model for 3D magnetostrictive systems," in *Proceedings of the ASME: Smart Materials, Adaptive Structures and Intelligent Systems*, 2014. Rhode Island, September 8-10.

[47] J. D. Cole, *Perturbation Methods in Applied Mathematics.* MA: Blaisdell Publishing Company, 1968.

[48] A. M. Lyapunov, *General Problem on Stability of Motion.* London: Taylor & Francis, 1892, Translated in English, 1992.

[49] A. V. Karmishin, A. I. Zhukov, and V. G. Kolosov, *Methods of dynamic calculation and testing for thin-walled structures.* Moscow: Mashinostroenie, 1990 In Russian.

[50] G. Adomian and G. E. Adomian, "A global method for solution of complex systems," *Mathematical Modelling*, vol. 5, no. 4, pp. 251–263, 1984.

[51] Z. Gharsseldien and K. Hemida, "New technique to avoid "noise terms" on the solutions of inhomogeneous differential equations by using adomian decomposition method," *Communications in Nonlinear Science and Numerical Simulation*, vol. 14, no. 3, pp. 685–696, 2009.

[52] Y. Q. Hasan and L. M. Zhu, "Solving singular boundary value problems of higher-order ordinary differential equations by modified adomian decomposition method," *Communications in Nonlinear Science and Numerical Simulation*, vol. 14, no. 6, pp. 2592–2596, 2009.

[53] S. J. Liao, *The Proposed Homotopy Analysis Technique for the Solution of Nonlinear Problems.* Ph.D. Dissertation, Shanghai Jiao Tong University, 1992.

[54] C.-S. Liu, "The essence of the generalized Taylor theorem as the foundation of the homotopy analysis method," *Communications in Nonlinear Science and Numerical Simulation*, vol. 16, no. 3, pp. 1254–1262, 2011.

[55] S. Liao, "An optimal homotopy-analysis approach for strongly nonlinear differential equations," *Communications in Nonlinear Science and Numerical Simulation*, vol. 15, no. 8, pp. 2003–2016, 2010.

[56] J.-H. He, "Homotopy perturbation technique," *Computer Methods in Applied Mechanics and Engineering*, vol. 178, no. 3–4, pp. 257–262, 1999.

[57] M. S. H. Chowdhury, I. Hashim, and O. Abdulaziz, "Comparison of homotopy analysis method and homotopy-perturbation method for purely nonlinear fin-type problems," *Communications in Nonlinear Science and Numerical Simulation*, vol. 14, no. 2, pp. 371–378, 2009.

[58] J.-H. He, “Variational iteration method for autonomous ordinary differential systems,” *Applied Mathematics and Computation*, vol. 114, no. 2–3, pp. 115–123, 2000.

[59] H. Tari, “Modified variational iteration method,” *Physics Letters A*, vol. 369, no. 4, pp. 290–293, 2007.

[60] R. E. Moore, *Methods and Applications of Interval Analysis.* Studies in Applied Mathematics, SIAM, 1979.

[61] A. Gibbons, “A program for the automatic integration of differential equations using the method of Taylor series,” *The Computer Journal*, vol. 3, no. 2, pp. 108–111, 1960.

[62] G. Corliss and Y. F. Chang, “Solving ordinary differential equations using Taylor series,” *ACM Transactions on Mathematical Software*, vol. 8, pp. 114–144, 1982.

[63] Y. F. Chang and G. Corliss, “Atomft: Solving odes and daes using Taylor series,” *Computers & Mathematics with Applications*, vol. 28, no. 10–12, pp. 209–233, 1994.

[64] T. W. Gamelin, *Complex Analysis.* Springer, 2001.

[65] A. C. Eringen, “Theory of micropolar fluids,” *Journal of Mathematics and Mechanics*, vol. 16, pp. 1–18, 1966.

[66] N. A. Kelson, A. Desseaux, and T. W. Farrell, “Micropolar flow in a porous channel with high mass transfer,” in *Proc. of 10th Computational Techniques and Applications Conference CTAC-2001* (K. Burrage and R. B. Sidje, eds.), vol. 44, pp. C479–C495, 2003.

[67] S. P. Liaw and R. H. Yeh, "Fins with temperature dependent surface heat flux–i. single heat transfer mode," *International Journal of Heat and Mass Transfer*, vol. 37, no. 10, pp. 1509–1515, 1994.

[68] M.-H. Chang, "A decomposition solution for fins with temperature dependent surface heat flux," *International Journal of Heat and Mass Transfer*, vol. 48, no. 9, pp. 1819–1824, 2005.

[69] D. D. Ganji, "The application of He's homotopy perturbation method to nonlinear equations arising in heat transfer," *Physics Letters A*, vol. 355, no. 4–5, pp. 337–341, 2006.

[70] S. Abbasbandy, "The application of homotopy analysis method to nonlinear equations arising in heat transfer," *Physics Letters A*, vol. 360, no. 1, pp. 109–113, 2006.

[71] H. Tari, D. D. Ganji, and H. Babazadeh, "The application of He's variational iteration method to nonlinear equations arising in heat transfer," *Physics Letters A*, vol. 363, no. 3, pp. 213–217, 2007.

[72] S. Abbasbandy and E. Shivanian, "Exact analytical solution of a nonlinear equation arising in heat transfer," *Physics Letters A*, vol. 374, no. 4, pp. 567–574, 2010.

[73] D. L. S. McElwain, "A re-examination of oxygen diffusion in a spherical cell with michaelis-menten oxygen uptake kinetics," *Journal of Theoretical Biology*, vol. 71, no. 2, pp. 255–263, 1978.

[74] A. S. V. R. Kanth and K. Aruna, "He's variational iteration method for treating nonlinear singular boundary value problems," *Computers & Mathematics with Applications*, vol. 60, no. 3, pp. 821–829, 2010.

[75] F. A. Chouery, “Exact and numerical solutions for large deflection of elastic non-prismatic beams,” *FAC Systems INC., WA*, 2006.

[76] S. Chakrabarti and M. J. Dapino, “Nonlinear finite element model for 3D Galfenol systems,” *Smart Materials and Structures*, vol. 20, no. 10, p. 105034, 2011.

[77] G. Engdahl, *Handbook of giant magnetostrictive materials.* Academic Press, San Diego, CA, 2000.

[78] C. Kittel, “Physical theory of ferromagnetic domains,” *Rev. Mod. Phys.*, vol. 21, pp. 541–583, 1949.

[79] P. G. Evans and M. J. Dapino, “Dynamic model for 3-D magnetostrictive transducers,” *IEEE Transactions on Magnetics*, vol. 47, no. 1, pp. 221–230, 2011.

[80] T. Cormen, C. Leiserson, R. Rivest, and C. Stein, *Introduction to algorithms.* MIT Press, Cambridge, Mass., 2009.

[81] P. Bratley and B. L. Fox, “Algorithm 659: Implementing sobol’s quasirandom sequence generator,” *ACM Transactions on Mathematical Software*, vol. 14, no. 1, pp. 88–100, 1988.

[82] A. Saltelli, P. Annoni, I. Azzini, F. Campolongo, M. Ratto, and S. Tarantola, “Variance based sensitivity analysis of model output. design and estimator for the total sensitivity index,” *Computer Physics Communications*, vol. 181, no. 2, pp. 259–270, 2010.

[83] Z. Deng and M. J. Dapino, “Characterization and finite element modeling of Galfenol minor flux density loops,” *Proc. SPIE, Behavior and Mechanics of Multifunctional Materials and Composites*, vol. 8689, pp. 86890V–11, 2013.

[84] J. E. Huber, N. A. Fleck, C. M. Landis, and R. M. McMeeking, “A constitutive model for ferroelectric polycrystals,” *Journal of the Mechanics and Physics of Solids*, vol. 47, no. 8, pp. 1663–1697, 1999.

[85] J. G. Boyd and D. C. Lagoudas, “A thermodynamical constitutive model for shape memory materials. part i. the monolithic shape memory alloy,” *International Journal of Plasticity*, vol. 12, no. 6, pp. 805–842, 1996.

[86] R. D. Mindlin, “High frequency vibrations of piezoelectric crystal plates,” *International Journal of Solids and Structures*, vol. 8, no. 7, pp. 895–906, 1972.

[87] J. N. Reddy, “On laminated composite plates with integrated sensors and actuators,” *Engineering Structures*, vol. 21, no. 7, pp. 568–593, 1999.

[88] K. S. Kannan and A. Dasgupta, “A nonlinear galerkin finite-element theory for modeling magnetostrictive smart structures,” *Smart Materials and Structures*, vol. 6, no. 3, p. 341, 1997.

[89] S. Datta, J. Atulasimha, C. Mudivarthi, and A. B. Flatau, “The modeling of magnetomechanical sensors in laminated structures,” *Smart Materials and Structures*, vol. 17, no. 2, p. 025010, 2008.

[90] S. Datta, J. Atulasimha, C. Mudivarthi, and A. B. Flatau, “Modeling of magnetomechanical actuators in laminated structures,” *Journal of Intelligent Material Systems and Structures*, vol. 20, no. 9, pp. 1121–1135, 2009.

[91] L. Shu, L. Headings, M. J. Dapino, D. Chen, and Q. Lu, “Nonlinear model for Galfenol cantilevered unimorphs considering full magnetoelastic coupling,” *Journal of Intelligent Material Systems and Structures*, vol. 0, no. 0, pp. 1–17, 2013.

[92] J. N. Reddy, *Mechanics of laminated composite plates and shells: theory and analysis*. CRC, 2003.

[93] S. Santapuri, J. J. Scheidler, and M. J. Dapino, “Dynamic nonlinear two-dimensional modeling framework for composite laminates with embedded magnetostrictive materials,” *Composite Structures, In review*, 2014.

[94] H. Tari and H. J. Su, “Complete solution to the eight-point path generation of slider-crank four-bar linkages,” *Journal of Mechanical Design*, vol. 132, no. 8, p. 081003, 2010.

[95] H. Tari, H. J. Su, and T. Y. Li, “A constrained homotopy technique for excluding unwanted solutions from polynomial equations arising in kinematics problems,” *Mechanism and Machine Theory*, vol. 45, no. 6, pp. 898–910, 2010.

[96] M. J. Box, D. Davies, and W. H. Swann, *Nonlinear Optimization Techniques (Monograph No. 5: Mathematical and Statistical Techniques for Industry)*. Imperial Chemical Industries Limited, Oliver & Boyd, 1969.